

1 Experimental Measurements of Convective Heat Flux Ahead of Fire

1.1 Introduction

It has long been known that fuel particles can ignite when enough radiative and convective heat is transferred to them [1]. Thus, experimental studies of fire propagation in simple and complex vegetative fuels usually focus on dynamics of the fire front and thermal measurements [2–4]. Radiative heat transfer has been often assumed to be the governing heat transfer mechanism in flame propagation[5]. However, recent findings show radiation is often not sufficient by itself [4, 6–10]. To understand the dynamics of fire propagation in vegetative fuels, it is crucial to include the convective mode of heat transfer. [11, 12]. Unlike radiative heat transfer, which can be measured using radiative heat flux gauges, no instrument can directly measure convective heat transfer. Convective heat transfer can be quantitatively calculated by measuring total and radiative heat flux using a Schmidt-Boelter sensor [10]. This methodology calculates the heat flux at the surface of the sensor. Hence, this method doesn't provide information on the local velocity field, which governs the convective heat transfer.

Optical methods such as Particle Image Velocimetry (PIV) have been performed to quantify the local velocity field and flow structure of the fire environment [13, 14]. The information provided by PIV is limited to the velocity field so it cannot provide a complete picture of thermal convection because the temperature is not measured. In more recent work, Gustenyov et al. [15] used smoke to visualize flow over a heated plate inside of a low-speed wind tunnel. The heated plate was used to simulate spreading line fire. With the development of infrared imaging, thermography methodologies can be used for the temperature mapping inside the fire plume [16]. The combination of thermography and PIV has been used to estimate the velocity and temperature

profile within the fire plume [17]. This methodology, known as Thermal Particle Image Velocimetry (TPIV), used hotspots within the plume as tracing particles and computed the displacement of such particles to obtain the velocity field within the fire plume. Due to the low IR emissivity of gases TPIV measurements were limited to direct tracking of hot particles in the plume, but no direct measurements of convective gas motion around the fire are feasible.

Moreover, the temperature field around the flame fluctuates as a consequence of the turbulent nature of the flame, [2, 18] These changes in temperature lead to density fluctuations that can be visualized by schlieren systems [19]. The common schlieren system, which was introduced by Toepler [20], needs a complex optical system using high precision lenses and mirrors. Wernekinck and Merzkirch [21] tried to reduce the complexity of the schlieren system by calculating and analyzing the displacement of laser generated speckle patterns. Background Oriented Schlieren (BOS), and Background Oriented Optical Tomography (BOOT) were invented almost simultaneously by Dalziel [22] and Meier [23]. In the development of BOS, Meier used PIV approach and captured optical distortion of the PIV-like speckled background noise. The optical distortion produced a pseudo-PIV with the particle displacement characterizing the distortion. While BOS is actually synthetic background-distortion schlieren, the BOS acronym is well-established [24]. Because of its easy and inexpensive configuration, BOS has become an important tool in flow visualization [25] and can be used for 2D and 3D reconstruction of the flow field. Various methods of BOS using different backgrounds have been developed [26–29]. The primary results from these various methods are visualizations of the flow field, density gradients, and density associated with the flow field.

Schlieren systems and speckle noise patterns have been used for a wide variety of flow imagery applications in different scales , from microvascular flow [30] to flow of a supersonic aircraft [31]

and flow visualization around a turbulent flame [32–38]. Schlieren imagery in fire plume applications has been usually deployed to a controlled burner flame rather than vegetative fuel beds. Recently Grauer et al. [39] applied background oriented optical tomography and reconstructed the 3D instantaneous refractive index field of a turbulent flame. Typically, schlieren images have not been processed to obtain secondary data such as velocity fields and important parameters related to the flow structure. These studies did not investigate and visualize the hot gas plume behaviour when an external flow is present.

In the present study, convective heat transfer was quantified to help understand its effects on pyrolysis and ignition in laboratory and small scales field fires. This measurement was part of a larger study that is measuring and modeling pyrolysis of common plant species located in the southern United States[40]. The experiments were conducted in a low-speed wind tunnel located at the USDA Forest Service Pacific Southwest Research Station fire laboratory in Riverside, CA[41, 42]. The details of the experimental setup and configuration are provided in section 1.3. Various technique have been used to describe flow fields around laboratory fires inside this wind tunnel[43–45], However, since the addition of foreign matter in the present study would have affected the gas sampling objective, 2D Background Oriented Schlieren system was deployed to visualize hot gases around a turbulent diffusive flame and help to describe the flow fields around the fire as it spread in a porous vegetative fuel bed. Section 1.2 gives a brief background on the BOS system. This section also describes the calculation process for flow visualization and velocity calculation. The result and summary of BOS analysis are provided in section 1.5. Other than the BOS system, other instruments such as heat flux sensors and thermocouples were used in the wind tunnel as well. These instruments are described in the experimental design section 1.3. The results associated with these instruments are described in section 1.6 and 1.7.

1.2 Background Oriented Schlieren

The fundamental principle and governing equation for schlieren flow visualization in gases is the Gladstone-Dale equation.[46]

$$n - 1 = K(\lambda) \cdot \rho, \quad (1)$$

where n is the refractive index of the medium which is linearly proportional to the density of the medium ρ . The proportionality constant, $K(\lambda)$, is known as the Gladstone-Dale constant and is a very weak function of temperature and is a function of the wavelength λ and the chemical composition of the medium [46]. For air, $K(\lambda)$ is usually taken to be $0.23 \cdot 10^{-3}(m^3/kg)$. Fig. 1, shows a simple setup of Background Oriented Schlieren configuration. Z_D is the distance of the inhomogeneous field from the background noise pattern. Z_B is the distance of the camera lens from the background. ϵ_y represent the deflection angle. L is the depth of the inhomogeneous flow field, f is the focal length of the camera, $\Delta y'$ is the displacement in the camera sensor plane and Δy is displacement in the background plane.

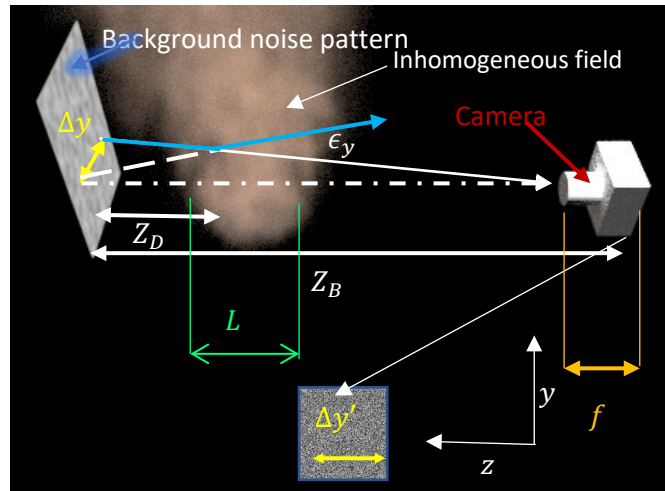


Figure 1. A simple schematic of BOS configuration.

In the configuration, such as the ones represented by Figure 1, The image of the background noise patterns does not get distorted when there is a homogenous density field between the pattern and

the camera. However, if there is a density gradient (inhomogeneous field) when light encounters the density gradient fields, it deflects with the deflection angle, ϵ_y . The camera sensor records the deflection as displacement $\Delta y'$. The displacement, $\Delta y'$ can be measured by comparing the background image with and without the inhomogeneous field. According to schlieren theory[47, 48], ϵ_y is a line integral of the refractive index gradient $\partial n / \partial y$ along the optical axis z . For a planar 2D BOS, the refractive gradient is assumed to be constant along the z axis. The Schlieren equation can be written as

$$\epsilon_y = \frac{1}{n} \int \frac{\partial n}{\partial y} dz = \frac{L}{n_\infty} \left(\frac{\partial n}{\partial y} \right) \quad (2)$$

where L is the depth of the inhomogeneous medium, and n_∞ is the refractive index of the ambient air. From figure 1

$$\tan(\epsilon_y) = \frac{\Delta y}{Z_D} = \frac{\Delta y'}{Z_B} \cdot f \quad (3)$$

assuming that the deflection angle is small ($\epsilon_y \cong \tan(\epsilon_y)$), equations 2 and 3 are combined to give:

$$\Delta y' = Z_D \frac{f}{Z_B} \frac{L}{n_\infty} \left(\frac{\partial n}{\partial y} \right) \quad (4)$$

$$\Delta y = Z_D \frac{L}{n_\infty} \left(\frac{\partial n}{\partial y} \right) \quad (5)$$

Values of L, n_∞, Z_D, f, Z_B are constant and depend only on the configuration of the experimental setup. Applying the Gladstone-Dale principal (equation 1), to equations 4 and 5, results in

$$\frac{\partial \rho}{\partial y} = \frac{n_\infty Z_B}{K(\lambda) \cdot Z_D \cdot f \cdot L} \Delta y' = G_1 \cdot \Delta y' \quad (6)$$

$$\frac{\partial \rho}{\partial y} = \frac{n_{\infty}}{K(\lambda) \cdot Z_D \cdot L} \Delta y = G_2 \cdot \Delta y \quad (7)$$

where G_1 and G_2 are constants which depend on the setup configuration and the Gladstone-Dale constant. The simplifications introduced in equation 6 and 7 are based on the assumption the changes in density gradient are more significant than changes in the Gladstone-Dale constant ($K(\lambda)/\partial y \ll 1$).

Combining equations 6 and 7 with using the common linear variation in density with temperature ($\rho = \rho_0[1 + \beta(T - T_0)]$) where β is the thermal expansion coefficient, it can be shown that:

$$\frac{\partial T}{\partial y} = C_1 \cdot \Delta y' \quad (8)$$

$$\frac{\partial T}{\partial y} = C_2 \cdot \Delta y \quad (9)$$

where C_1 and C_2 are constants which depend on the setup configuration, $K(\lambda)$ and β .

Since this method visualizes density gradients, it directly leads to the visualization of baroclinicity[49].

1.2.1 Displacement calculations

As shown in equation 6, the density gradient for every pixel is obtained by calculating displacement ($\Delta y'$) between the distorted and undistorted images. Displacement vectors can be derived using common cross-correlation algorithms developed primarily for PIV applications. A common open-source software is OPEN-PIV [50]. PIV cross correlation algorithms result in loss of resolution, especially when higher BOS sensitivity requires a bigger integration window [51].

In computer science, the calculation of the displacement vectors from a pair of images is commonly referred to as optical flow estimation. Atcheson et al. [52] compared optical flow algorithms with cross-correlation algorithms for BOS flow visualization and found that optical

flow algorithms significantly increased the resolution of BOS. Settles and Hargather [24] concluded although image cross-correlation processing is more straightforward, optical flow algorithms are preferable due to a better resolution Horn-Schunck [53] and Lucas–Kanade [54] are the two most common optical-flow algorithms used. In this study, in addition to the Horn-Schunck and Lucas–Kanade algorithms, more complex optical flow algorithms, such as Farneback's algorithm [55], Brox algorithm [56] and TV-L1 algorithm[57], were applied to the BOS dataset. Usually, optical flow algorithms are computationally expensive; making real-time imaging almost impossible [24]. However, the computational speed of optical flow algorithms can be improved significantly by developing an optical flow algorithm on a GPU architecture, such as the Nvidia¹ CUDA platform. In this study, all the optical flow algorithms, except for Horn-Schunck, were developed using Nvidia's CUDA platform for faster computation. In the following section, the common principals behind optical flow estimation and the algorithms used in this study are described.

1.2.1.A Optical Flow Estimation of the Flow Field

Optical flow is apparent movement of brightness patterns in an image which is formed from the relative motion of an object with regards to a viewer. The concept of optical flow estimation arises from Gibson's [58] work on the visual stimulus provided to animals. Considering the surface that is being imaged is flat with uniform illumination across the surface, the brightness at a point in the image is proportional to reflectance of the surface at that point. Assuming that the reflectance varies smoothly, the brightness data is differentiable. Optical flow is defined as the 2D vector field describing apparent motion of each pixel point between two images $I(x, y, t_0)$, $I(x, y, t_1)$. Here

¹ The use of trade or firm names in this publication is for reader information and does not imply endorsement by the U.S. Department of Agriculture of any product or service.

I is the brightness values associated with each point of the image (x, y) at the timestamp t_1 and t_2 .

- **Brightness Conservation Constraint (Aperture problem)**

Assuming that the grey value (brightness) of a pixel does not change by displacement, the following relation can be written

$$I(x, y, t) = I(x + \delta x, y + \delta y, t + \delta t) \quad (10)$$

Based on this assumption, also known as conservation of brightness, the change of brightness of a specific pixel point between a pair of images is due to the apparent motion of those pixels. Conservation of brightness principal could be restated as if a point in the object is selected, and then the point is followed between a pair of images, the intensity of the pixel does not change. The linearized version of the brightness conservation assumption leads to optical flow constraint:

$$\frac{DI}{Dt} = \frac{\partial I}{\partial t} + \frac{\delta x}{\delta t} \cdot \frac{\partial I}{\partial x} + \frac{\delta y}{\delta t} \cdot \frac{\partial I}{\partial y} = \frac{\partial I}{\partial t} + u \cdot \frac{\partial I}{\partial x} + v \cdot \frac{\partial I}{\partial y} = 0 \quad (11)$$

Here u, v are the velocity (displacement) vectors associated with the flow field. Conservation of brightness is a conceptual concept that is not always correct, because various external sources have an effect of the brightness of a pixel. Moreover, equation (11) is based on the assumption that apparent motion between a pair of images is small and it is in order of the size of a pixel. Thus equation (11) by itself may not provide a good estimation of big movements in the image. Nevertheless, Equation (11) states that the apparent motion is dependent on both spatial and temporal gradient of pixel intensities. There are two unknowns u and v in equation 11, thus the optical flow constraint cannot provide information of the 2D vector u, v by itself. Additional constraints are needed to solve for u and v .

- **Smoothness Constraint**

One of the earliest attempts to provide a solution for u and v in equation (11) was provided by Horn-Schunck [53]. In this methodology, they introduced another constraint known as the smoothness constraint. This constraint states that for very slow displacement and movements the square of the gradient of velocity should be very small, mathematically

$$E_S^2 = \left(\frac{\partial u}{\partial x}\right)^2 + \left(\frac{\partial u}{\partial y}\right)^2 + \left(\frac{\partial v}{\partial x}\right)^2 + \left(\frac{\partial v}{\partial y}\right)^2 \quad (12)$$

Here E_S^2 is the energy function associated with the gradient of velocity that should be minimized.

Equation (12) and (11) could be combined to provide the following energy function:

$$\int_{\Omega} \left(\frac{\partial I}{\partial t} + u \cdot \frac{\partial I}{\partial x} + v \cdot \frac{\partial I}{\partial y} \right)^2 + \alpha (|\nabla u|^2 + |\nabla v|^2) dx dy \quad (13)$$

where Ω represent the image domain, and α is a factor which weights in the smoothness constraint.

After basic transformations, it is shown that minimization of equation (13) is equivalent to minimization of

$$\int_{\Omega} \left(\frac{DI}{Dt} \right)^2 + \alpha ((\nabla \cdot U)^2 + |\nabla \times U|^2) dx dy \quad (14)$$

where $U = u \cdot \hat{i} + v \cdot \hat{j}$ is the velocity vector. In fluid mechanics, minimization of divergence of velocity $(\nabla \cdot U)$ corresponds to the fact that the flow is incompressible, and minimization of $\nabla \times U$ signifies that the vorticity, corresponding to the flow field between a pair of images, is minimized

- **Solution Scheme for Horn-Schunck**

The Horn-Schunck algorithm is one of the fundamental algorithms in optical flow measurements, and many algorithms are based on it. In this methodology, to solve for u and v , the Euler-

Lagrange equation is applied to the energy function shown in equation (14), resulting to the following system of Partial differential equations:

$$I_x \left(\frac{\partial I}{\partial t} + u \cdot \frac{\partial I}{\partial x} + v \cdot \frac{\partial I}{\partial y} \right) - \alpha^2 \nabla^2 u = 0 \quad (15.a)$$

$$I_y \left(\frac{\partial I}{\partial t} + u \cdot \frac{\partial I}{\partial x} + v \cdot \frac{\partial I}{\partial y} \right) - \alpha^2 \nabla^2 v = 0 \quad (15.b)$$

Approximating the Laplace of velocity as an average velocity of surrounding pixels ($\nabla^2 u \approx \kappa(\bar{u} - u)$) and $\nabla^2 v \approx \kappa(\bar{v} - v)$, the equations 15 can be simplified as:

$$(\alpha^2 + I_x^2)u + I_x I_y v = \alpha^2 \bar{u} - I_x I_t \quad (16.a)$$

$$I_x I_y u + (I_y^2 + \alpha^2)v = \alpha^2 \bar{v} - I_y I_t \quad (16.b)$$

Thus, u and v can be obtained by solving the following system of equations through iteration.

$$(\alpha^2 + I_x^2 + I_y^2)u = +(\alpha^2 + I_y^2)\bar{u} - I_x I_y \bar{v} - I_x I_t \quad (17.a)$$

$$(\alpha^2 + I_x^2 + I_y^2)v = +(\alpha^2 + I_x^2)\bar{v} - I_x I_y \bar{u} - I_y I_t \quad (17.b)$$

- **Gradient constancy constraint:**

The brightness conservation constraint has the drawback that slight changes in brightness can influence the results. Uras[59] introduced another reasonable constraint, besides equation (11).

Based on equation (11), he showed that the following system of equations would hold :

$$\frac{\partial^2 I}{\partial x \partial t} + u \cdot \frac{\partial^2 I}{\partial x^2} + v \cdot \frac{\partial^2 I}{\partial x \partial y} = 0 \quad (18.a)$$

$$\frac{\partial^2 I}{\partial y \partial t} + u \cdot \frac{\partial^2 I}{\partial x \partial y} + v \cdot \frac{\partial^2 I}{\partial y^2} = 0 \quad (18.b)$$

This system of equations could be rewritten as :

$$\frac{D}{Dt}(\nabla I) = 0 \quad (19)$$

In other words, in this constraint, it is assumed that the gradient of the brightness of the images doesn't vary due to displacement:

$$\nabla I(x, y, t) = \nabla I(x + \delta x, y + \delta y, t + \delta t) \quad (20)$$

Here ∇ denotes the spatial gradient. This assumption allows accounting for a small variation in the brightness of images. In the general case, equation 19 will not hold, the more accurate general equation is :

$$\frac{D}{Dt}(\nabla I) = \mathbf{M}^T \nabla I \quad (21)$$

Here \mathbf{M}^T is the transpose of the following (2 X 2) matrix :

$$\mathbf{M} = \begin{bmatrix} \frac{\partial u}{\partial x} & \frac{\partial u}{\partial y} \\ \frac{\partial v}{\partial x} & \frac{\partial v}{\partial y} \end{bmatrix} \quad (22)$$

Equation 21 can be rewritten as

$$\mathbf{H}U = -\nabla I_t + U \cdot \frac{DI}{DT} - M^T \nabla I \quad (23)$$

Here \mathbf{H} is the Hessian with respect to spatial coordinates. Knowing that equation (11) holds, (23) becomes:

$$\mathbf{H}U = -\nabla I_t - M^T \nabla I \quad (24)$$

Equation 24 shows that in order for equation 19 to hold $||M^T \nabla I|| \ll \nabla I_t$. Uras discussed although the situations this condition is not satisfied can easily be produced, experience has shown that this

condition holds in most cases. In order to solve for $U = (u, v)$, the following linear system is solved with the exception where $Det\mathbf{H}$ vanishes:

$$\mathbf{H}U = -\nabla I_t \quad (25)$$

It can be shown that equation 25 is the same as equation 19. The gradient constancy constraint allows a small variation in the image brightness and helps to solve for the displacement vector (u, v) by using a constraint that doesn't vary under image brightness fluctuations. Compared to brightness conservation-equation (10), image gradient conservation is more helpful to resolve translation motions, while brightness conservation is better for more complicated motions

- **Multiscale Approach.**

The optical flow constraint is only valid when the partial derivatives can be correctly approximated. Such as when the motion is small, or the gradient of the image is linear. In order to estimate large displacements, the optical flow is usually embedded in a multi-scale strategy. One of these strategies is known as the image pyramid method. In this method, the image pyramid is made by repeatedly downsampling an image by a given factor. This factor can have any value smaller than one and depends on the image size and the sensitivity of the deployed algorithm. The optical flow is found on the smallest image in the pyramid and is used to unwarp the next largest image. Interpolation is used for the fractional pixel locations

- **Variational Model for optical flow estimation**

To estimate the optical flow, Brox et al. [56] derived an energy function that penalized deviations from model assumptions. The first energy function is the measurement of global deviation from conservation of brightness and gradient constancy assumption , equations (10) and (20). Letting $\mathbf{x} := (x, y, t)^T$ and $\mathbf{w} := (u, v, 1)^T$ the energy function is written as :

$$E_1(u, v) = \int_{\Omega} \psi(|I(\mathbf{x} + \mathbf{w}) - I(\mathbf{x})|^2 + \gamma(|\nabla I(\mathbf{x} + \mathbf{w}) - \nabla I(\mathbf{x})|^2)) d\mathbf{x} \quad (26)$$

Where γ is a weight function between both constraints. In order to make the energy function more robust, Brox et al applied a concave function $\psi(s^2) = \sqrt{s^2 + \epsilon^2}$, which is the modified $L1$ minimization to the first term in equation 26. Afterwards, they introduced a smoothness term which explains the assumption that the model is piecewise smooth which, is expressed as :

$$E_2 = \int_{\Omega} \psi(|\nabla_3 u|^2 + |\nabla_3 v|^2) \quad (27)$$

Where the operator ∇_3 is the tempo-spatial gradient. In the case of comparing two consecutive frames of images, the operator is replaced by the spatial gradient, (Horn-Schunck smoothness constraint). The total energy function is the weighted sum between the two energy functions

$$E(u, v) = E_1 + \alpha E_2 \quad (28)$$

Here α is the regularization parameter. Brox et al approach uses coarse to fine warping method (image pyramids) to find the (u, v) which minimize energy function E .

- **TV-L1 optical flow Estimation**

As mentioned earlier, the Horn-Schnuck approach is a good method when the displacements are small. In the presence of large displacements, it is common to replace the optical flow constraint in equation 11 with :

$$I(\mathbf{x} + \mathbf{w}) - I(\mathbf{x}) = 0 \quad (29)$$

This equation is not linear; therefore commonly it is linearized using Taylor expansion, resulting in

$$F(\mathbf{w}) = \nabla I(\mathbf{x} + \mathbf{w}^0) \cdot (\mathbf{w} - \mathbf{w}^0) + I(\mathbf{x} + \mathbf{w}^0) - I(\mathbf{x}) \quad (30)$$

Zach et al. [57] and Sanchez et al. [60] defined an energy function

$$E(w) = \int_{\Omega} (|\nabla u| + |\nabla v|) + \lambda |F(\mathbf{w})| \quad (31)$$

To minimize the energy function, Zach et al. and Sanchez et al. introduced the following convex relation:

$$E(w) = \int_{\Omega} (|\nabla u| + |\nabla v|) + \frac{1}{2\Theta} |u - v| + \lambda |F(\mathbf{w})| \quad (32)$$

Setting Θ to a very small value forces the minimization to occur where u and v are nearly equal, which reduces to the original energy function defined in equation (32)

- **Lucas-Kanade method**

Almost concurrently with the seminal work of Horn-Schunck, Lucas-Kanade [54] introduced another methodology and mindset for optical flow estimation. In their work, Lucas-Kanade assumed that the motion between the two images is slow and the displacement is constant in each small blocks of the image. Therefore, equation (11) can hold for all pixel of a window W . Writing the optical flow equation for each point of the window will result to the following system of equations

$$\begin{bmatrix} I_x(P_1) & I_y(P_1) \\ \vdots & \vdots \\ I_x(P_n) & I_y(P_n) \end{bmatrix} \cdot \begin{bmatrix} u \\ v \end{bmatrix} = \begin{bmatrix} -I_t(P_1) \\ \vdots \\ -I_t(P_n) \end{bmatrix} \quad (33)$$

Where P_n indicates the pixel inside the block window. Simplifying this equation, it could be written as $A \cdot v = b$. This system of equations has more equation than unknowns, therefore using the Least Square principle, both sides of the equation is multiplied by transpose matrix A^T :

$$A^T A v = A^T b \quad (34)$$

Solving for the velocity matrix, the following equation is formed

$$v = (A^T A)^{-1} A^T b \quad (35)$$

The computation will be as

$$\begin{bmatrix} u \\ v \end{bmatrix} = \begin{bmatrix} \Sigma W^2 \left(\frac{\partial I}{\partial x} \right)^2 & \Sigma W^2 \left(\frac{\partial I}{\partial x} \right) \left(\frac{\partial I}{\partial y} \right) \\ \Sigma W^2 \left(\frac{\partial I}{\partial x} \right) \left(\frac{\partial I}{\partial y} \right) & \Sigma W^2 \left(\frac{\partial I}{\partial y} \right)^2 \end{bmatrix}^{-1} \cdot \begin{bmatrix} -\Sigma W^2 \left(\frac{\partial I}{\partial x} \right) \cdot \left(\frac{\partial I}{\partial t} \right) \\ -\Sigma W^2 \left(\frac{\partial I}{\partial y} \right) \cdot \left(\frac{\partial I}{\partial t} \right) \end{bmatrix} \quad (36)$$

Here W is the window function to emphasize the constraint at the center of each window.

- **Farneback method**

In a totally different approach, Farneback [55] introduced another algorithm, which does not solve for equation (11). Instead, this methodology approximated a neighborhood of both frames at a time t_1 and t_2 using a polynomial function. For the case of a quadratic polynomial, the image brightness (intensity) can be written as:

$$I_{t_1}(x) = x^T A_1 x + b_1^T x + c_1 \quad (37)$$

A new signal can be constructed using a global displacement (d) as

$$\begin{aligned} I_{t_1}(x - d) &= (x - d)^T A_1 (x - d) + b_1^T (x - d) + c_1 \\ &= x^T A_1 x + (b_1 - 2A_1 d)^T x + d^T A_1 d - b_1^T d + c_1 \end{aligned} \quad (38)$$

$$I_{t_2}(x) = x^T A_2 x + b_2^T x + c \quad (39)$$

Since $I_{t_1}(x - d) = I_{t_2}(x)$, equating the coefficient in the quadratic polynomial yields to $b_2 = b_1 - 2A_1 d$. From $b_2 = b_1 - 2A_1 d$ the transition value d could be solved if A_1 is non-singular. In principle, equation (38) and (39) can be equated at every pixel, and the solution may be obtained

iteratively. Farneback noted that the pointwise solution is too noisy. Instead, the displacement may be assumed to be slow-varying and satisfies a neighborhood of W values of x , this reduces to a problem similar to (36) and the solution is obtained as

$$d = (\sum W A^T A)^{-1} \sum W A^T \Delta b \quad (40)$$

Here $A(x) = 1/2(A_1(x) + A_2(x))$ and $\Delta b = -1/2(b_2(x) - b_1(x))$. It is interesting to note the similarities between equation (40) and (36) reveals some similarities and differences between the Lucas-Kanade method and The Farneback Method. Lucas Kanade uses the gradient information in the vicinity of the pixels of interest, while the Farneback method approximates the same information using with the coefficients of a local quadratic polynomial.

1.3 Experimental setup

The measurements described in this section are part of a larger study that is measuring and modeling pyrolysis of common plant species located in the southern United States[40]. As part of this larger study, pyrolysis gases were measured in association with a series of fires performed in a wind tunnel. The wind tunnel was the main element of the experimental setup. This low-speed wind tunnel has a fan which is driven by 1hp electric motor, which is connected to a micro inverter which controls the wind speed with an output frequency. The fuel bed was 2m long with a width of 0.8 m width. The wind tunnel utilized the experiments to be performed with and without wind. The wind is measured at approximately 30 cm above the fuel bed. To create a reproducible flame front, longleaf pine needles were uniformly distributed to provide a porous fuel bed. Small nursery plants were interspersed in the second meter of the fuel bed. More detail explanation of the fuel bed configuration is provided in the experimental configuration and treatment section (section 1.4). Figure 2 shows the model of the wind tunnel.

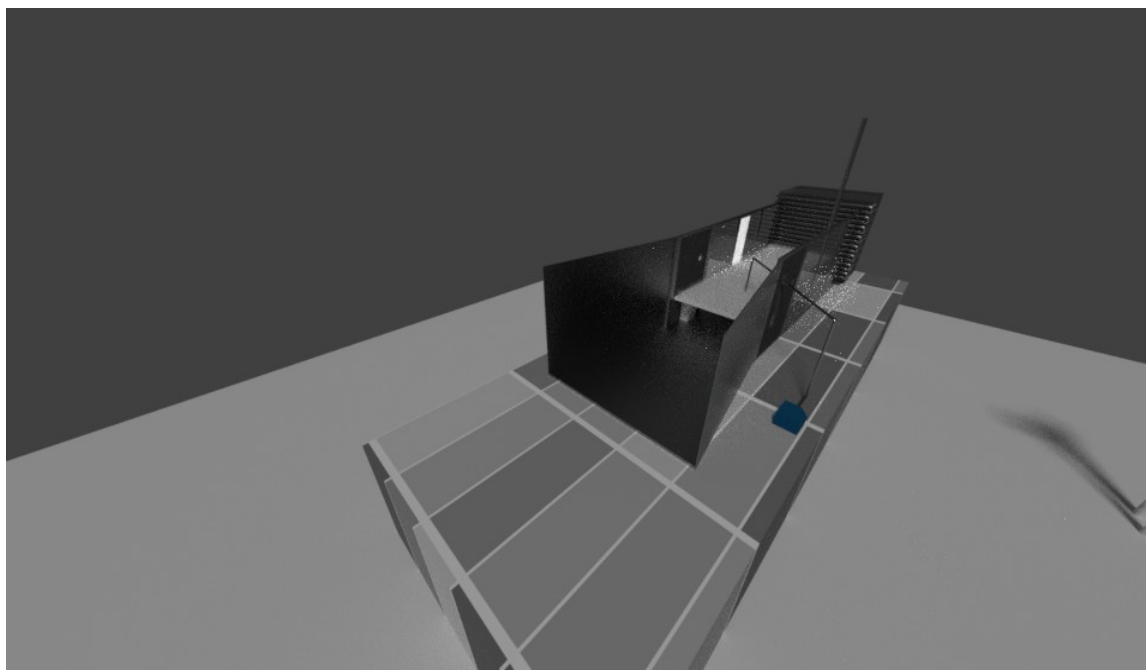


Figure 2. 3D model of the wind tunnel

Instruments were deployed to the wind tunnel to initially capture, measure, and characterize pyrolysis products from the live plant and furthermore, quantify, and evaluate the effects of heat transfer mechanism on the pyrolysis products. The devices that were used for pyrolysis product sampling was a Bruker Tensor T37, Bruker OPAG-22, and TELOPS. In addition to these live sampling instruments, an array of 9 stainless steel tubes were inserted vertically into the fuel bed. these tubes were used to pump the gases into the canisters. The canisters were later analyzed offline using gas chromatography technique

In addition to the gas sampling instruments described, the mass of a single plant, temperature and the relative humidity of the wind tunnel was measured. Moreover, total and radiant heat fluxes at the top of the fuel bed were measured using a Medterm Schmidt-Boelter sensor. The description of these set of instruments are followed

1.3.1 Mass measurement of a single plant

It is important to have a quantitative understanding of the mass loss rate of live nursery plants. Because the amount of mass lost during the pyrolysis process can be correlated to pyrolysis products. Moreover, the mass loss rate can also be used to describe the heat transfer effects on the pyrolysis process. To measure the mass of single live nursery plant, a high precision scale is required to record the mass of the plant with high temporal resolution. The scale used had 1 mg resolution and 6hz sampling rate. A sample of potted nursery plant was placed with care on top of the scale. Because of the high sensitivity of the scale, it was important to make sure that the plant-scale system was not affected by any other foreign objects (i.e., longleaf pine needle and surrounding plants). A model for the scale-plant setup is demonstrated in figure 3

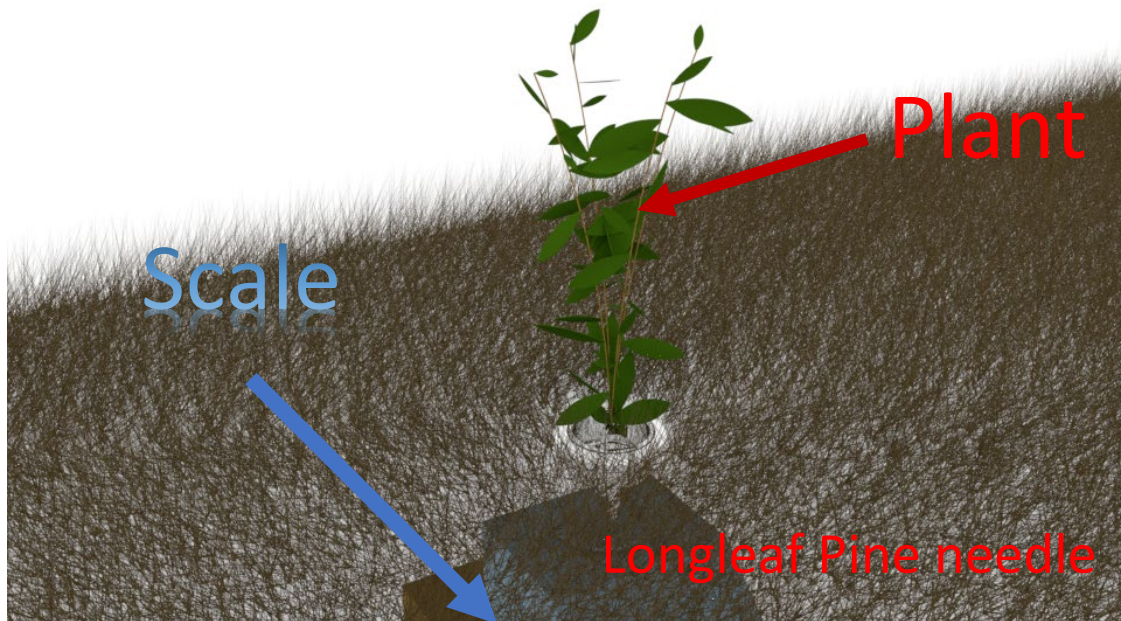


Figure 3. Schematic of Nursery Plant- Scale System

1.3.2 Radiant and Heat flux measurements

The importance of heat transfer has been already emphasized. As mentioned, although there is no instrument which can directly measure radiative and convective heat transfer, convective heat

transfer can be quantitatively calculated by measuring total and radiative heat flux using a Schmidt-Boelter sensor. Two Schmidt-Boelter sensors were placed before and after the plant-scale system . figure 4 shows the position of these instruments

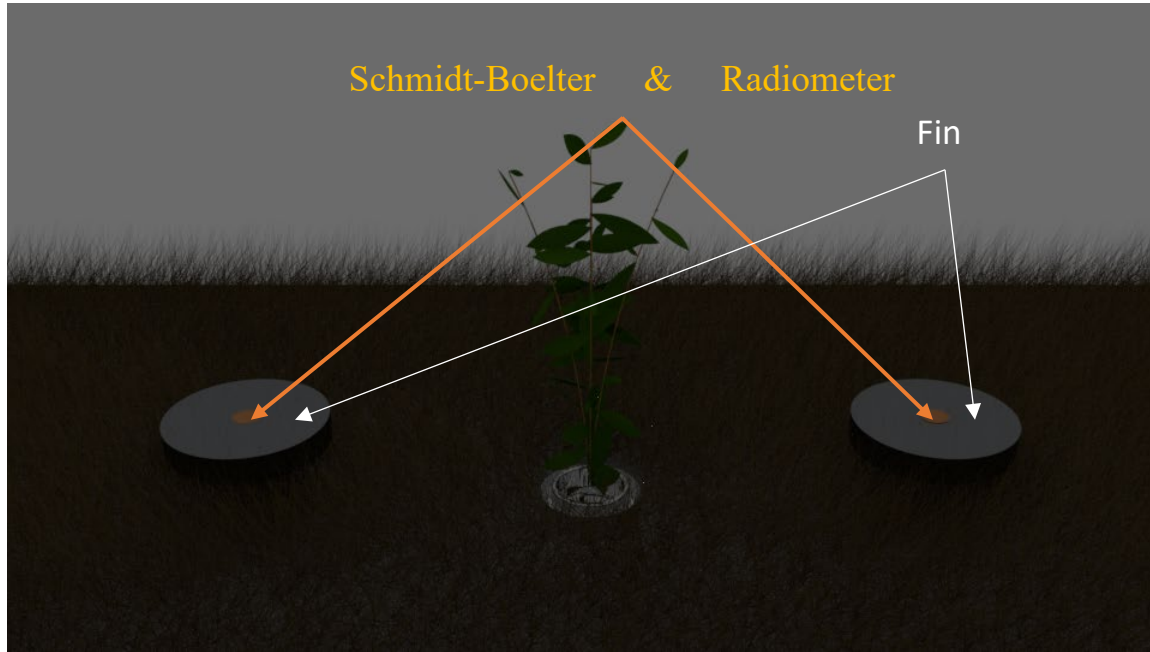


Figure 4. Schematic of Schmidt-Boelter & Radiometer System

The Schmidt Boelter gauges absorb the heat at one surface and transfer the heat in the normal direction to the absorbing surface. The voltage output of the sensor is generated by a thermopile, which it responds to the difference in temperature of the surface and plane beneath the surface. The radiometer on the sensor consists of a purged radiating transmitted window. The voltage output of the radiometer corresponds to the radiation on the surface of the sensor.

To calculate total and radiative heat flux of the sensor, the gauges are calibrated. The calibration equation for the Medtherm gauges used in this system is provided as:

$$Q = AV^B \quad (41)$$

Here V , is the voltage output, A and B are constants defined in table 1. The unit of Q in this equation is kW/m^2 . The sensors are connected to Campbell scientific CR3000 datalogger, to log and record the voltage difference in real time.

Table 1 Calibration constants used in equation 41

Sensor type	Location	A	B
Radiometer	Before scale-setup	5.582660	1.064960
Total (Schmidt-Boelter)	Before scale-setup	7.430203	1.059662
Radiometer	After scale-setup	6.177155	1.076644
Total (Schmidt-Boelter)	After scale-setup	7.900974	1.0660964

1.3.3 Thermocouple system

A system of K-type thermocouples was created to mimic temperature profile around a single plant.

The image of such a thermocouple system is demonstrated in figure 5

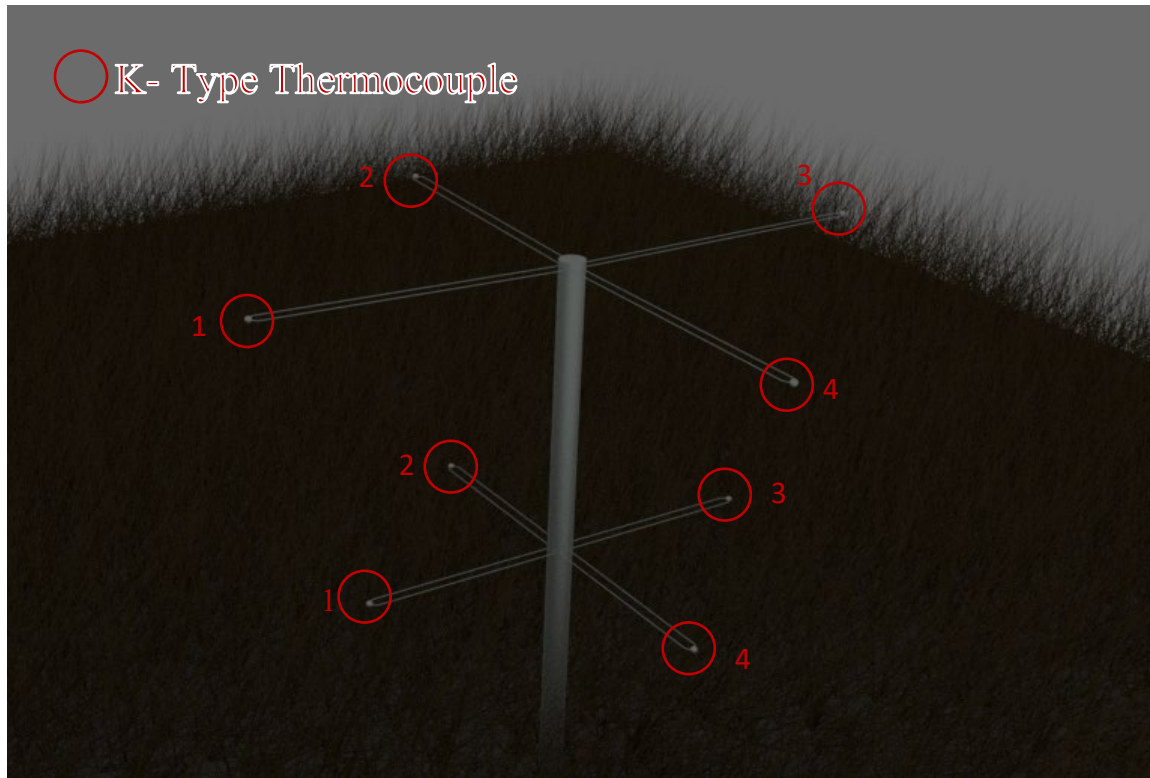


Figure 5. Thermocouple tree system

In the last phase of the experimental configurations, the thermocouple tree system was replaced with 14 thermocouples, which were scattered through the fuel bed. The configuration of this thermocouple setup can be seen in figure 6. This configuration created the opportunity to record the temperature of the gases at the moments that they were analyzed by the FTIR system

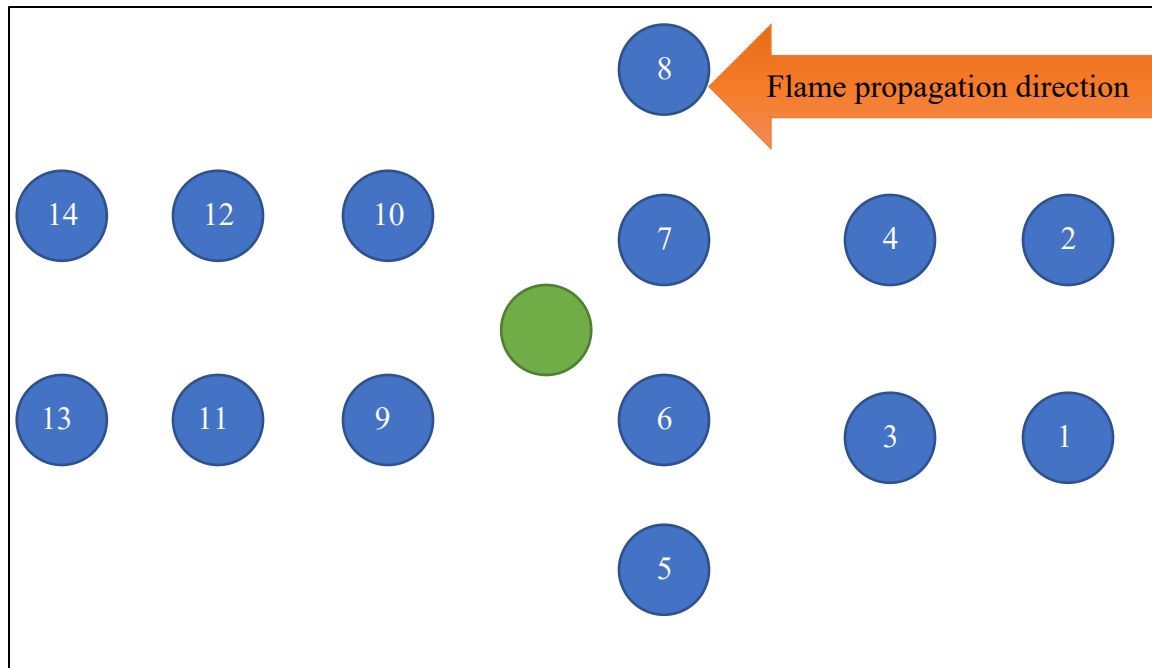


Figure 6. configuration of the thermocouple system for the last phase The blue circle represents the thermocouple location and the green circle shoes the plant-scale setup.

1.3.4 IR imaging

A longwave infrared camera (LWIR) was mounted on top of the wind tunnel to provide the top-view temperature and IR emission mapping of the fuel bed. A sample of the IR emission map is seen in figure 7:

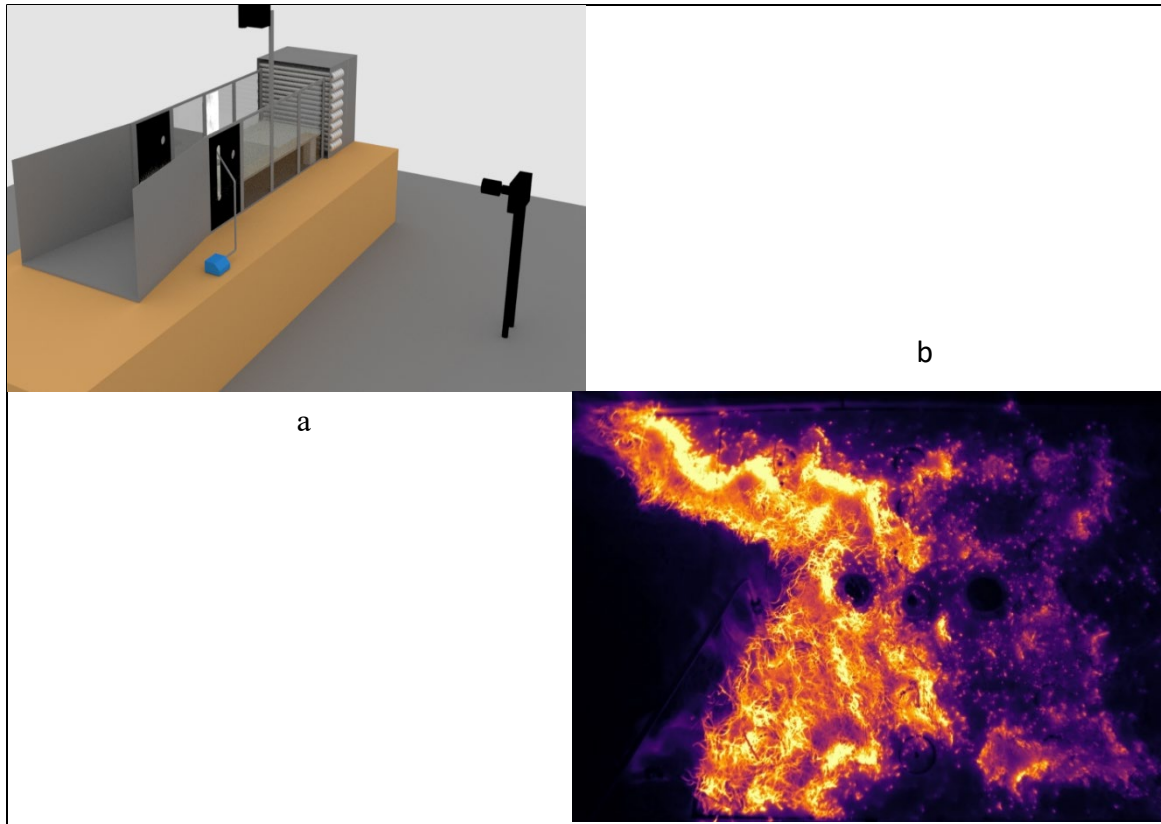


Figure 7. a) IR camera position ,b) IR image Sample

1.3.5 BOS System

The BOS system was constructed as an addition to the tunnel. A simple random noise function generated the background patterns on transparent paper which were placed on a lightbox for illumination. Images were captured using a DSLR camera with a frame rate of 60 frames per second. To capture image distortion, the camera was focused manually on the background noise pattern, and the camera frame was adjusted to maximize the amount of the noise background seen. Figure 8-a shows a schematic of the simple BOS system in the low-speed wind tunnel. Figure 8-b shows an image obtained by the camera. Note the small portion of the fuel bed that was visible.

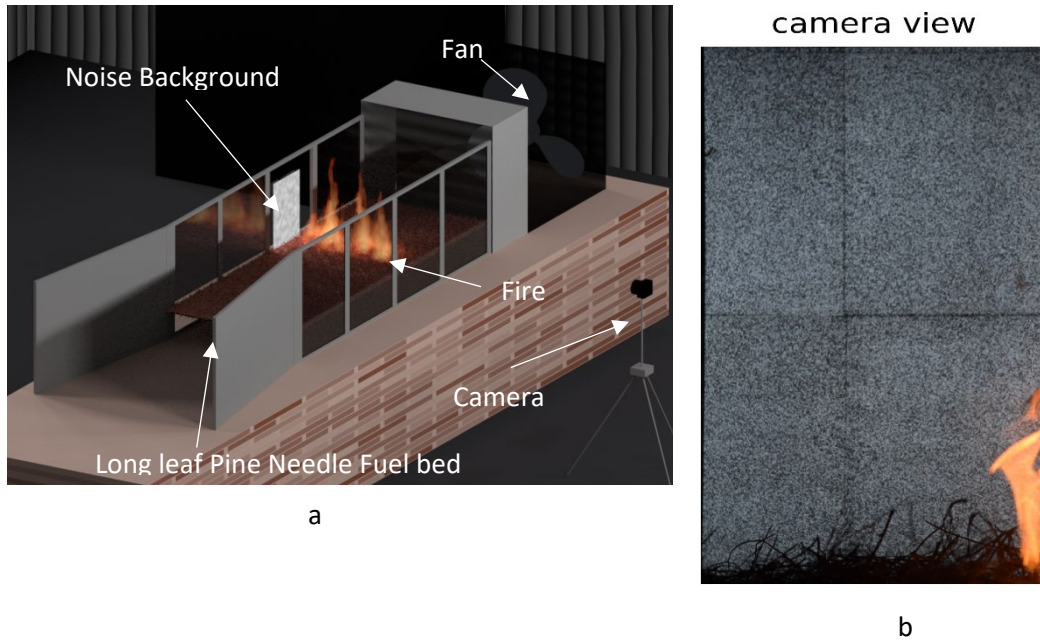


Figure 8. Simple schematic experimental setup. (a) The experimental setup inside the low-speed wind tunnel (b) the image captured by the camera

In order to estimate density gradients, it is also necessary to measure the distances required for the calculation of constant G_1 and G_2 in equations 6 and 7. These distances and other needed parameters are summarized in Table-2. One should keep in mind that these values are dependent on the experimental condition (i.e. $n_\infty, K(\lambda)$) and experimental setup (i.e. Z_D, f, L). Once G_1 and G_2 are known, C_1 and C_2 can be calculated by knowing the value β , which for gases is $1/T_\infty$, where

T_{∞} is the ambient temperature. Also included in the table 2 is Camera Pixel Size which is necessary for calibrating displacement, $\Delta y'$, in equation 6.

Table 2. Properties used to calculate G_1 in equation 6

Property	Value
n_{∞}	1.0023
Z_D	3.28m
f	0.2m
L	0.6 m
$K(\lambda)$	$0.23 \cdot 10^{-3} (m^3/kg)$
Camera Pixel Size	$3.92 \cdot 10^{-6} m$

1.4 Experimental configurations and treatments

A total of 97 fires were burned, and data was collected for BOS and other instruments. Forty-two fires had no wind and fifty-five had an imposed wind. The mean fuel moisture content of the longleaf pine needles was 9.5 ± 0.2 and 10.4 ± 0.3 percent for the wind and no wind fires, respectively. The rate of spread was $12.4 \pm 0.5 \text{ mm/s}$ and $5.3 \pm 0.1 \text{ mm/s}$ for the wind and no wind fires respectively. The experiments were divided into three phases. The detail of each phase is followed

In the first phase, which was the experiments done between November 10th, 2017 to November 18th, 2017, Total of 37 ²experiments were done. In this set of experiments, the ambient conditions were the same as the ambient condition of the building. Out of the total of these 37 experiments, 28 were done without the wind, and the remaining experiments were with the external wind of

² This number corresponds to number of experiments recorded from various Instruments.

0.44m/s. In this phase, 13 different experimental configurations were analysed. Table 3 shows information regarding these configurations

Table 3. Experimental configurations for phase 1 of the study

Live Nursery Plant	Weight of Longleaf Pine needle	Number of experiments	Number of live nursery plants	Wind condition	Notes
Inkberry (Ilex glabra (L.) A. Gray)	800 <i>g</i>	3	41	No Wind	
Inkberry (Ilex glabra (L.) A. Gray)	800 <i>g</i>	3	24	No Wind	
Inkberry (Ilex glabra (L.) A. Gray)	1000 <i>g</i>	2	24	0.44 <i>m/s</i> wind	
Inkberry (Ilex glabra (L.) A. Gray)	1000 <i>g</i>	2	41	0.44 <i>m/s</i> wind	
Inkberry (Ilex glabra (L.) A. Gray)	1000 <i>g</i>	4	24	No Wind	
Inkberry (Ilex glabra (L.) A. Gray)	1000 <i>g</i>	4	41	No Wind	
Inkberry (Ilex glabra (L.) A. Gray)	1000 <i>g</i>	2	34-47	No Wind	
Inkberry (Ilex glabra (L.) A. Gray)	1000 <i>g</i>	3	34-47	0.44 <i>m/s</i> wind	
Fetterbush Lyonia lucida (Lam.) K. Koch	1000 <i>g</i>	4	30	No Wind	Elevated plants
Darrow's blueberry Vaccinium darrowii	1000 <i>g</i>	2	30	No Wind	
Fetterbush& Darrow's blueberry	1000 <i>g</i>	2	31	No Wind	Elevated plants
	1000 <i>g</i>	2		0.44 <i>m/s</i> wind	
	800 <i>g</i>	4		No Wind	

As can be seen from table 3, in most of the experiments, the weight of the pine was 1000 *g*. The main reason for the increase was to have a better fire propagation.

In the second phase, which was the experiments done between February 22, 2018, and March 1st, 2018, a total of 23 experiments were done. In this phase, in contrast with the previous phase, the air was conditioned to mimic the wintertime in the southern united states; thus, the air was kept at

4°C with a relative humidity of (40%). In all these experiments, the wind speed was set to be 0.8m/s. In this phase, four different experimental configurations were analyzed. Table 4 shows information regarding these configurations

Table 4. Experimental configurations for phase 2 of the study

Live Nursery Plant	Weight of Longleaf Pine needle	Number of experiments	Number of live nursery plants	Wind condition
Fetterbush <i>Lyonia lucida</i> (Lam.) K. Koch	1000 <i>g</i>	7	54	0.8 <i>m/s</i> wind
Darrow's blueberry <i>Vaccinium darrowii</i>	1000 <i>g</i>	5	54	0.8 <i>m/s</i> wind
Fetterbush & Darrow's blueberry	1000 <i>g</i>	6	54	0.8 <i>m/s</i> wind
	1000 <i>g</i>	5		0.8 <i>m/s</i> wind

In the third phase, which was the experiments done between October 30th, 2018, and November 2nd, 2018, a total of 24 experiments was done. In this phase, except for one set of the data, the air was not conditioned at it was kept the same as the ambient room condition. In all of these experiments, the wind speed was set to have a value of 0.4 *m/s*. In this phase, four different experimental configurations were analysed. Table 5 shows information regarding these configurations

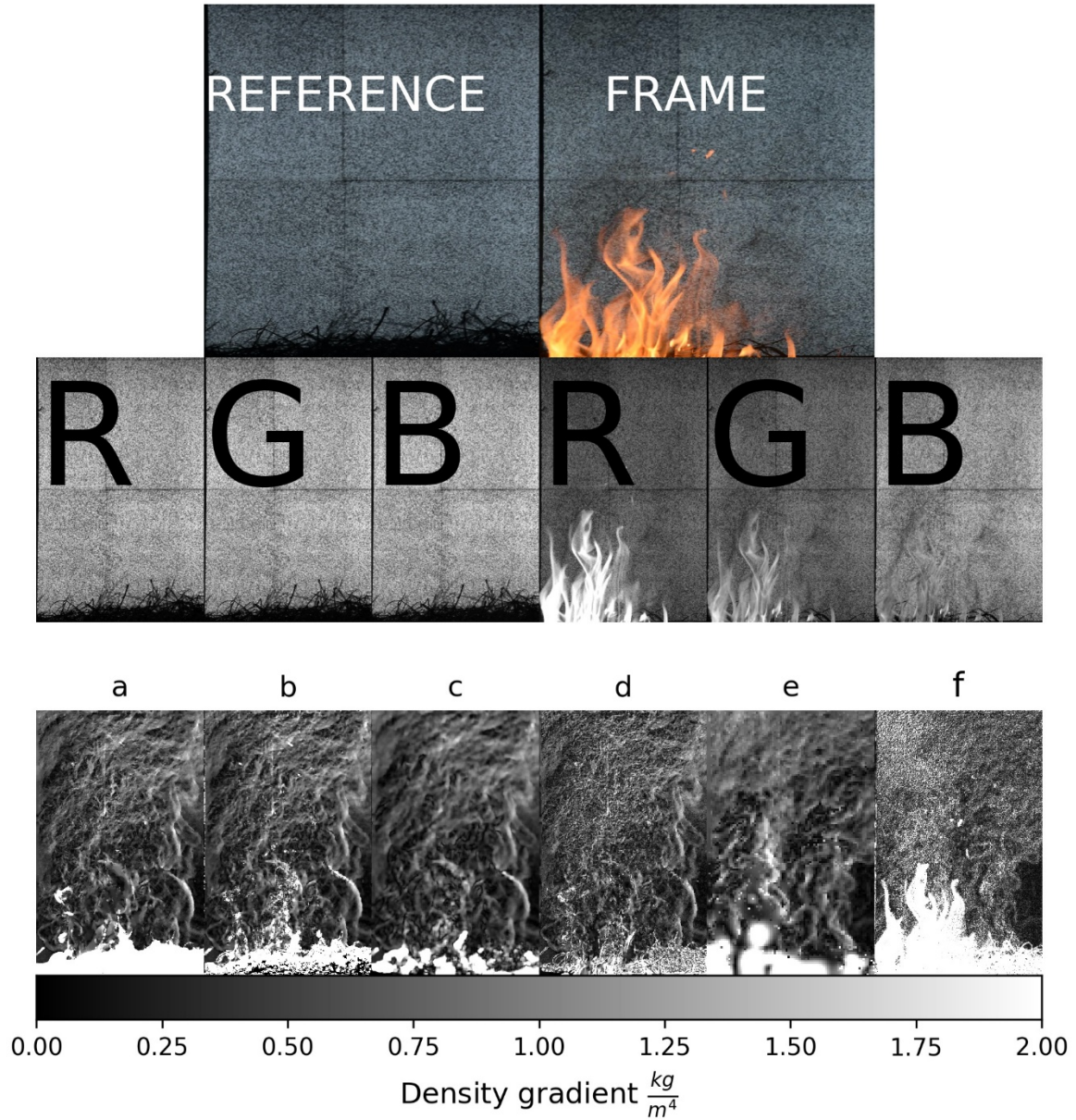
Table 5. Experimental configurations for phase 3 of the study

Live Nursery Plant	Weight of Longleaf Pine needle	Number of experiments	Number of live nursery plants	Wind condition
Fetterbush Lyonia lucida (Lam.) K. Koch	1000 <i>g</i>	8	74	0.44 <i>m/s</i> wind
Sparkleberry Vaccinium arboreum Marshall	1000 <i>g</i>	8	74	0.44 <i>m/s</i> wind
Inkberry (Ilex glabra (L.) A. Gray)	1000 <i>g</i>	6	74	0.44 <i>m/s</i> wind
	1000 <i>g</i>	2		0.44 <i>m/s</i> wind

1.5 BOS Data Analysis

1.5.1 Flow Visualization

In the first step, we applied the optical flow algorithms that were discussed in section 1.21.A. The displacement was calculated by comparing the images of a distorted and undistorted background. The blue channel of the three-channel (RGB) DSLR camera image showed less detail of the flame itself, leading to a greater number of meaningful data points. The optical flow algorithms estimated the displacement in x and y directions ($\Delta x, \Delta y$), which were related to $\partial \rho / \partial y$ and $\partial \rho / \partial x$ using equation 6. For visualization purposes, the magnitude of the density gradient vector $\nabla \rho$ was calculated and visualized in Figure 9. The first row shows the raw image of the flame and the undistorted reference frame. The second row shows red, green and blue channels of both images. The third row demonstrates the calculated magnitude of the density gradient vector $\nabla \rho$ using different optical flow algorithms and block matching algorithm. From the images, the Farneback algorithm produces a smoother visualization with less visible noise compared to all other algorithms.



a) Brox , b) Lucas-Kanade , c) Farneback
d) Dual TV L1 , e) Block matching , f) Horn-Schunck

Figure 9. Imagery, color channels (red, green, blue) and calculated magnitude of density gradient for different optical flow algorithms

1.5.2 Density Gradient Image Velocimetry

Quantitatively the visualizations developed in the previous section provide data on the density gradient and do not provide information about the velocity structures of the flow field. Since

velocity is crucial to understand the flow behavior in different conditions, velocimetry techniques which use BOS have been proposed [61, 62]. Bühlmann et al. [61] suggested that “PIV analysis” of the BOS displacement field (using density gradient data as tracing particles) could be performed to estimate local convective velocities spatially. Most of the velocities obtained by “PIV-analysis” of the displacement field represent the velocities of the bigger structures of the flow field with no details at small scale due to the lack of resolution [63]. One main reason for this lack of resolution is that the “PIV analysis” commonly uses a block matching algorithm for its calculation. Since optical flow algorithms have a higher spatial resolution, they were applied to the displacement data set. Since density gradient data has been traced, we refer to this methodology as Density Gradient Image Velocimetry (DGIV). Furthermore, the density gradient data were vectors. Thus, calculation of the displacement vectors required a separate displacement calculation for each vector component.

As in density gradient calculation, algorithms that are sensitive to all the scales of motion are required. As discussed in section 1.2.1.A, this group of optical flow algorithms uses a multiresolution coarse-to-fine algorithm called an image pyramid. An image pyramid is made by repeatedly downsampling an image by a given factor. This factor can have any value smaller than one and depends on the image size and the sensitivity of the deployed algorithm. The optical flow was found on the smallest image in the pyramid and is used to unwarp the next smallest image. Interpolation was used for the fractional pixel locations. This process was then iterated until reaching the original image resolution [64]. Brox, TV-L1, and Farneback algorithms incorporate this procedure. We used the Brox algorithm because it takes into account conservation of brightness gradients.

Figure 10 demonstrates the procedure of vector field computation. The top left box shows the two consecutive raw images of the flame and the density gradient field computed using the Farneback algorithm. The top right plot shows the velocity vector field calculated using the Brox optical flow algorithm applied to the density gradient field. The bottom box shows magnification of the four boxed areas from the vector field superimposed on the density gradient magnitude.

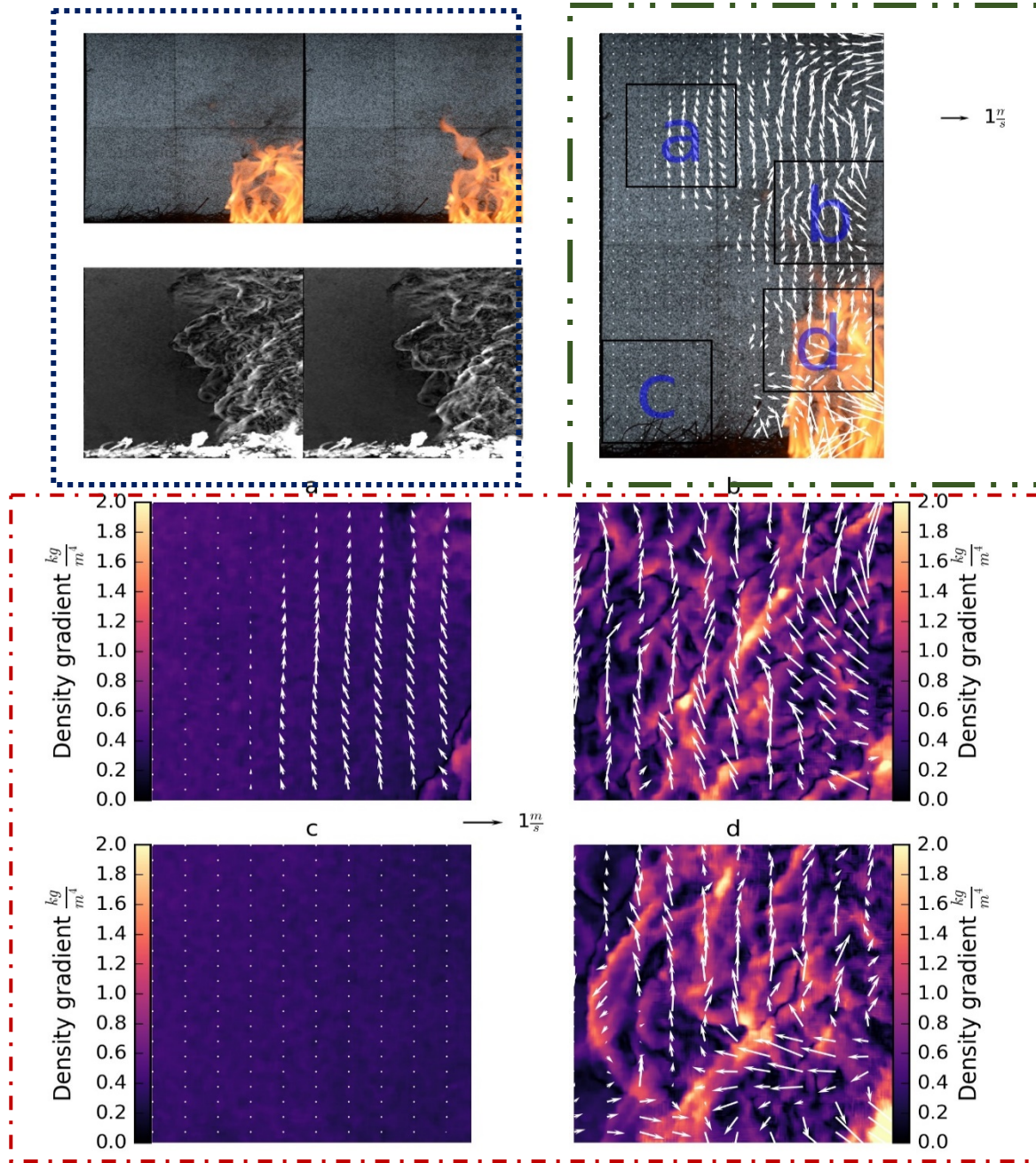


Figure 10 Illustration of vector field calculation

1.5.3 Estimation of Convective Heat Transfer using BOS

The density gradient data and the velocity vectors could be used to estimate density, temperature, and subsequently convective heat transfer. However, this methodology is computationally expensive. Since convective heat transfer is generally related to the turbulent motion in the flow

field, visualization of the turbulent structure could provide information on convective heat transfer. Following this idea, Hargather and Settles [65] proposed a new method of processing BOS images. They suggested processing of two different flow field images relative to one another instead of comparing a disturbed and undisturbed image of the noise background. This procedure reveals only the changes caused by fluctuation in the refractive flow field between the two images. Hargather and Settles further suggested that this technique visualized the turbulent part of the thermal plume. Using Hargather and Settles [65] rational, we propose a methodology to correlate fluctuations in the flow field to convective heat flux. Rewriting equation 2 as

$$\epsilon_y = \frac{1}{n} \int \frac{\partial n}{\partial y} dz = -\frac{L \cdot \rho_\infty \cdot \beta \cdot K(\lambda)}{n_\infty} \left(\frac{\partial T}{\partial y} \right) \quad (41)$$

Equation 41 shows that the deflection angle, ϵ_y is a function of the temperature gradient. According to Fourier's law heat flux is caused by a temperature gradient, therefore here we rewrite Equation 3-12 as

$$\epsilon_y = \frac{1}{n} \int \frac{\partial n}{\partial y} dz = \frac{L \cdot \rho_\infty \beta \cdot K(\lambda)}{n_\infty} \cdot \frac{q_y}{k} \quad (42)$$

Here k is the thermal conductivity and q_y is the heat flux density in the y direction. In this way (42) we related heat flux to the deflection angle. When convective heat transfer is present, heat flux density q can be written as:

$$\frac{q}{k} = -\nabla T - \frac{1}{\alpha} \cdot \overline{u' T'} \quad (43)$$

Here α is the thermal diffusivity and u' and T' are velocity and temperature fluctuations. The additional term represents the heat transfer caused by turbulent convection. Considering only convection, $-\nabla T$ can be ignored resulting in equation 44.

$$\epsilon_y = \frac{1}{n} \int \frac{\partial n}{\partial y} dz = -\frac{L \cdot \rho_\infty \cdot \beta \cdot K(\lambda)}{\alpha \cdot n_\infty} \overline{u' T'} = -\frac{L \cdot K(\lambda)}{\alpha \cdot n_\infty} \overline{u' \rho'} = -\frac{L}{\alpha \cdot n_\infty} \overline{u' n'} \quad (44)$$

Equation 44 demonstrates that when a light ray travels in the z direction and intersects a region of convective flow, the light will bend. This is the same phenomenon where an optical wave propagating through a medium experience irradiance (intensity) fluctuations also known as optical turbulence. Combining equation 44 with Hargather and Settles [65] methodology and applying the same steps used to developing equations 6 and 7, convection can be correlated to calculated displacement vectors as

$$\overline{u' \rho'} = -\frac{\alpha \cdot n_\infty Z_B}{K(\lambda) \cdot Z_D \cdot f \cdot L} \Delta y' = -\alpha \cdot G_1 \cdot \Delta y' \quad (45)$$

$$\overline{u' \rho'} = -\frac{\alpha \cdot n_\infty}{K(\lambda) \cdot Z_D \cdot L} \Delta y = -\alpha \cdot G_2 \cdot \Delta y \quad (46)$$

It has to be noted that displacements in equation 45 and 46 are calculated by comparing two consecutive frames of BOS image.

1.5.4 Data Processing result for a single experiment

Applying the procedures described above, the thermal plume derived velocity field, and estimated convective flux for flames subjected to two wind conditions are presented. This section provides a general understanding of the flow field and convective thermal plume around, and the interpretation for an individual Experiment.

1.5.4.A Visualization of the Thermal Plume of Propagating flame

For the flow visualization, 11,600 images were processed for a single burn. Since it is not feasible to show all these data, six images are shown in figure 11 for a no wind fire. In the images, the flame propagated from right to left; however, image 1 occurred in the time before image 2. For

visualization purposes, all calculated properties were normalized to have a value between 0 and 255 in the video files. Due to the slow rate of spread of the flame, 100 to 200 seconds after ignition, the flow was seen moving from left to right. This flow was caused by natural entrainment of air towards the flame. As the flame entered the field of view, the thermal plume associated with the flame could be seen. Looking closely at the flame in the left image, the noise patterns around the flame flickered and moved. The optical flow algorithm captured this distortion to visualize the thermal plume. When the fire left the field of view around 250 seconds after ignition, air entrainment towards the plume could be visualized again. Also, the heat flux from non-combustible ash from the burned pine needles caused small thermal plumes.

In the second experimental set, the external wind speed was set to 0.44 m/s . Figure 11-b demonstrate the results of these experimental set. The initial frames of video 2 occur before the ignition time. Shortly after ignition, the thermal plume ahead of the flame became visible for 60 seconds until the flame reached the field of view. The direction of the thermal plume was in the same direction as of the wind but as the flame approached the field of view, the thermal plume was more aligned with the direction of the flame due to the strong buoyancy force. Even though, the Byram's convective number [66, 67] for this case was calculated to be 67, which indicates the presence of high radiation power, BOS visualized an strong convective flow ahead of the flame. After 141 seconds from the ignition, as the flame passed the field of view, the wind was visualized. Since the ashes from the burnt fuel had higher temperatures than the ambient wind, a turbulent thermal boundary layer formed behind the flame.

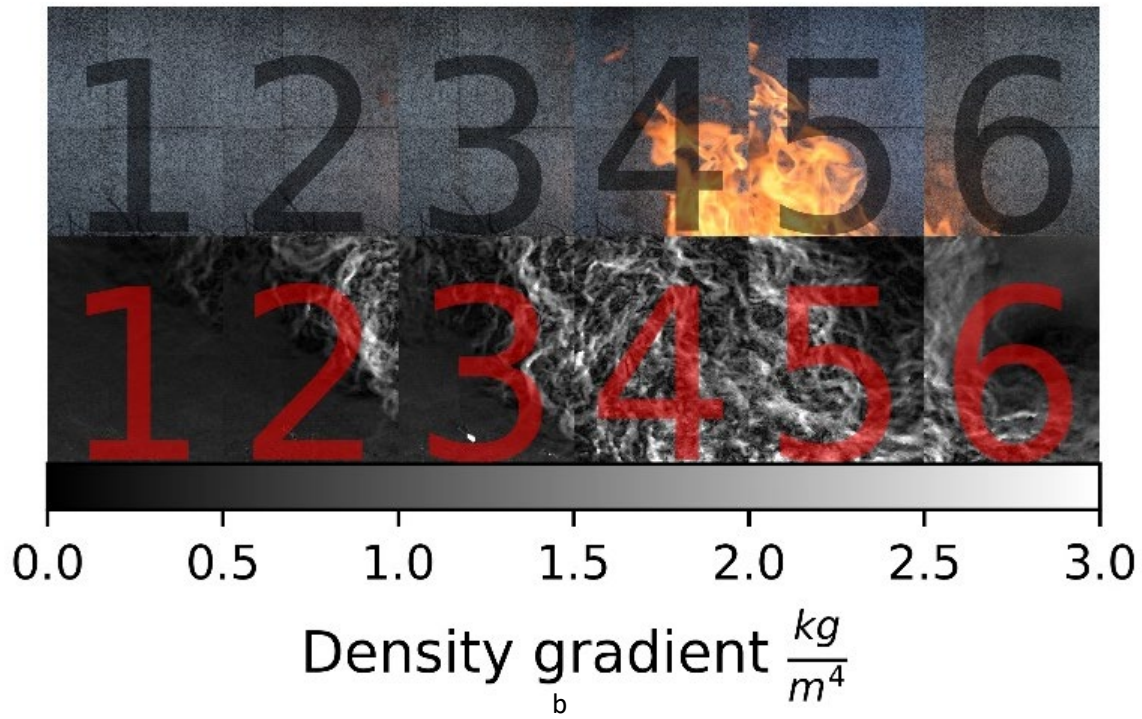
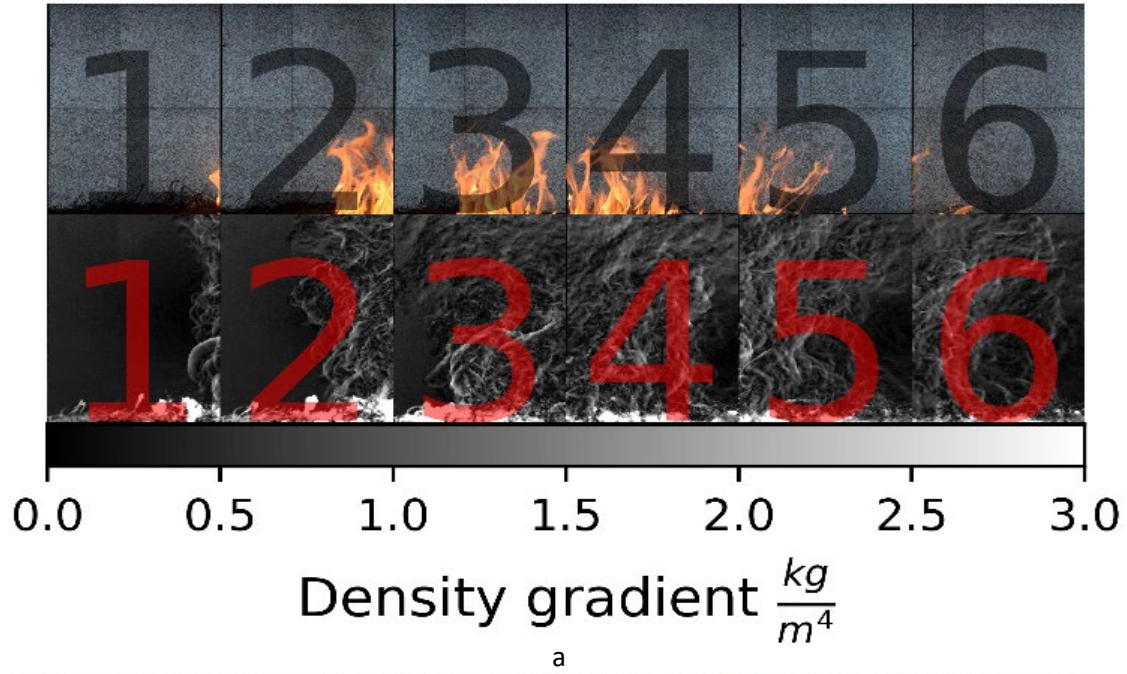


Figure 11 six snapshots of fire propagation in a vegetative fuel bed. (a) without the presence of wind (b) when an external wind of $u = 0.44 \text{ m/s}$ is present

1.5.4.B Velocity Profile of Propagating Flame

The results of applying the DGIV algorithm to the images in figure 11 can be seen in figures 12 (no wind) and 13 (with wind). These images provide a general representation of the velocity field as the fire propagated in the fuel bed. The velocity profile was also evaluated along a vertical transect (black lines) that were selected to give a general understanding of the velocity vectors relative to flame location. With DGIV, if there was no density gradient, no fluid motion of the fluid could be detected.

When no wind was present, the fire was buoyancy-driven, and the main motion of the thermal plume was upward. Because of baroclinic vorticity, vortices were generated next to the flame. These phenomena can be seen in the velocity vectors. The transect velocities in image one and two show the buoyancy-driven upward motion of hot gases in front of the fire. In the third and fourth image, the transects were located inside the plume. The velocity vectors showed a strong upward motion of the plume as well as the horizontal motions caused by baroclinic vorticity and turbulent convection. The transect velocities in the fifth and sixth images show velocity vector on the lee side of the fire plume.

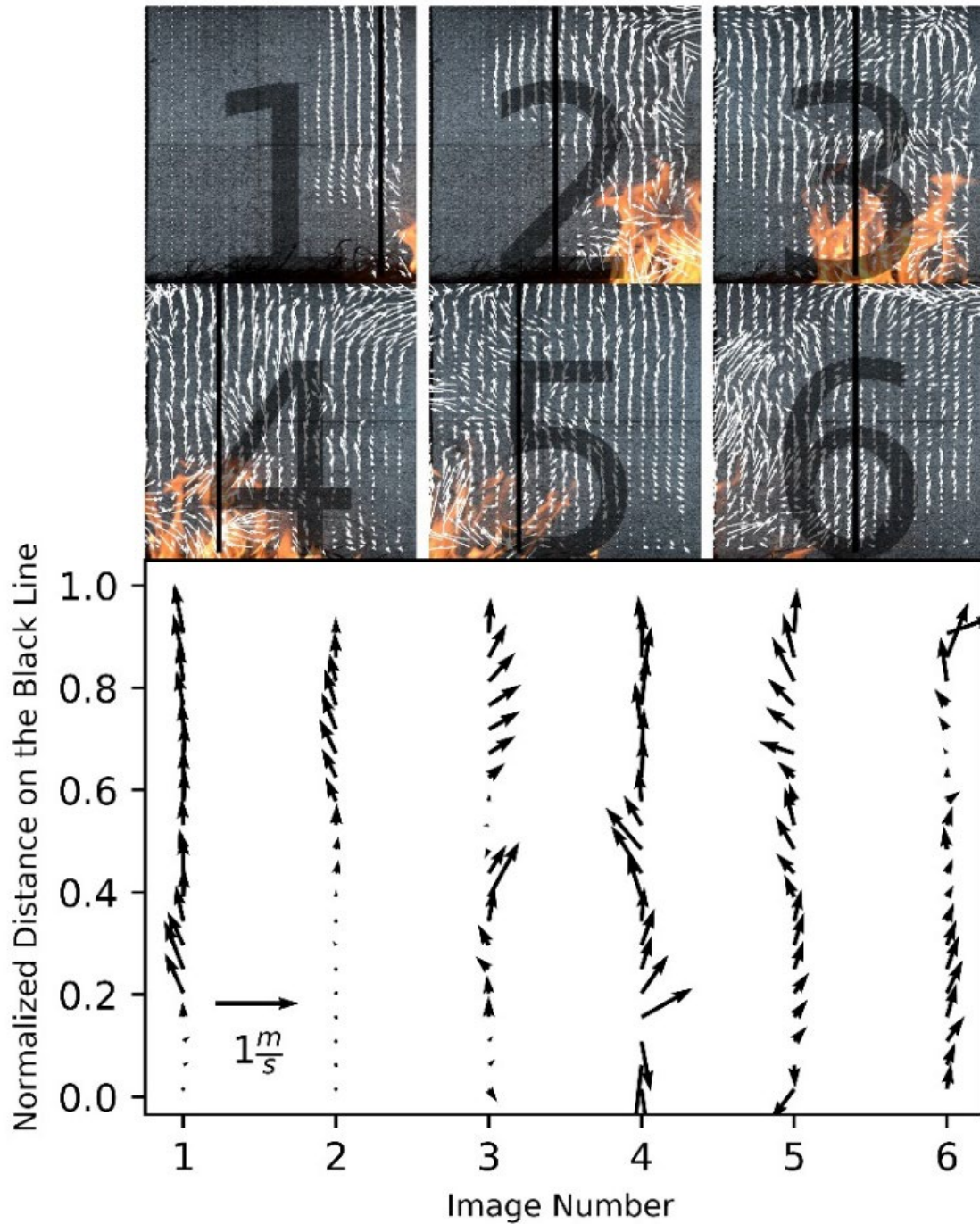


Figure 12 Velocity vector field of fire propagating in vegetative fuel when no wind is present

Figure 13 showed the fire propagation when 0.44 m/s wind was present. Under this condition, also known as wind-driven fire, the direction of motion of the thermal plume was more horizontal and aligned to the direction of the wind. The velocity vectors captured the effect of wind, especially

before flame entered the field of view. The transect vectors in the first three images show the motion of the wind-driven fire ahead of the flame before the flame entered the field of view. In image 4, the velocity transect was located a short distance ahead of the flame. The transect vectors demonstrated the combination of vertical motion due to buoyancy and horizontal motion caused by the wind. In image 5, the transect was at the close distance before the plume. The vectors captured the combination of horizontal entrainment caused by the wind, along with buoyant motion caused by hot remaining ashes. In Image 6, the transect vectors were further removed from the flame, and they captured the horizontal wind motion close to the surface.

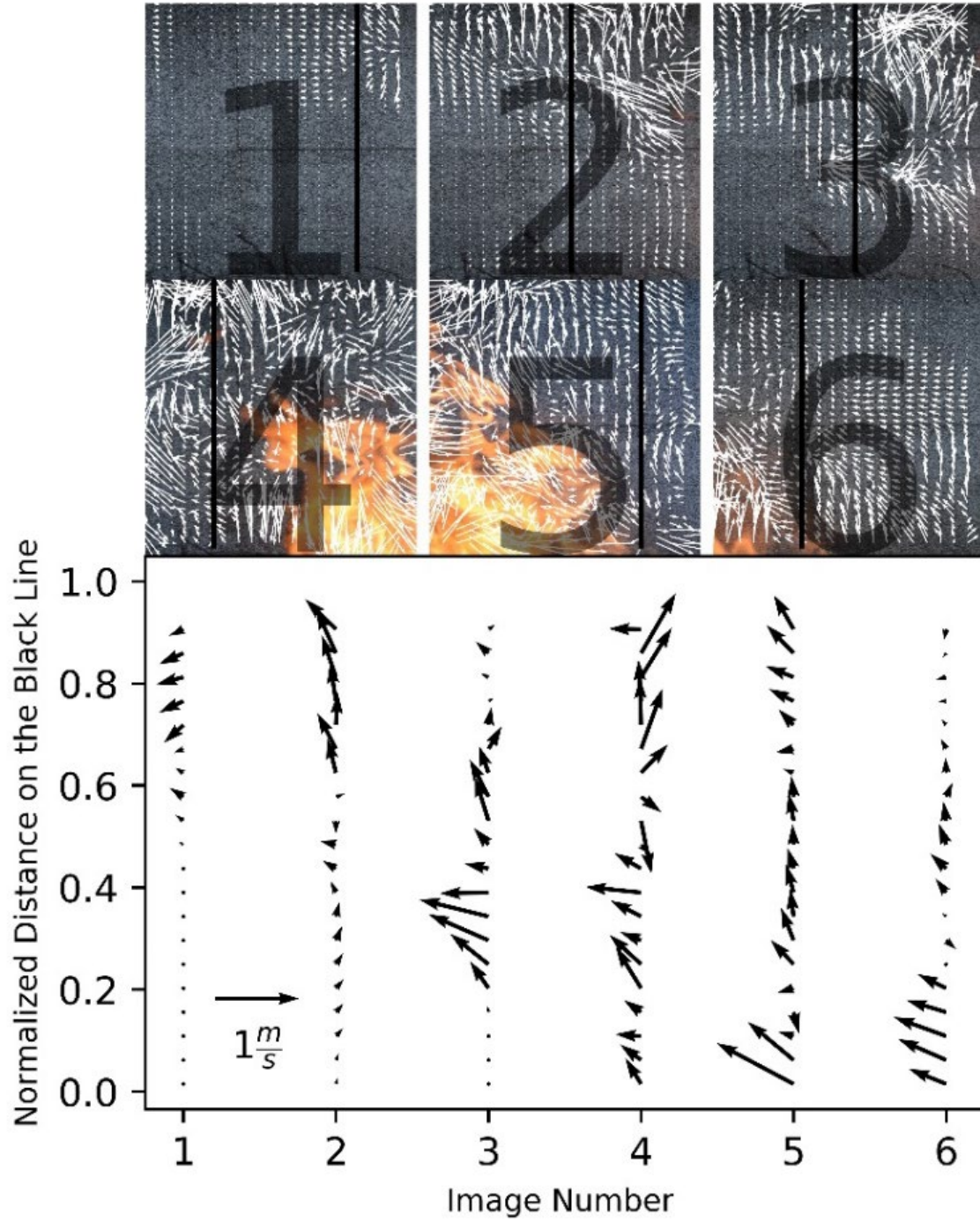


Figure 13 Velocity vector field of wind-driven fire.

1.5.4.C Estimation of convective heat flux ahead of propagating flame

Applying the model developed in equation 45 and 46 to the dataset of the propagating flame, convective heat flux can be calculated assuming $q = T_{\infty} c_p \overline{u' \rho'}$. Where T_{∞} is ambient temperature

and c_p is specific heat of air. Figure 14 illustrates the convective heat flux derived from figure 11. When no wind was present, the convective heat transfer structures were closer to the flame itself. In the wind-driven fire, convection was ahead of the flame. Convective heat transfer increased as distance to the flame decreased. The calculated value shown in figure 14, demonstrates the convective preheating of the fuel bed. These values are based on various assumptions such as the convective profile is constant in line of sight axis (z axis in figure 1). Nevertheless, the presented methodology visualizes the convective heat transfer ahead of the fire and it can be used to understand the effect of wind on preheating of the fuel bed.

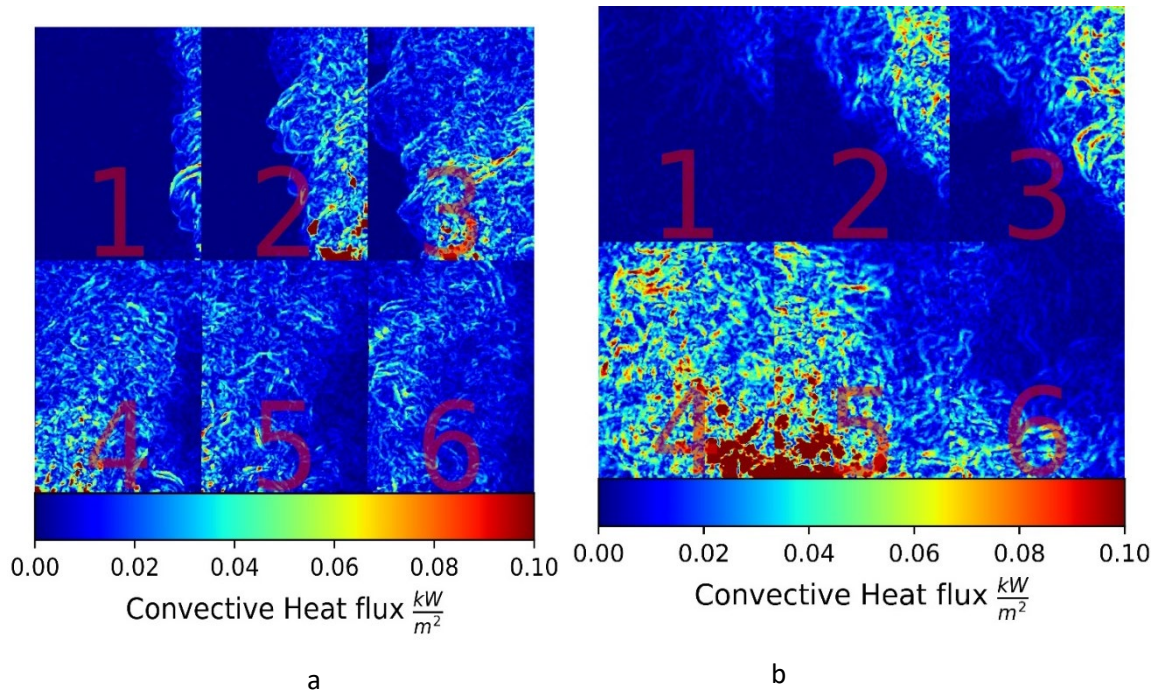


Figure 14 Convective heat transfer around a fire propagating in a vegetative fuel bed. (a) without the presence of wind (b) when the external wind of $u = 0.44 \text{ m/s}$ is present

In the previous section, the thermal plume and velocity vectors associated with the fire was visualized and calculated. Furthermore, our purposed methodology, which was introduced in section (1.5.3) was deployed to visualize and estimate convective heat transfer of hot gases around the flame using consecutive BOS images. It has been seen that wind forces the thermal plume

ahead of the flame. The presence of convective eddies ahead of the flame enhances preheating of fuel. To quantitatively understand the effect of wind on thermal convection in front of the flame, the convective heat flux profile was analyzed in three different distances from the flame. Moreover, in addition to the experimental sets presented in this section, a third case is also introduced, in which the wind speed is increased to 1 m/s and the ambient temperature is reduced and kept at $4.4\text{ }^{\circ}\text{C}$. For this comparison, images with approximately the same flame geometry were compared. The selected frames along with the density gradient profile and convective heat flux profile can be seen in figure 15. The calculated values on these lines can be seen in figure 15.

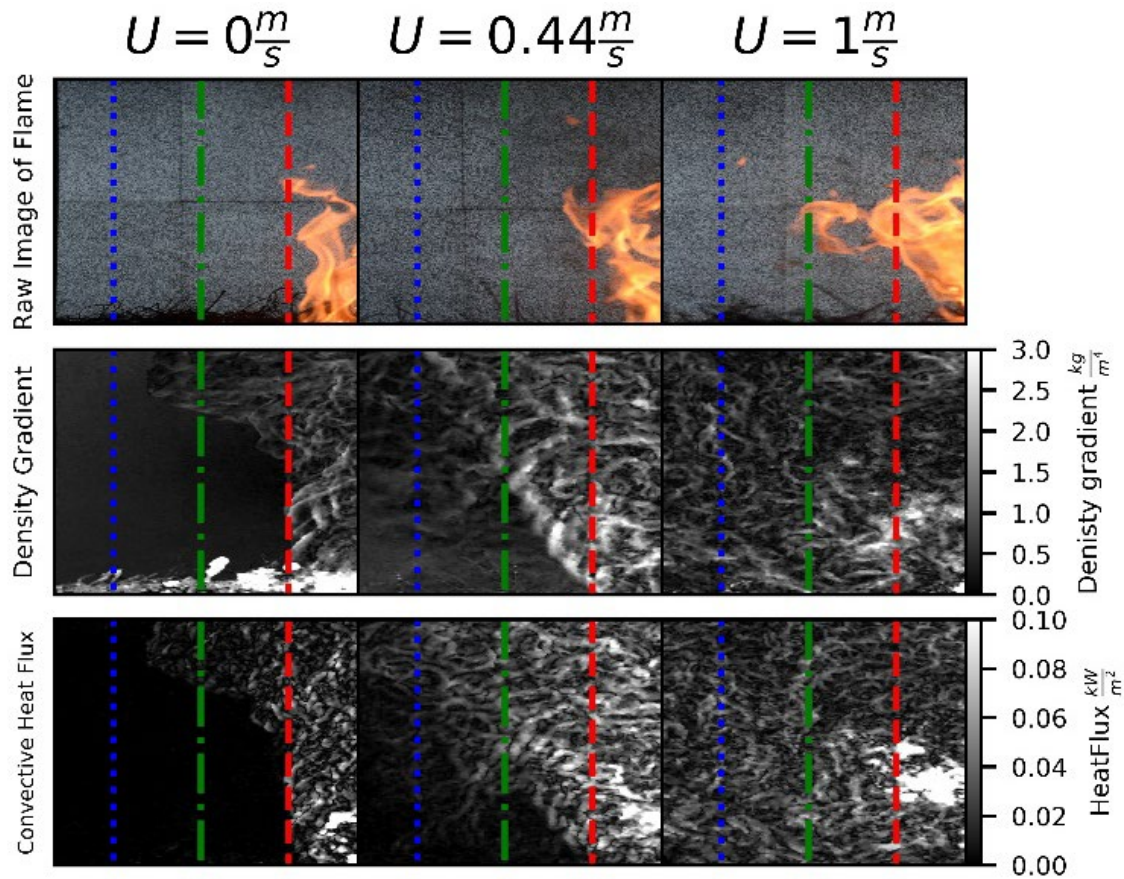


Figure 15 Comparison of thermal plume around the fire in different wind condition. Each column represents the wind condition. The first row is the raw frame of the image. the second row is the magnitude of the density vectors, and the third row is the measured convective heat flux. The vertical red line is approximately 3.375 cm, the green line is approximately 13.5 cm, and the blue line is approximately 21.477 cm ahead of the flame.

It can be seen from figures 15 and 16, for approximately the same flame geometry, the presence of wind increases convective heat flux. Moreover, higher the wind speed, more area the convective thermal plume ahead of flame covers.

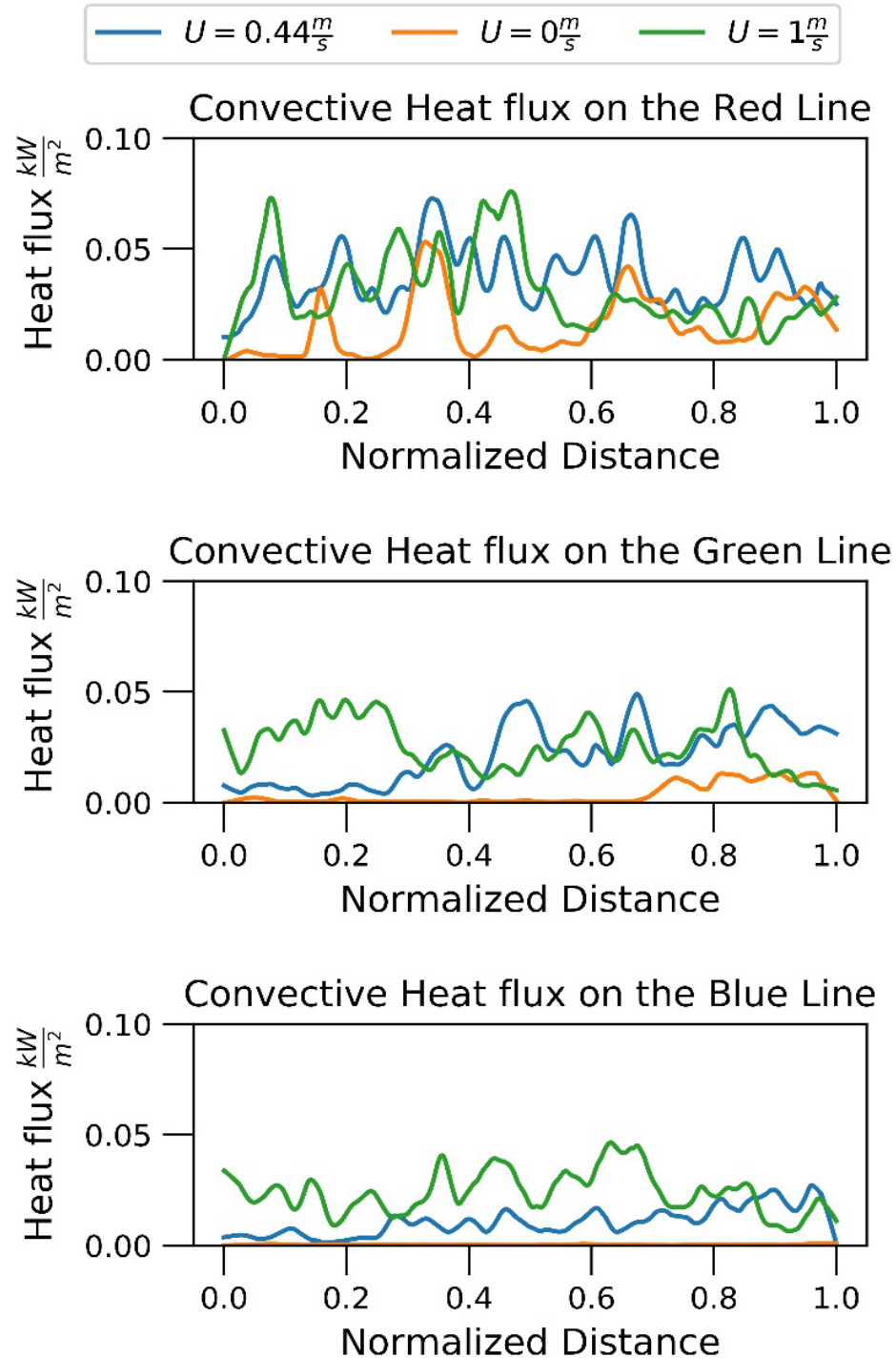


Figure 16 evaluation of convective heat flux on the red, green, and blue line in figure 15. It can be seen heat flux decreases farther away from the flame. Also, it can be seen, higher the wind speed higher the heat flux is ahead of the fire

BOS is based on the fact that hot gases around the fire plume have different density compared to the surrounding fluid. These fluctuations cause changes in the refractive index, which is the reason

for the background image to get distorted. When applying BOS to reacting flow, the changes in density is not solely caused by changes in temperature. The products of the combustion reaction are gases that have a different density than air. Therefore, since the exact compositions of gases are unknown, it was more relevant to analyze the density gradient and fluctuations rather than changes in temperature. In reactive flows, it is a good assumption that when comparing two consecutive frames of images, turbulent mass and heat transfer are equal. Development of equation 45 is based on this assumption.

1.5.4.D Flow Visualization and convection measurement for Live Vegetative Fuel Beds.

As it was indicated in the previous sections, small nursery plants were interspersed across the fuel bed. The plants used in these experiments were from southern united states and from Lyonia, Vaccinium and Ilex species. The experiments were done with and without the presence of external wind. As the fire propagated through the fuel bed, the BOS system was able to capture density variations ahead of the flame front by comparing distorted and undistorted background images. Comparison two consecutive frames of images helped to understand convective behavior of the thermal plume.

For the first set, inkberry (*Ilex glabra*) was distributed in the pine needle fuel bed. Figure 17 shows the result of BOS imagery of Inkberry. The red dotted region identifies the plant location. Since the plants are small, its foliage was buried under the pine needle fuel bed. The ambient temperature was 25°C with a dew point of 6°C. The wind speed was kept at 0.44 m/s.

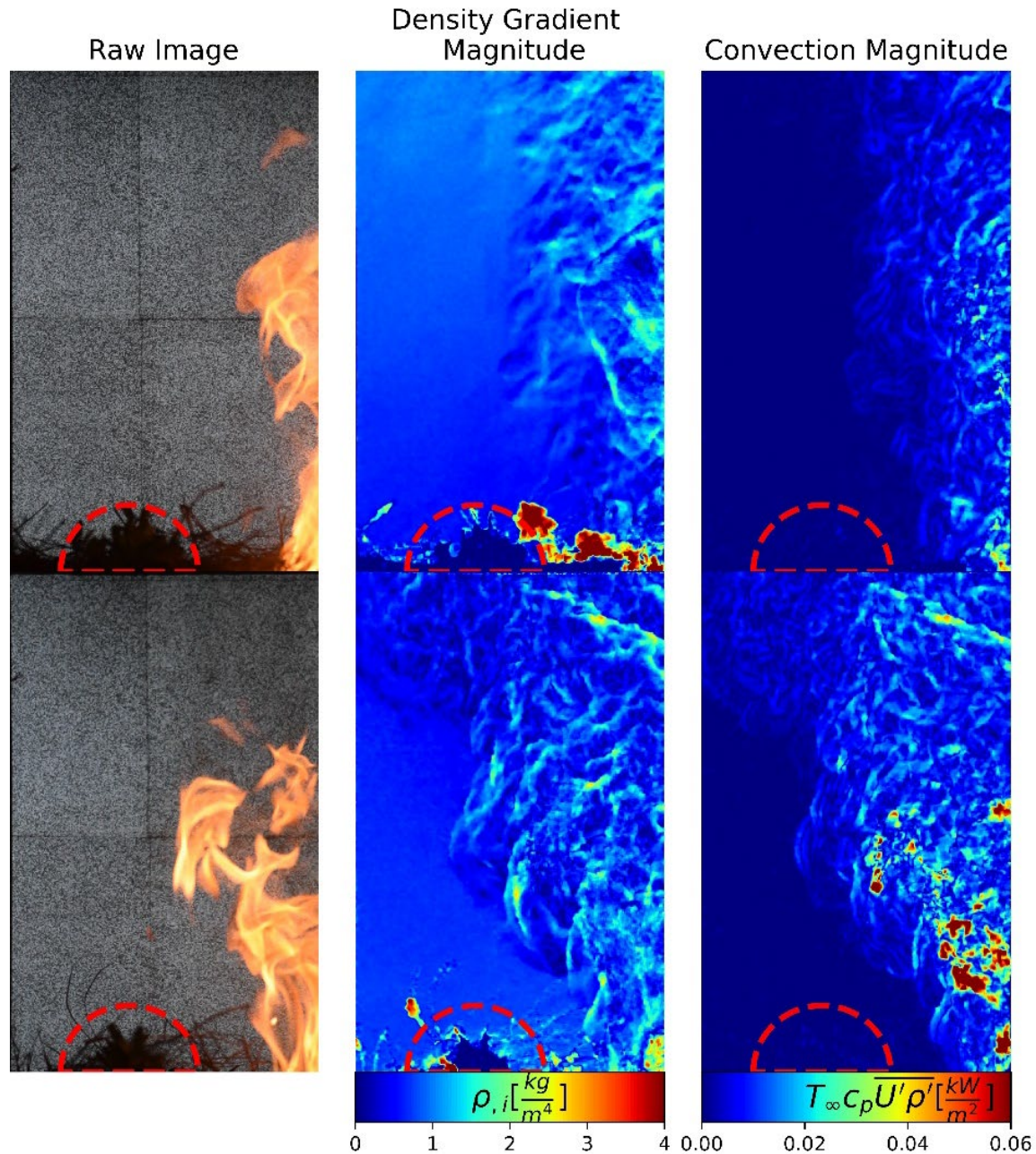


Figure 17 Visualization of the thermal plume and convective plume around the fire. The live fuel is Inkberry (*Ilex*). The first row represents the cases without the presence of external wind, and the second row shows the case was 0.44 m/s wind was present. The red dotted line shows the plant location.

In the second set, Darrow's blueberry (*Vaccinium darrowii* Camp) was distributed in the pine needle fuel bed. In the no wind case, the ambient temperature was 27°C with a dew point of 9°C.

In the presence of external wind of 0.66 m/s, the ambient temperature was set to 4°C with a dew

point of -9°C. Compared to Inkberry, blueberry had taller foliage resulting in some branches to be higher than the pine needle fuel bed. Figure 18 shows the result of BOS imagery of blueberry.

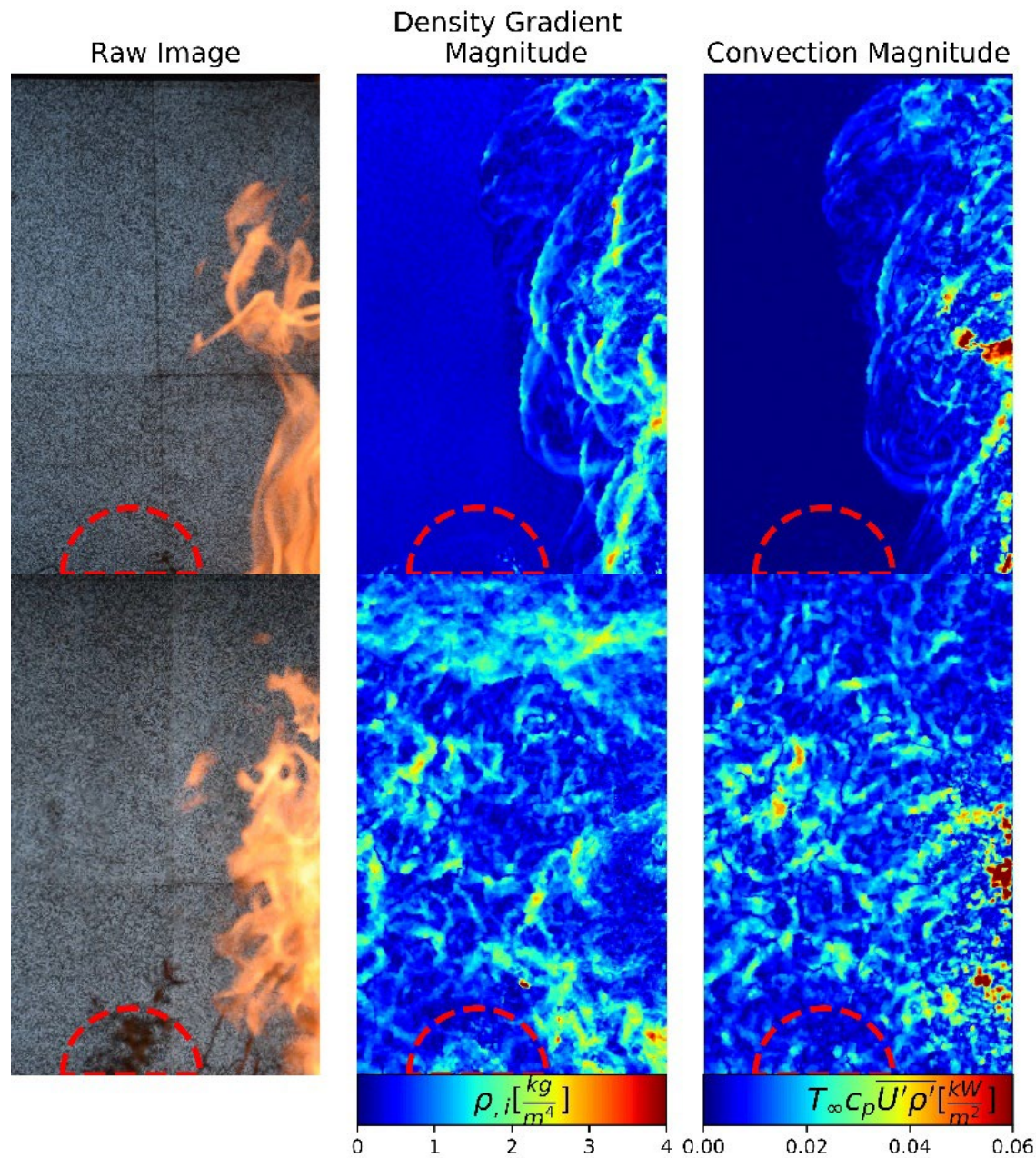


Figure 18 Visualization of the thermal plume and convective plume around the fire. The live fuel is Blueberry (*Vaccinium*). The first row represents the cases without the presence of external wind, and the second row shows the case was 0.8 m/s wind was present. The red dotted line shows the plant location.

In the third set, Fetterbush (*Lyonia lucida*) was distributed in the pine needle fuel bed. In the no-wind case, the ambient temperature was 27°C with a dew point of 9°C. In the presence of external

wind of 0.8 m/s the ambient temperature was set to 4°C with a dew point of -9°C . Compared to Inkberry, blueberry had taller foliage resulting in some branches to be higher than the pine needle fuel bed. Figure 19 shows the result of BOS imagery of Fetterbush.

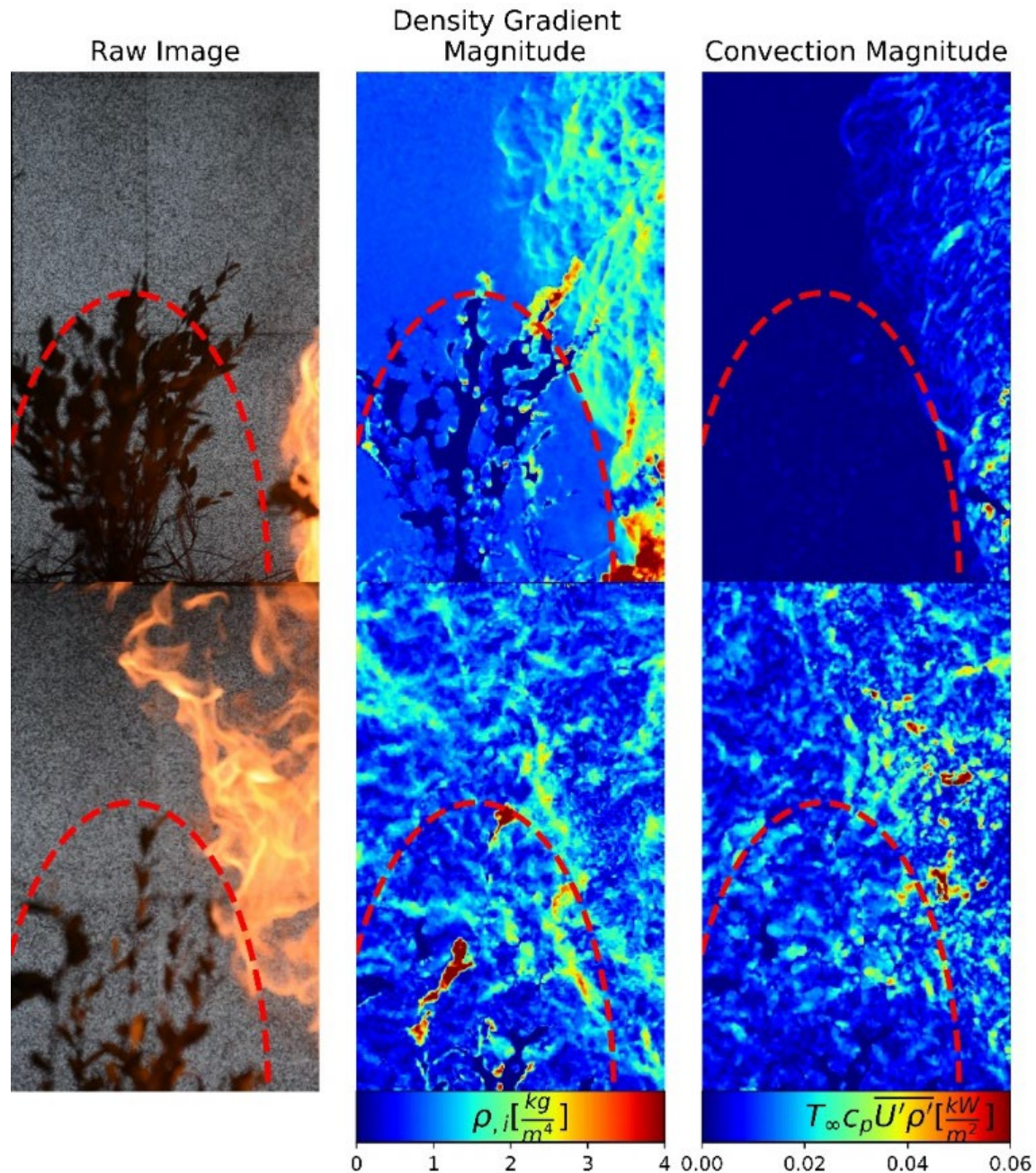


Figure 19 Visualization of the thermal plume and convective plume around the fire. The live fuel is Fetterbush (Lyonia). The first row represents the cases without the presence of external wind, and the second row shows the case was 0.8 m/s wind was present. The red dotted line shows the plant location.

From figures 17-19, it can be seen that wind pushes the thermal plume ahead of the flame. This phenomenon can be seen, especially with higher wind speed and lower ambient temperature. When no external wind is present, small changes and variation in density gradient around the plant's foliage can be seen. This phenomenon could result in processes such as preheating of the foliage and also release of pyrolysis products; both phenomena cause the density of the gases surrounding the live species to change.

1.5.5 Summary of results for all experimental configuration

In section 1.5.4, the process and results for understanding flow behavior for a single experiment was described. This procedure gave a good understanding of the flow behavior around the fire with and without the presence of external wind, and how potentially live shrubs would have affected the flow field. These findings were a great methodology for understanding the flow field. However, having around 11,600 images for each burn and around 1,125,200 total high-resolution images made it necessary to develop a data analysis paradigm. This process made it possible to develop a correlation between different experimental configurations, while it reduced the size of the dataset significantly. The first step for developing such model was to understand and describe the flow using fundamental transport equations of heat and momentum, doing so, the following Reynolds Averaged Navier-Stokes (RANS), and energy balance equation was used as the basis of the analysis

$$\bar{U}_{i,t} + \bar{U}_j \bar{U}_{i,j} = -\frac{1}{\rho} \bar{p}_{,i} + \bar{f}_i + \nu \bar{U}_{i,jj} - \overline{u_i u_{j,j}} = -\frac{1}{\rho} \bar{p}_{,i} + \bar{f}_i + (\nu + K_\nu) \bar{U}_{i,jj} \quad (47)$$

$$\bar{T}_{,t} + \bar{U}_j \bar{T}_{,j} = \alpha \bar{T}_{,jj} - \overline{T' u_{j,j}} = (\alpha + K_H) \bar{T}_{,jj} \quad (48)$$

In equation 47, \bar{U}_i is the mean velocity of the flow, ρ is the density of the fluid, p_i is the pressure gradient associated with flow field, ν is the kinematic viscosity of the fluid, u_i is the fluctuating

component of velocity and K_v is eddy diffusivity of momentum. In equation (48) \bar{T} and T' are the mean and fluctuating components of temperature of the flow field and α is the thermal diffusivity and K_H is eddy diffusivity of heat.

In fluid mechanics, the convective mode of transport of momentum, heat, and mass is described using eddy diffusivity. Therefore, to understand convective heat transfer in propagating fire in a vegetative fuel bed, eddy diffusivity was used to describe convective heat transfer. Since BOS dataset provided a measure of convective heat transfer as well, thus this dataset was used to obtain values on eddy diffusivity. Mathematically eddy diffusivity of heat is described as:

$$K_H = \frac{\overline{T'u_j}}{\bar{T}_{,j}} \quad (49)$$

In many cases is not trivial to measure fluctuating components nor the gradient terms. Moreover, knowing the values associated with eddy diffusivity, not only provides understanding of the convective mode of transport but also utilizes solving RANS equation numerically. Thus, various numerical methodologies exist for modeling eddy diffusivity. These methodologies are usually categorized based on the number of transport equations that are necessary to be solved in addition to the fundamental governing equations. For example, the commonly used $k - \epsilon$, $k - \omega$ are two equation models because they solve Turbulent Kinetic Energy TKE and dissipation or vorticity equation in addition to the governing transport equations.

When working with an experimental dataset, like the BOS dataset, solving additional transport equations is not possible. However, a category of eddy diffusivity models known as zero-equations models exists that doesn't solve any transport equation. These models instead provide an algebraic relation between the parameters that are correlated to eddy diffusivity. Looking back at the physical description of diffusion, one can describe eddy diffusivity as:

$$L \propto \sqrt{K \cdot t} \quad (50)$$

Here L is a length scale that the fluid parcel will be transported by eddy with diffusivity of K in the time scale t . Equation 50 can be rewritten as

$$K \propto \frac{L^2}{t} \quad (51)$$

Prandtl used the same methodology and defined the characteristic length L as mixing length L_m . The mixing length is defined as the distance the fluid parcel will be transported while it conserves its properties before it mixes with the surrounding fluid. Looking at the BOS results (Figure 11) this distance can be described as the horizontal width and vertical height of the thermal plume around the fire. In this study preheating of the surface fuels are important, thus in our analysis only the horizontal width was considered. Figure 20 shows a schematic of mixing length around a fire with and without presence of wind.

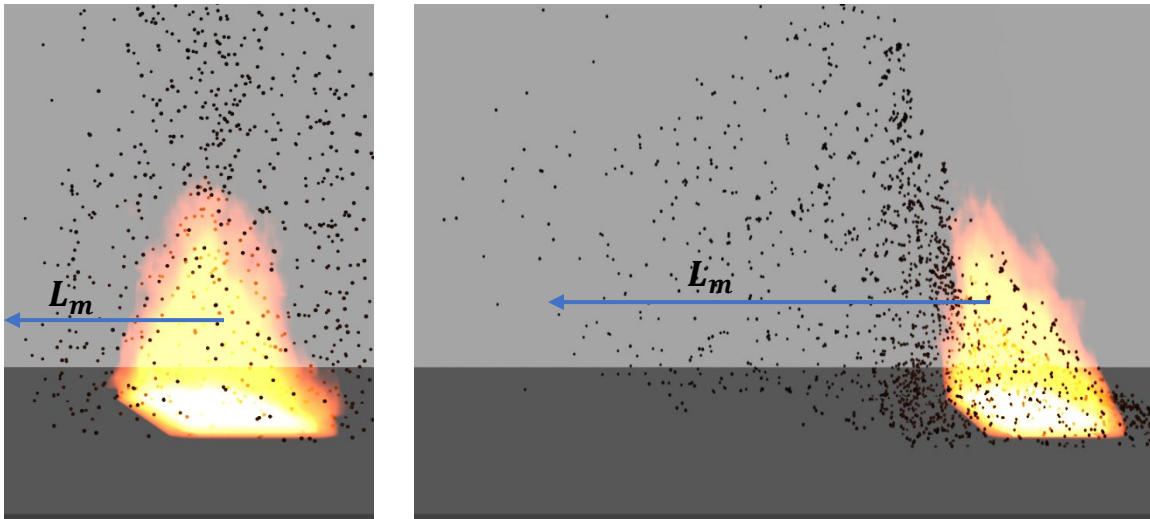


Figure 20 Schematic of the definition for convective mixing length

Looking back to equation (51), other than length scale L , eddy diffusivity is also dependent on a time scale t . To define this time scale, the vorticity which characterizes the rotation of eddies was

considered. These eddies facilitate the turbulent mixing thus a time scale corresponding to vorticity can help to characterize eddy diffusivity. The vorticity equation is obtain by taking curl of the Navier-Stokes equation :

$$\frac{D\omega}{Dt} = \underbrace{\omega_j u_{i,j}}_1 - \underbrace{\omega_i u_{j,j}}_2 - \underbrace{\nu \omega_{i,jj}}_3 + \underbrace{\frac{1}{\rho^2} \epsilon_{ijk} \rho_{,i} P_{,k}}_4 \quad (52)$$

Here ω is the vorticity vector. The first term represent vortex stretching, the second term is related to fluid expansion due to combustion, the third term is viscous diffusion of vorticity. The fourth term, is the *baroclinic torque*, which is quite important in turbulent combustion. Baroclinic vorticity arises when the density and pressure gradients are misaligned. In the flame, the pressure gradient is hydrostatic and the density gradient points horizontally outward, which causes the baroclinic term to be nonzero. Since the only term in the vorticity equation that is not a function of existing vorticity is the baroclinic term, it is theorized baroclinicity gives rise to the initial vorticity in the flame[68]. One can rewrite baroclinic term as:

$$B = \frac{\rho_{,i}}{\rho} \cdot g \quad (53)$$

Looking back at equations (6) , BOS can be used to calculate the value for density gradient $\rho_{,i}$.

The calculated value B can be combined with L_m to define eddy diffusivity as :

$$K = L_m^2 \cdot B^{0.5} \quad (54)$$

$$K = L_m^2 \cdot \sqrt{(g \cdot \rho_{,i} / \rho)} \quad (55)$$

This model can be used to summarize the turbulent nature of the convective flow around the flame. Having this model, it was necessary to process all 1,125,200 images to create a new dataset, which the model could be deployed to. To create such database the values of the density gradient,

convective heat flux and velocity magnitude was averaged over two regions of each individual image. The first region was the entire frame of image. This region, as will be described in the next section, was used to calculate the values for mixing length L_m . The second region was a neighborhood with dimensions of 100x100 pixels on the bottom right corner of image figure 21. The purpose of this region, as it is demonstrated as a white box in figure 21, was to capture the convective heat flux above the fuel bed. The values calculated using the second region provided understanding on the convective heat flux ahead of the flame which caused preheating of the unburnt fuel.

Sample processed data
with region of interest

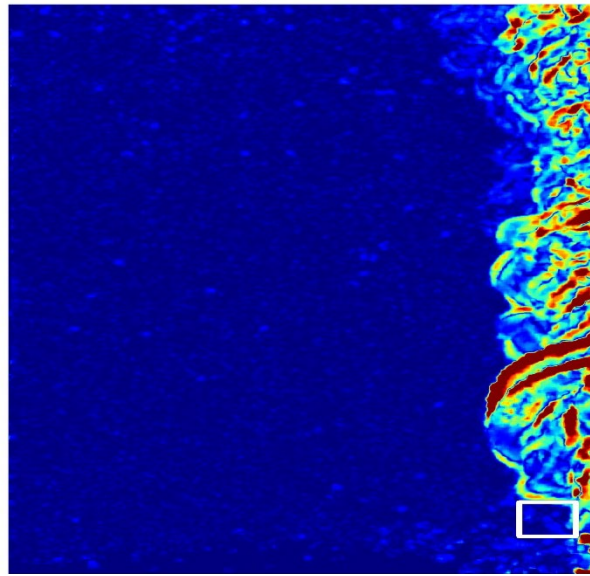


Figure 21 Demonstration of region of interest when processing convection.

1.5.5.A Calculation process of mixing length L_m and time scale t

In the previous section, a model was developed to help characterize turbulent behavior of convective thermal plume around the flame, thus eddy diffusivity was defined based on a mixing time scale and mixing length scale. Afterward, the BOS dataset was processed to average

convective heat flux over the entire frame of an image. For simplicity the mean heat flux value is shown as $\langle H \rangle$. To define the convective mixing length a normalized value R_H was defined as

$$R_H = \frac{\langle H \rangle - \langle H \rangle_{min}}{\langle H \rangle_{max} - \langle H \rangle_{min}} \quad (56)$$

The subscript *min* and *max*, demonstrates the maximum value of the corresponding signal. Later the R_H signal was plotted against a fuel bed length scale $X = L \cdot t / \Delta t$. Here t is the sampling time, and Δt is the experiment duration, and L is the length of the fuel bed. After plotting R_H , a normal distribution function defined in equation 57 was fitted to the dataset.

$$G = e^{-0.5 \left(\frac{x - \mu}{\sigma} \right)^2} \quad 57$$

Here μ is the mean of signal distribution and σ is the standard deviation. doing so, L_m was defined as

$$L_m = 3 \cdot \sigma \quad 58$$

This value of L_m corresponds to the distance from the maximum to the location where R_H reaches 0.003 of its initial value. Looking back to Prandtl's definition of mixing length, this value corresponds to the length that the fluid is mixed with its surrounding. Figure 22 shows the plotted value R_H and how L_m was calculated.

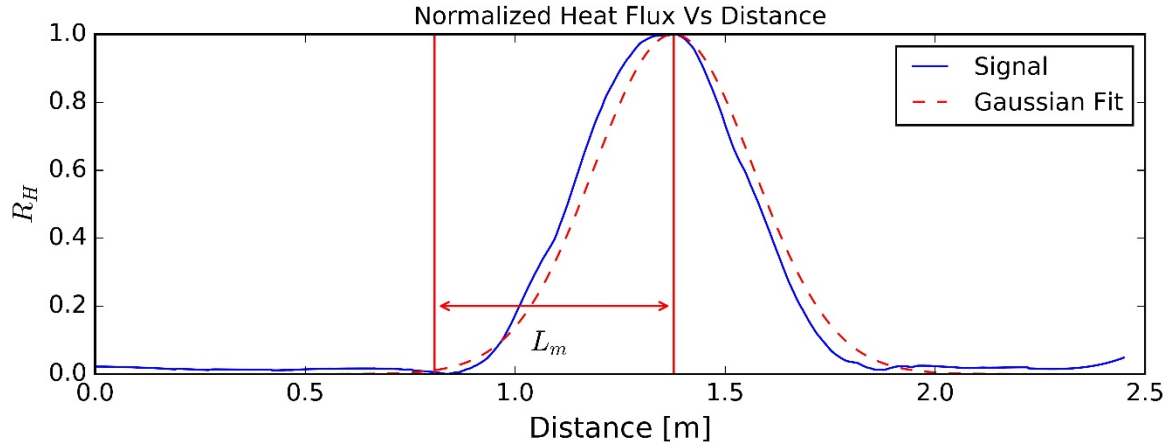
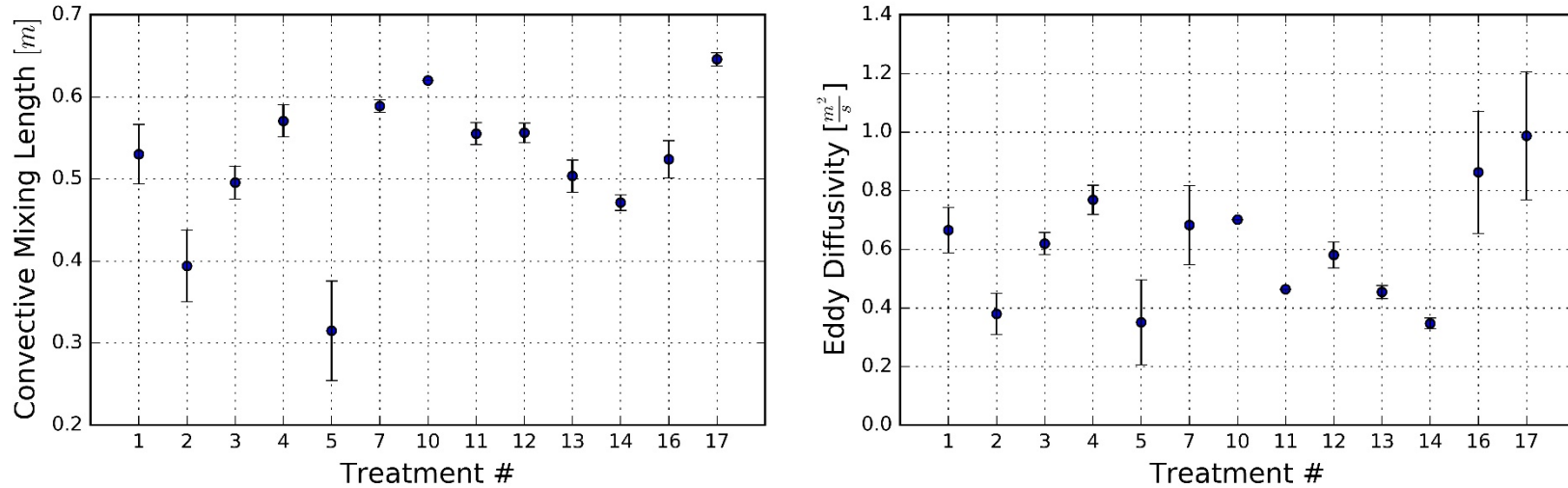


Figure 22 plot of R_H vs Distance

After calculating L_m for each experiment, t was calculated using the magnitude of the density gradient signal at the position of L_m . Doing so made it possible to calculate eddy diffusivity for each experimental setup. The summarized results for each phase of the experiments are demonstrated below in figures 23-25

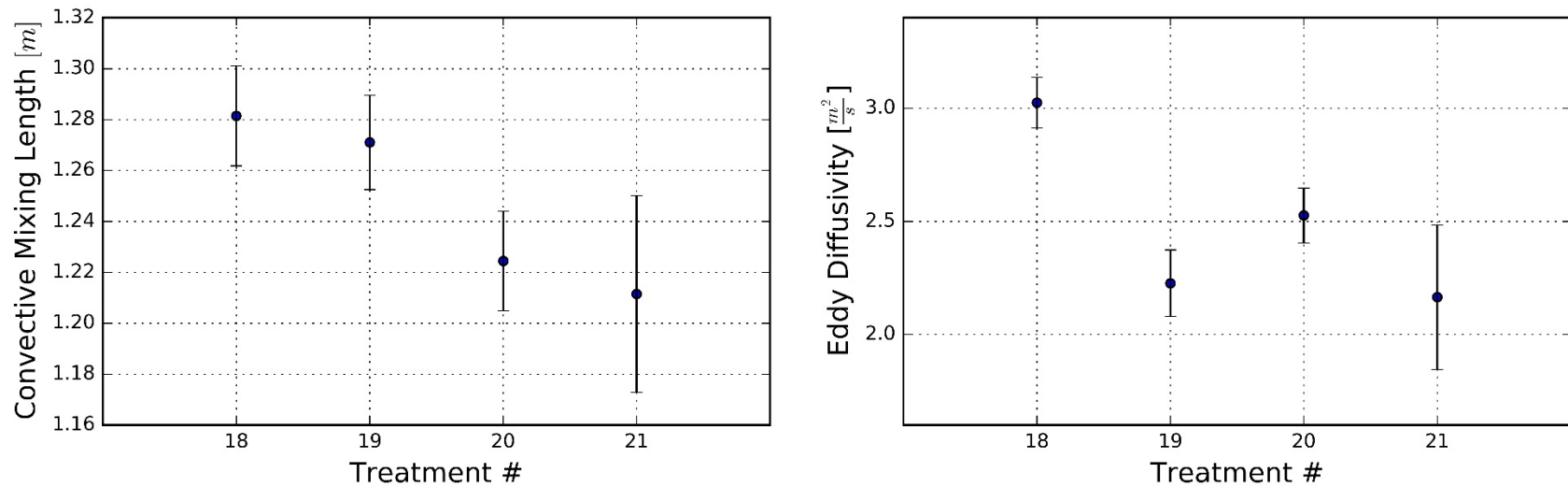
Convective Mixing Length and Eddy Diffusivity Calculation for Phase 1



Treatment#	Mass Longleaf Pine (g)	Live Plant	Number of Live Plant	Wind speed (m/s)	Ambient Temperature (C)	Ambient Relative Humidity	Longleaf pine fuel moisture (%)	Foliage fuel moisture (%)
1	800	Pine only	0	0.0	22.18	55.67	13.98	0.0
2	800	Inkberry	24	0.0	21.45	53.0	9.17	115.7
3	800	Inkberry	41	0.0	20.08	58.5	10.52	122.47
4	1000	Fetterbush	21-31	0.0	23.65	41.5	9.11	96.24
5	1000	Darrow's blueberry	46	0.0	26.67	33.0	9.53	124.06
7	1000	Blueberry+Fetterbush	31	0.0	20.9	31.0	11.16	132.79
10	1000	Pine only	0	0.44	21.45	31.0	9.51	0.0
11	1000	Inkberry	24	0.44	23.38	27.5	9.54	113.11
12	1000	Inkberry	41	0.44	23.65	30.5	9.28	113.65
13	1000	Inkberry	24	0.0	23.93	36.25	11.03	113.33
14	1000	Inkberry	41	0.0	24.34	33.5	10.59	112.3
16	1000	Inkberry	34-46	0.0	24.75	33.0	9.25	114.71
17	1000	Inkberry	34	0.44	23.1	38.0	10.39	107.15

Figure 23 Convective mixing length and eddy diffusivity calculation for phase 1

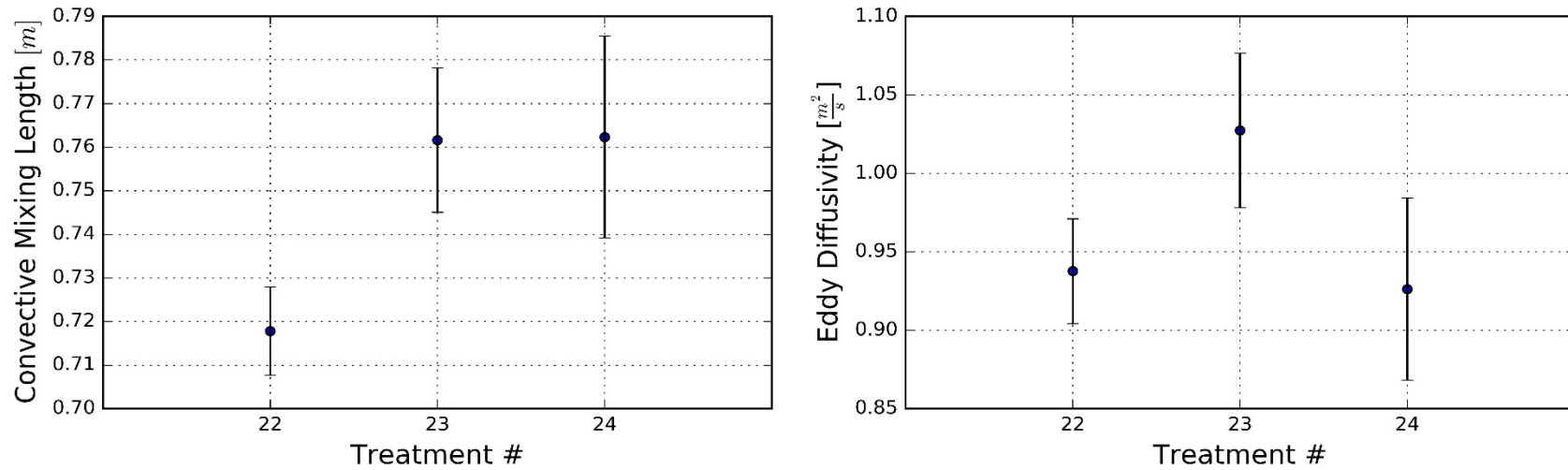
Convective Mixing Length and Eddy Diffusivity Calculation for Phase 2



Treatment#	Mass Longleaf Pine (g)	Live Plant	Number of Live Plant	Wind speed (m/s)	Ambient Temperature (C)	Ambient Relative Humidity	Longleaf pine fuel moisture (%)	Foliage fuel moisture (%)
18	1000	Fetterbush	50	0.8	6.47	59.19	10.45	101.46
19	1000	Darrow's blueberry	54	0.8	6.52	62.36	11.53	138.85
20	1000	Blueberry+Fetterbush	54	0.8	7.26	58.29	10.61	115.46
21	1000	Pine only	0	0.8	8.73	65.2	10.32	0.0

Figure 24 Convective mixing length and eddy diffusivity calculation for phase 2

Convective Mixing Length and Eddy Diffusivity Calculation for Phase 3



Treatment#	Mass Longleaf Pine (g)	Live Plant	Number of Live Plant	Wind speed (m/s)	Ambient Temperature (C)	Ambient Relative Humidity	Longleaf pine fuel moisture (%)	Foliage fuel moisture (%)
22	1000	Sparkle Berry	74	0.44	28.25	17.71	7.83	105.46
23	1000	Fetterbush	74	0.44	26.11	23.33	8.0	104.27
24	1000	Inkberry	74	0.44	26.24	26.4	8.85	90.55

Figure 25 Convective mixing length and eddy Diffusitivity calculation for phase 3

The result demonstrated in figures 23-25 elaborate the effect of the external wind as a key parameter affecting the mixing length, eddy diffusivity and thus convective heat transfer. In the first phase, there was a big variety of treatments and experimental configurations, however comparison of treatment 12 and 14 shows that when all the parameters were kept constant, the external wind increased the convective mixing length and thus eddy diffusivity. The results obtained using BOS in this phase did not demonstrate how adding live shrubs had affected the eddy diffusivity compared to cases with only pine needle fuel bed. The small shrub height, and the variability on other important parameters such as the number of plants and mass of pine needle fuel bed may have caused such outcome. However, generally the result of all three phases indicate that the presence of the plants affected the calculated eddy diffusivity.

1.5.5.B Calculation of convective heat flux for all experimental configuration

As it was explained in the previous section, a neighborhood of 100 x 100 pixels were selected to capture convective heat flux caused by the flame. Figure 26 shows a sample signal obtained by such process. The results for all the experiments were summarized by evaluating the maximum value and median value of the convective signal distribution. The results are shown in figure 27. The description for each treatment is shown in figures 23-25 and tables 3-5

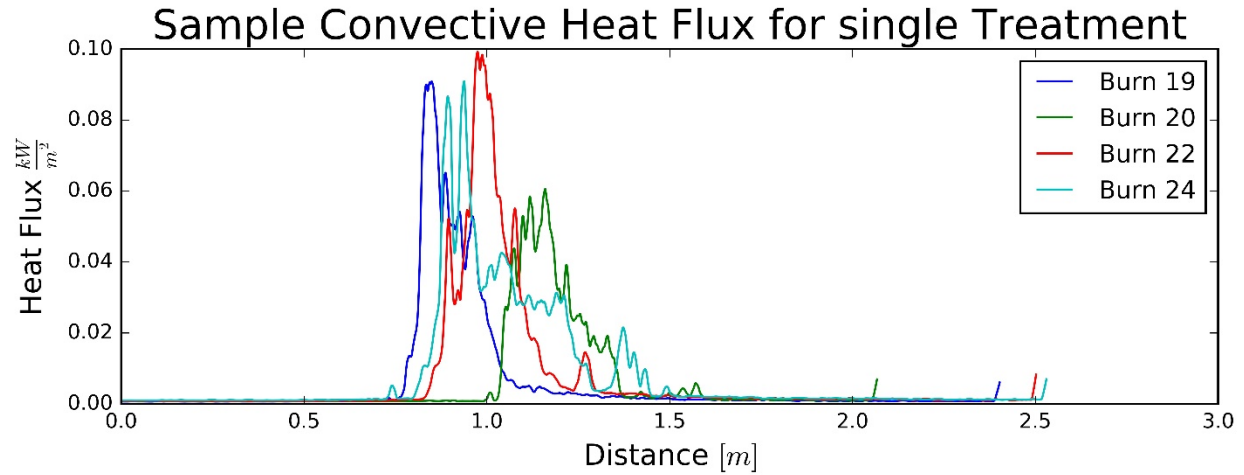


Figure 26 Convective heat flux for a single treatment

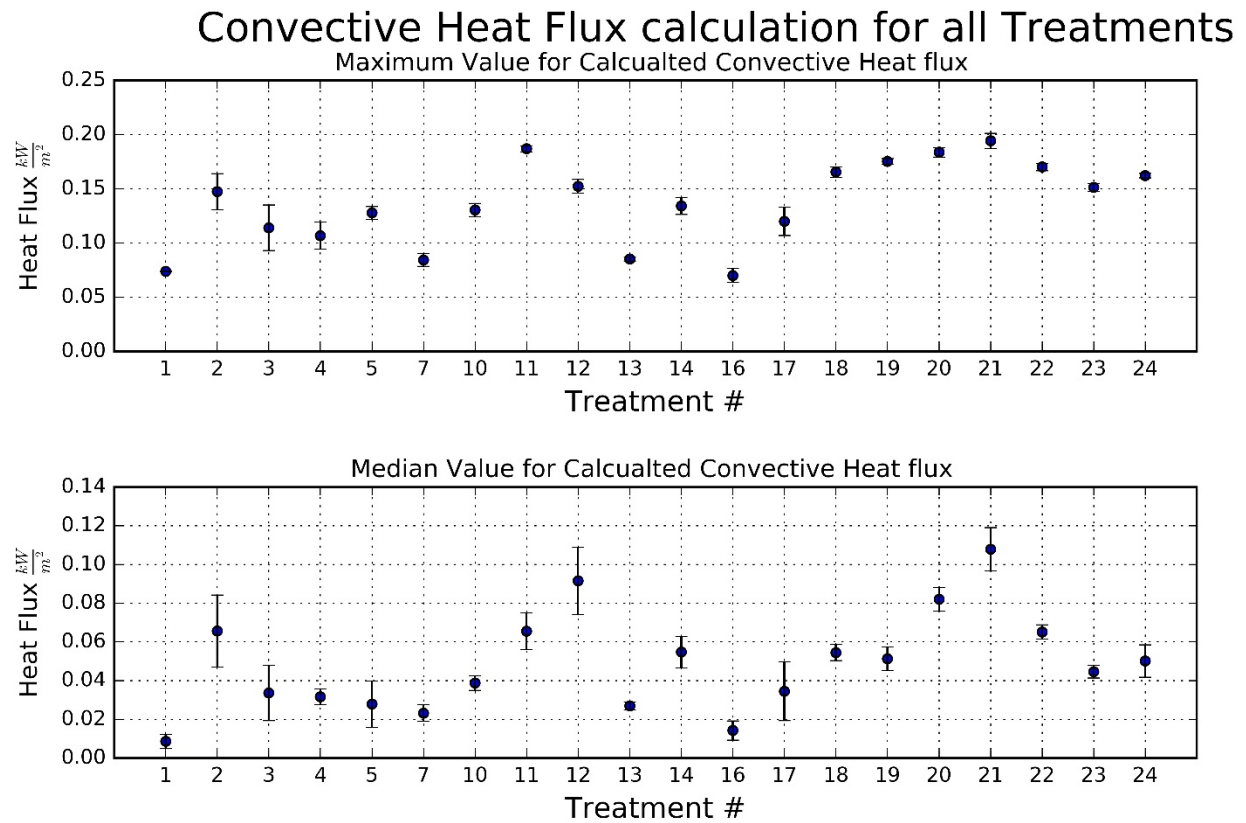


Figure 27 Maximum and the median value of convective heat flux for all treatments

The results are shown in figure 27 shows how the convective heat flux changed in different experimental configurations. It has to be noted, as it was also discussed in section 1.5.4, these

values are an estimation of the amount of convective heat transfer caused by the fire in the direction that it propagates. As it has also been discussed various assumptions were made to estimate convective heat flux, and these assumptions may cause uncertainty in the results shown in figure 27. One of the major assumptions was using 2D BOS to study a 3D phenomenon, consequently the images and data were a planar projection of a 3D phenomenon. All the values obtained assumed that when a linear flame was present, all the properties did not change in the direction of line of sight. As flame front deviates from linear this assumption could cause uncertainty on the quantitative results. Thus, the computed values may not be exact. However, this methodology still can provide a general understanding of the convective heat transfer for example, as demonstrated here, how it changes in different wind condition.

1.6 Mass Loss Data Analysis

In section 1.3.1 the importance of high-resolution mass loss measurement of a single plant was discussed. It had been discussed that a decent mass loss data could be combined with gas measurement data and correlate the pyrolysis gases to the mass lost in the pyrolysis process. The mass-loss rate can also help to understand heat transfer effects on the pyrolysis process. To create such signal a high precision scale was used. The main challenge in obtaining signal was that in many of the experiments, especially when no wind was present, the ashes from the burnt fuel would fall on to the mass loss test section and corrupt the signal obtained by the sensor. As it can be seen in figure 29 the total mass loss of a plant was less than 7 grams, thus the interference caused by the ashes made the data for specific burn useless. Other than these signal interferences, in some of the experimental setup the plant was elevated and therefore couldn't be placed on the scale. Nevertheless, in some cases, the signal gathering was successful. These signals follow a similar trend as the signal shown in figure 28. The major differences are the initial mass of the plants and also mass loss rate, which is depended on heat transferred to the plant. Figure 28 shows a sample signal obtained by the mass loss measurement system along with the calculated mass loss rate from the signal

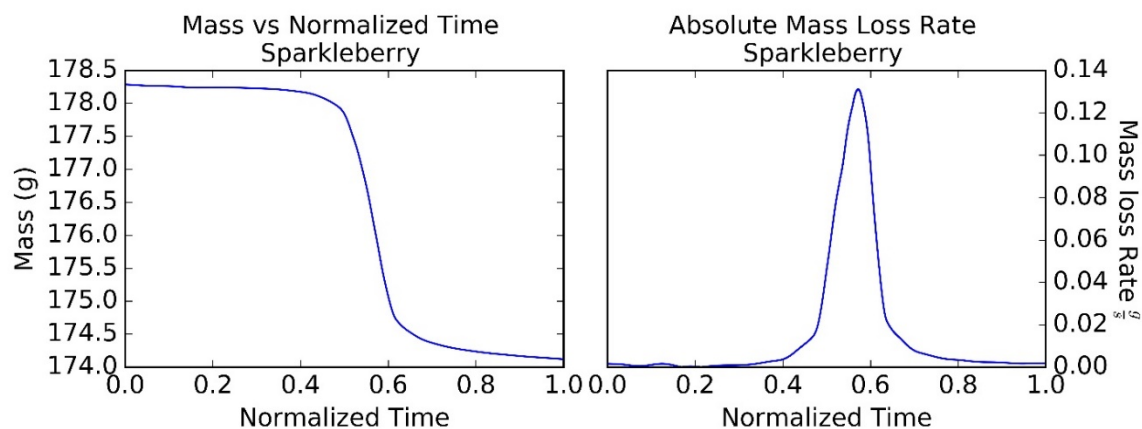


Figure 28 sample mass loss signal

In order to summarize the mass loss rate results, the initial mass of all the measured experiments, total mass loss, and the maximum mass loss rate of reliable signals was plotted in figure 29

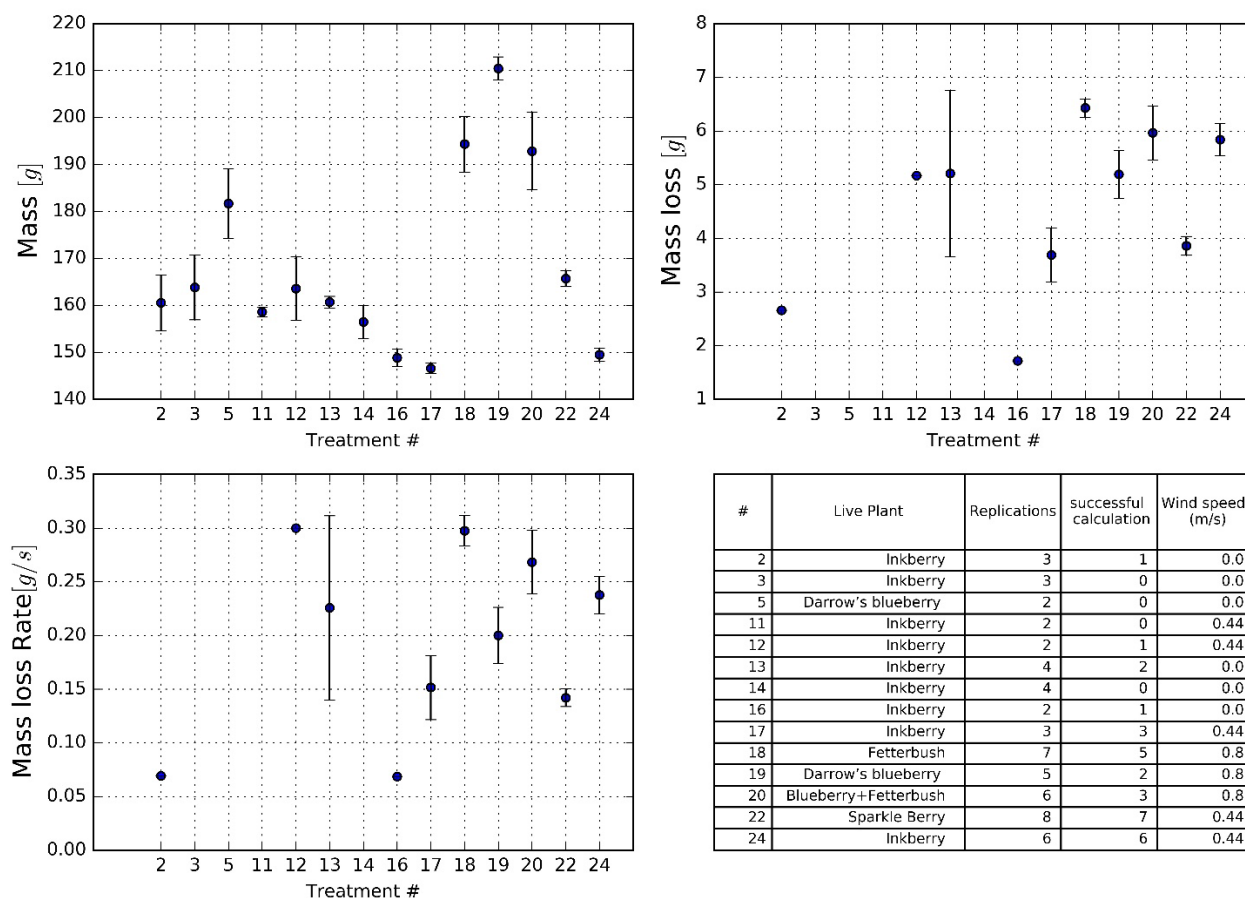


Figure 29 summary of mass loss data

1.7 Schmidt Boelter and thermocouple system Data analysis

In addition to the BOS system and high precision scale, a pair of Medtherm Schmidt Boelter sensors and a thermocouples system was installed in the wind tunnel. In the first two phases, the thermocouple was designed to mimic the temperature profiles around a plant. The temperature profiles and the maximum values did not change significantly between the experimental configurations. Figure 30 shows a sample result of the thermocouple signal in these phases. In the third phase, as mentioned in section 1.3.3 the thermocouples were dispersed in the wind tunnel to help to know the temperature when the pyrolysis gas was captured. Figure 31 shows the result for this configuration.

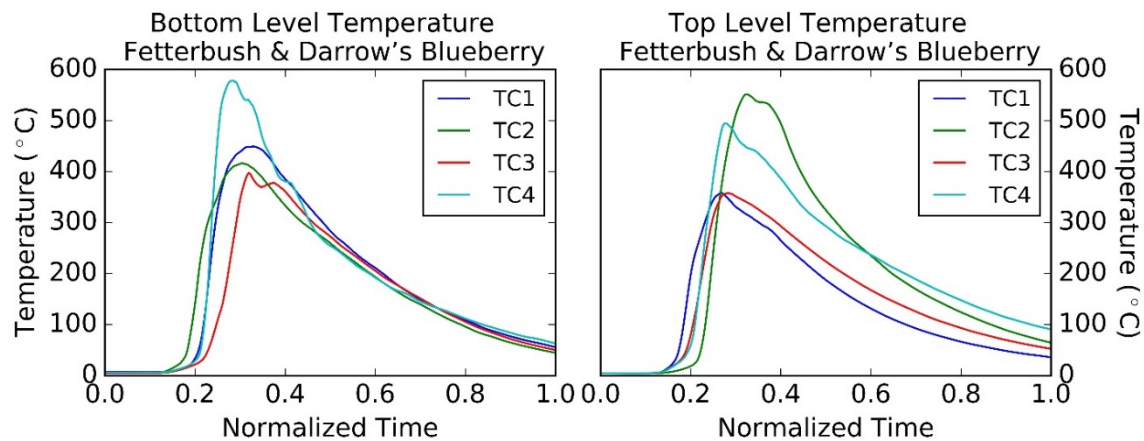


Figure 30 Sample temperature profile for two first phases

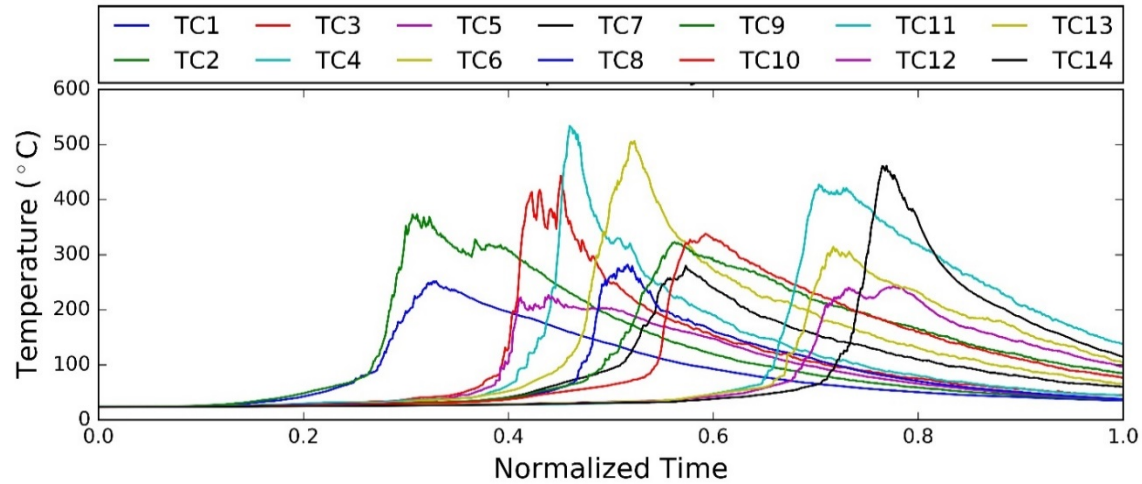


Figure 31 Sample temperature profile for third phase

The Medtherm sensor was installed to capture total and radiant heat flux absorbed by the surface fuel as the fire propagated through the fuel bed. The sample results for output of these sensors can be seen in figure 32. When looking into the heat flux sensor data, it can be seen that the amount of radiation and total heat flux varies a lot. The reason for this difference relates back to the position of the sensors. The sensors were laid out so it can capture heat flux on the surface of the fuel bed, but commonly it would have been covered by the pine needle. As a result, the total heat flux measurement took into account conduction and also limited the view factor between the radiometer and the flame, which resulted in a small amount of radiation to be recorded.

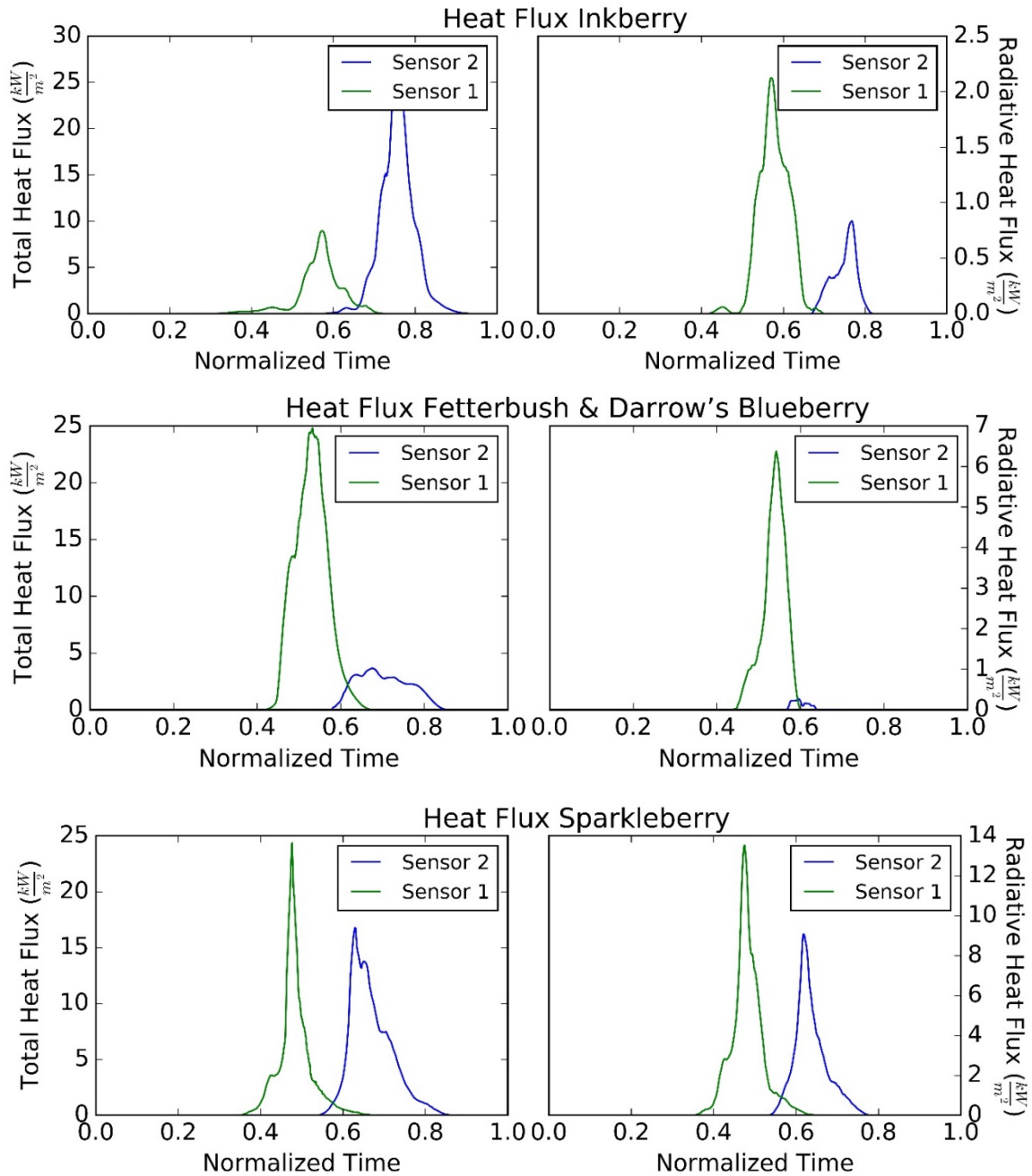


Figure 32 Sample signal of heat flux sensors

1.8 Summary

Recent findings elaborate on the importance of convective heat transfer in fire propagation in vegetative fuels. In this research, the effect of convective heat transfer mechanism on the pyrolysis

process and fire propagation was studied. To quantify convection ahead of the flame, Background Oriented Schlieren (BOS) was used as a simple method of flow visualization around the fire. BOS made it possible to visualize the thermal plume associated with the fire as the flame propagated through the fuel bed. This enabled us to effortlessly see how in a wind-driven fire, the wind forces the thermal plume ahead of the flame while in the non-wind driven fire the thermal plume is attached to the flame itself. Next, we demonstrated that by applying Density Gradient Image Velocimetry (DGIV) to the result of BOS the flow associated with the thermal plume could be visualized as well. Finally, it was shown that comparing consecutive frame of images makes it possible to visualize and quantify convective heat transfer.

After visualizing convective heat around a fire, a procedure was developed to model convective heat transfer ahead of the fire using the concept of eddy diffusivity. The eddy diffusivity was defined using an algebraic equation, which used turbulent mixing length and mixing time scale. The result of evaluating eddy diffusivity in different experimental configuration, demonstrated how the presence of external wind affected the mixing length and thus eddy diffusivity. To summarize external wind effects on eddy diffusivity, the eddy diffusivity was plotted against non-dimensional Froud number defined as :

$$Fr^2 = \frac{(U_w - ROS)^2}{g \cdot \frac{\Delta H_c}{H_\infty} \cdot W_f} \quad (59)$$

This Froud number expression provides a measure of the ratio of the kinetic energy of the air over the sensible heat flux provided by the fire. Here, U_w is the wind speed, ROS is the rate of spread of the fire, g is the gravity and W_f is the width of flame. The convective buoyancy is expressed as $\Delta H_c / H_\infty$, where ΔH_c is enthalpy of combustion and H_∞ is the ambient enthalpy. Froud number shown in equation (59) is very similar to the Froud number defined by Clark et al [69]. In this

study for calculating the heat of combustion, ΔH_c , the heat release of the long leaf pine needle was only considered. Figure 33 shows the plotted values of eddy diffusivity against their calculated Froude number

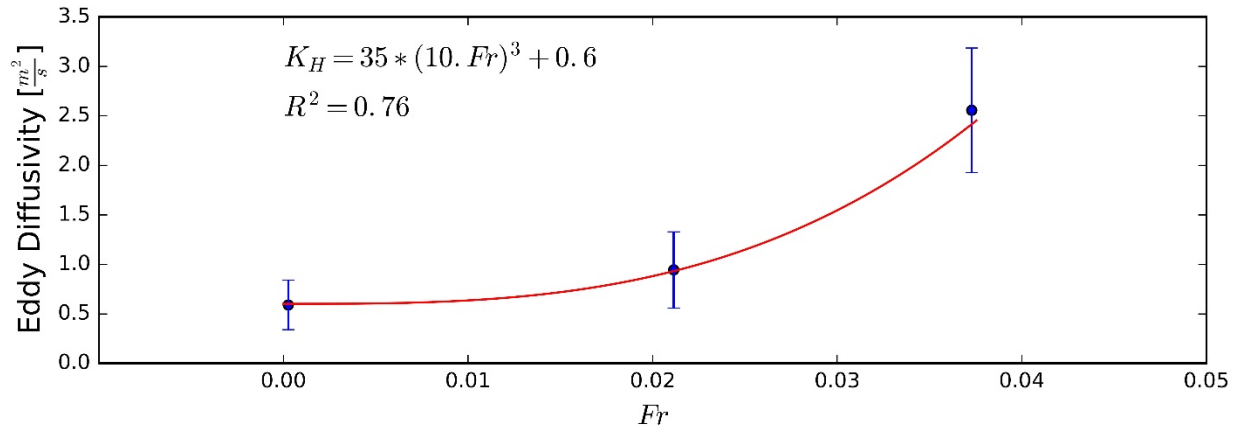


Figure 33 Values of eddy diffusivity against calculated Froude number

As it can be seen in figure 33, eddy diffusivity can be described as the function of Froude number as:

$$K_H = 35 \cdot (10 \cdot Fr)^3 + 0.6 \quad 60$$

The same procedure can be taken to evaluate the effect defined Froude number on the value of convective heat flux measured ahead of the flame using BOS. Figure 34 shows the result of such process.

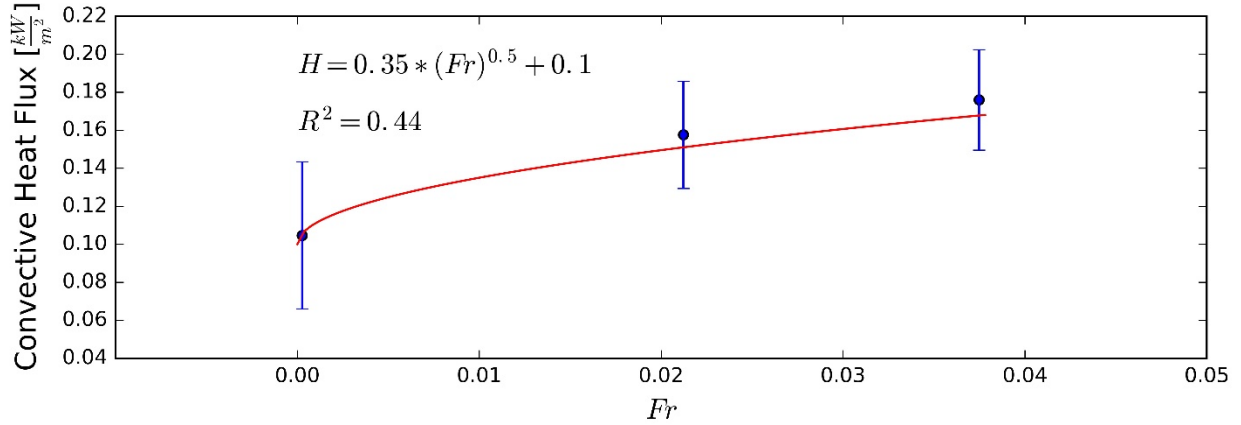


Figure 34 Values of convective heat transfer against calculated Froude number

Similarly, an expression can be defined which correlated the convective heat flux obtained in these experiments to the Froude number

$$H_c = 0.35 \cdot Fr^{0.5} + 0.1 \quad (61)$$

In calculating convective heat flux, it was assumed when a linear flame is present, all the properties do not change in the direction of line of sight, As flame front deviates from linear this assumption could cause uncertainty on the quantitative results. Thus, the computed values may not be exact. However, when looking at the order of magnitude of measured values it is comparable to some numerical models such as the one done by Porterie et al , [70]. Nevertheless, this methodology still can provide a general understanding of the convective heat transfer for example, as demonstrated here, how it changes in different wind condition.

2 Numerical Modeling of Fire Spread Across Pine Needles Fuel Beds

2.1 Introduction

Wildland fires are a big threat to human life and the local ecosystem. In 2018, more than 58,000 fires occurred in the US and those fires burned over 8,000,000 acres [71]. One of the plants that are mostly prone to fire is dead plant which is widely distributed in the forest. Due to the low moisture content (generally 0-40%), the characteristics of easy accumulation of heat and the concentrated distribution, the dead fuel has an extremely high probability of fire and will bound to spread once a fire occurs. Hence, better understanding of the fire spread characteristics of such fuels are essential to control large scale wildland fires.

The propagation of fire is a complex phenomenon involving ignition, pyrolysis, combustion and spread. Each process is also affected by many factors: thermal properties of the ignited materials, heat transfer and external environment conditions [72]. The external environment is considered as the most important aspect that affects the fire size and spread rate. It mainly includes terrain slope and wind conditions. Basically, the air flow caused by the wind environment can provide enough oxygen during combustion. It can also increase the heat transfer to the unburned fuel area by reducing the angle between the flame and unburned fuel bed. Therefore, the wind speed will inevitably accelerate the fire spread.

In order to better understand the fire spread phenomenon, many fire spread models were established. Wildland fire spread models are mainly divided into three categories: statistical models, semi-empirical models and physical models. In contrast to the statistical models and semi-empirical models, physical models pay more attention to the mechanism of chemical process and heat transfer [73]. The solid-phase pyrolysis and the gas-phase combustion are introduced in chemical mechanisms, and the kinetic parameters are used to support each reaction. The heat

transfer process involves radiation, conduction and convection. Most of the thermal degradation models of wildland fire is based on a simplified reaction mechanism. The first step is to turn the relative wet plants into dry plants, which can be described as water evaporation. The second step is a single-step reaction, which mainly pyrolyzes dry plants into char and fuel gases. Both of the above two step reactions are endothermic process. The third reaction is gas combustion reaction. The real plants contain many compositions, and each of them has various physical properties. Therefore, more complex physical models are needed to improve the reliability of the results. This study utilizes a series of Computational Fluid Dynamics simulations to study the fire spread across pine needles fuel beds. Three different wind conditions including $U=0$, 0.44, and 1 m/s are investigated. Two modeling schemes, single-step reaction and multi-step reaction are utilized to model the pyrolysis process. In the single-step reaction, the pine needles fuel is considered as cellulose, while for the multi-step reaction the pine needles fuel is modeled as a combination of cellulose, hemicellulose and lignin. To validate the numerical methodology, the temperature and flame spread rate are compared with the wind tunnel measurements. Different quantities such as temperature at fuel bed surface, flame shape, flame spread rate, flame width and fuel mass loss rate are analyzed in this study.

2.2 Experimental setup

The experiments were conducted in a wind tunnel located at the U.S. Forest Service PSW Research Station in Riverside, CA. Figure 35 shows a schematic of the experimental setup. The length, width and height of wind tunnel is 4.0 m, 1.2 m and 1.0 m, respectively. For ease of observation, two transparent glasses are installed on the both side of the tunnel. A fan located on the left side of the tunnel is used to create a wind environment, and a rectifying section is arranged at the beginning of the tunnel to obtain uniform wind profile in the cross-section. The bottom of the tunnel is made

of gypsum. The ambient temperature and humidity were maintained at 24 °C and 24%, respectively. The experiments repeated for three different wind conditions. Table 1. lists the details of each experiment. For each experiment, the total mass of the pine needles is 1 kg and the fuel moisture content is 10%. The fuel size is 2.8 m length, 0.9 m width and 0.06 m height. Several thermocouples are arranged at the surface of the fuel bed to collect the flame temperature.

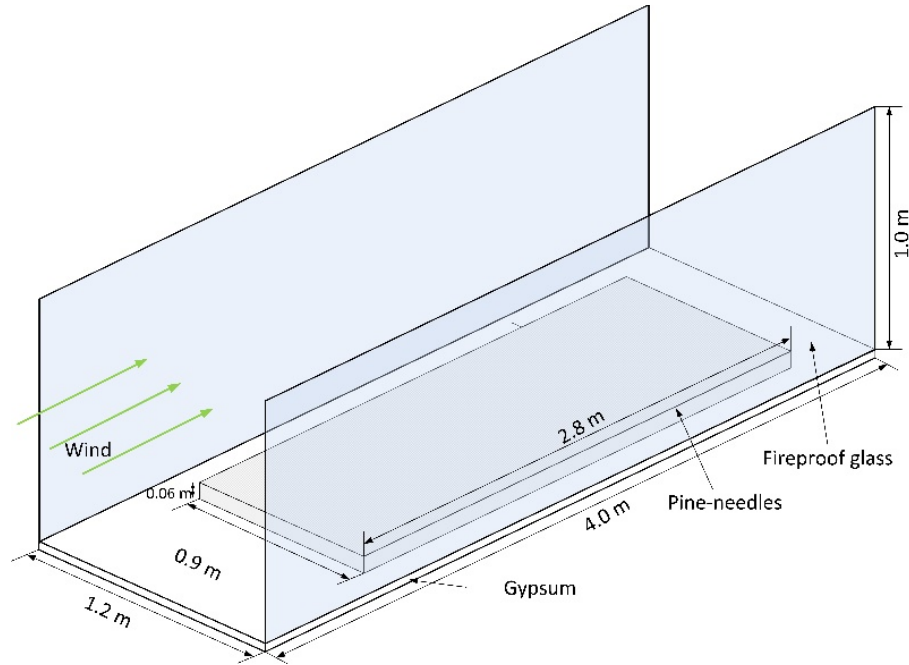


Figure 35. A schematic of wind tunnel with fuel bed dimensions

Table 6. Different experimental scenarios

Case no.	Total mass (kg)	Fuel Content (%)	Moisture	Wind speed (m/s)
1	1	10		0
2	1	10		0.44
3	1	10		1

2.3 Numerical model

2.3.1 Gas-phase equations

Large eddy simulation (LES) technique is utilized to study pyrolysis and combustion of pine needles fuel bed. The LES equations are derived by implementing a low-pass filter, parameterized by a width of Δ , to the mass, momentum, energy and species equations. The Favre-filtered governing equations are presented as follows [74]:

$$\frac{\partial \bar{\rho}}{\partial t} + \nabla \cdot (\bar{\rho} \tilde{u}) = 0 \quad (62)$$

$$\frac{\partial \bar{\rho} \tilde{u}}{\partial t} + \nabla \cdot (\bar{\rho} \tilde{u} \tilde{u}) = -\nabla \bar{p} - \nabla \cdot (\bar{\tau} + \tau^{sgs}) + \bar{\rho} g \quad (63)$$

$$\frac{\partial \bar{\rho} \tilde{h}}{\partial t} + \nabla \cdot (\bar{\rho} \tilde{h} \tilde{u}) = \frac{D\bar{P}}{Dt} + q''' + q^{sgs} - \nabla \cdot (\bar{q}_c + \bar{q}_d + \bar{q}_r) \quad (64)$$

$$\frac{\partial \bar{\rho} \tilde{Z}_\alpha}{\partial t} + \nabla \cdot (\bar{\rho} \tilde{u} \tilde{Z}_\alpha) = -\nabla \cdot (\bar{J}_\alpha + J_\alpha^{sgs}) + \bar{m}_\alpha''' \quad (65)$$

where $\bar{\rho}$ is the filtered density, \tilde{u} is the Favre-filtered velocity vector, \tilde{Z}_α is the mass fraction of lumped species α , \bar{J}_α and J_α^{sgs} denote the molecular species diffusion flux and subgrid-scale (SGS) species diffusion flux, respectively, \bar{m}_α''' is the mean chemical source term, \bar{p} is the background pressure, $\bar{\tau}$ and τ^{sgs} represent viscous and SGS stress tensors, \tilde{h} is the sensible enthalpy, Δ is the filter width, \bar{P} is the filtered pressure, q''' is the heat release rate per unit volume from chemical reaction, q^{sgs} is the energy transferred to subgrid-scale, \bar{q}_c , \bar{q}_d and \bar{q}_r represent the conductive, diffusive and radiative heat flux.

Turbulence model was mainly described based on the two turbulent transport coefficients: the turbulent viscosity and the turbulent diffusivity. Schmidt number and Prandtl number were used to identify the turbulent diffusivity, and both of them are given a value of 0.5 [75]. In this study, the eddy viscosity was calculated based on the Deardorff's model [76, 77]:

$$\nu_t = C_v \Delta (k_{sgs})^{1/2} \quad (66)$$

$$k_{sgs} = \frac{1}{2} ((\bar{u} - \hat{u})^2 + (\bar{v} - \hat{v})^2 + (\bar{w} - \hat{w})^2) \quad (67)$$

Where ν_t is the turbulent viscosity, C_v is a constant, 0.1, \bar{u} represent the average value at the grid cell center, \hat{u} is the weighted average over the adjacent cells.

All the formulation relating different flux (heat, species, momentum) and source terms are presented as follows:

$$(J_\alpha + J_\alpha^{sgs}) = -\bar{\rho}(\tilde{D}_\alpha + \frac{\nu_t}{Sc_t}) \nabla \tilde{Z}_\alpha \quad (68)$$

$$\bar{\tau} = -2\tilde{u}(\frac{\pi}{\Delta}(\frac{\tilde{k}_{sgs}}{2})^{1/2} - \frac{1}{3}(\nabla \cdot \tilde{u}) I) \quad (69)$$

$$\bar{\tau}^{sgs,d} = -2\bar{\rho}\tilde{\nu}_t(\frac{\pi}{\Delta}(\frac{\tilde{k}_{sgs}}{2})^{1/2} - \frac{1}{3}(\nabla \cdot \tilde{u}) I) \quad (70)$$

$$\bar{m}_F''' = -\bar{\rho} \frac{\min(\tilde{Z}_F, \tilde{Z}_A/s)}{\tau_{min}} \quad (71)$$

$$q^{sgs} = -\bar{\rho}\bar{c}_p \frac{\nu_t}{Pr_t} \nabla \tilde{T} \quad (72)$$

$$\bar{q}_d = -\sum_\alpha \bar{\rho} D_\alpha \tilde{h}_\alpha \nabla \tilde{Z}_\alpha \quad (73)$$

Where D_α is the diffusivity of species α , Sc_t is the turbulent Schmidt number, Pr_t is the Prandtl number, \tilde{Z}_F and \tilde{Z}_A represent mass fraction of fuel gas and air, respectively, s is the mass stoichiometric coefficient for air, τ_{min} is a time scale for mixing.

2.3.2 Heat transfer

The heat release rate per unit volume is defined by the gas fuel mass production rates multiplies by the respective heat of formation:

$$q''' = -\sum_{\alpha} \dot{m}''' \Delta h_{f,\alpha} \quad (74)$$

Where q''' is the heat release rate per unit volume and $\Delta h_{f,\alpha}$ is the heat of combustion.

Due to the neglecting the heat transfer through conduction, the heat transfer process that supports fire spread mainly includes radiation and convection. The net contribution from thermal radiation is defined by:

$$\bar{q}_r = \kappa(x) [U(x) - 4\pi I_b(x)] \quad (75-a)$$

$$U(x) = \int_{4\pi} I(x, s') ds' \quad (75-b)$$

$$s \cdot \nabla I(x, s) = \kappa(x) [I_b(x) - I(x, s)] \quad (76-a)$$

$$I_b = \sigma T^4 / \pi \quad (76-b)$$

Where $\kappa(x)$ is the absorption coefficient, $I_b(x)$ is the source term, and $I(x, s)$ is the solution of the radiation transport equation for a non-scattering gray gas.

In the LES calculations, the convective heat transfer coefficient, h , is based on the combination of natural and forced convective heat transfers. More details information can be found in [75].

2.3.3 Solid-phase equation

Each solid material of fuel undergoes multiple pyrolysis reactions before it burns. In this process, many intermediate products will be formed to support the next reaction. For a given reaction (dry pyrolysis and oxidation), the reaction rate is defined by Arrhenius rate equation:

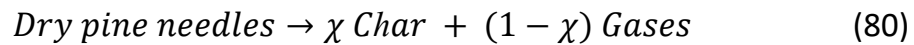
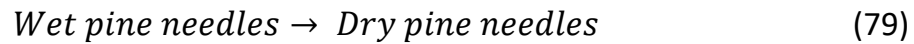
$$\frac{dY_{s,i}}{dt} = -\sum_{j=1}^{N_{r,i}} r_{ij} + \sum_{i'=1}^{N_m} \sum_{j=1}^{N_{r,i'}} v_{s,i'j} r_{i'j} \quad (i' \neq i) \quad (77)$$

$$r_{ij} = A_{ij} Y_{s,i}^{n_{s,ij}} \exp\left(-\frac{E_{ij}}{RT_s}\right) X_{O_2}^{n_{O_2,ij}} \quad Y_{s,i} = \left(\frac{\rho_{s,i}}{\rho_s(0)}\right) \quad (78)$$

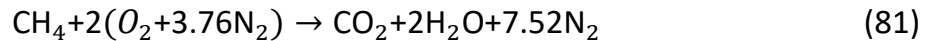
where r_{ij} is the rate of reaction at the temperature T_s for i^{th} material undergoing its j^{th} reaction, the second term on the right side of the equation denotes the contribution of the other materials producing the i^{th} materials as a residue with a yield of $v_{s,i'j}$. In this study, only the product of tar and gases were related to this term. $\rho_{s,i}$ is the density of i^{th} material component, and $\rho_s(0)$ represents the initial density. $n_{s,ij}$ is the reaction order, A_{ij} is the pre-exponential factor, s^{-1} and E_{ij} is the activation energy, kJ/mol.

2.3.4 Single-step reaction

The single-step reaction mechanism mainly contains two reactions: vaporization reaction and one pyrolysis reaction. The purpose of physical vaporization is to turn wet pine needles into dry pine needles which is an endothermic process. In order to simplify the model and achieve a single-step reaction, the pine needle was assumed to be made of cellulose and all the pyrolysis gases were derived from the following single reaction.



For the gas combustion reaction, previous studies noted that the pyrolysis gases produced by plant contain carbon dioxide, carbon monoxide, hydrogen and methane. Shotorban et al. [78] showed that most of the pyrolysis gases produced by cellulose, hemicellulose and lignin was methane. Accordingly, the simplified chemical reaction is adopted in this research, and the stoichiometric relation is presented as follow:



Thermal properties of solid fuel, moisture and char is given in Table 3. In order to simplify the model, the thermophysical properties of the initial pine needles and intermediate product are assumed to be identical. In Table 3., apparent density means bulk density.

Table 7. The thermophysical properties of solid fuel constituents [79, 80].

Species	Apparent density (kg/m ³)	Density (kg/m ³)	Thermal conductivity (W/mK)	Specific heat (kJ/kgK)
Moisture	-	1000	0.596	3.9
Dry fuel	650	2167	0.1256	2.3
Char	350	2333	0.0837	1.1

2.3.5 Multi-step reaction mechanism

In order to improve the numerical model, a multi-step reaction is implemented to model the pyrolysis process. The pine needles considered as moisture, cellulose, hemicellulose and lignin. The mass fraction of cellulose, hemicellulose and lignin in the dry fuel assumed to be 33%, 33% and 34%, respectively. The reaction scheme shown in figure 36 is utilized for each of the fuel components. The reaction scheme contains five reaction steps, and each solid material undergoes those reactions. Reactions R1-R3 are primary step and R4 is a secondary step. Similar to single-step reaction, the moisture reaction is also introduced in the mechanism.

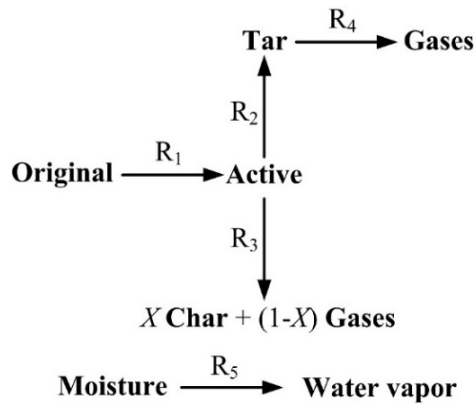


Figure 36. The reaction scheme of biomass [78, 81].

The thermophysical properties of each solid fuel (dry pine needles) and solid product (active and virgin cellulose, hemicellulose and lignin) of each step reaction are assumed identical, as shown in Table 3. The kinetic parameters of each reaction are given in Table 5.

Table 8. The kinetic parameters of each materials [79].

Reaction	A (s ⁻¹)	E (kJ/mol)
R1-cellulose	2.8×10^{19}	242.4
R2-cellulose	3.28×10^{14}	196.5
R3-cellulose	1.3×10^{10}	150.5
R1-hemicellulose	2.1×10^{16}	186.7
R2-hemicellulose	8.75×10^{15}	202.4
R3-hemicellulose	2.6×10^{11}	145.7
R1-lignin	9.6×10^8	107.6
R2-lignin	1.5×10^9	143.8
R3-lignin	7.7×10^6	111.4
R4	4.28×10^6	108
R5	5.13×10^{10}	88

2.4 Results and discussion

Figure 37(a) shows the contour of temperature for a vertical plane at center of wind tunnel for different time steps including 20 s, 85 s and 135 s. These results are for no wind condition and single-step reaction modeling. The maximum temperature exceeds 900 °C. According to the temperature variations, the flame height is around 50 cm. The vertical variation of velocity at the middle plane is shown in Figure 37(b). The results show that vertical component of velocity exceeds 3 m/s in some regions of flame.

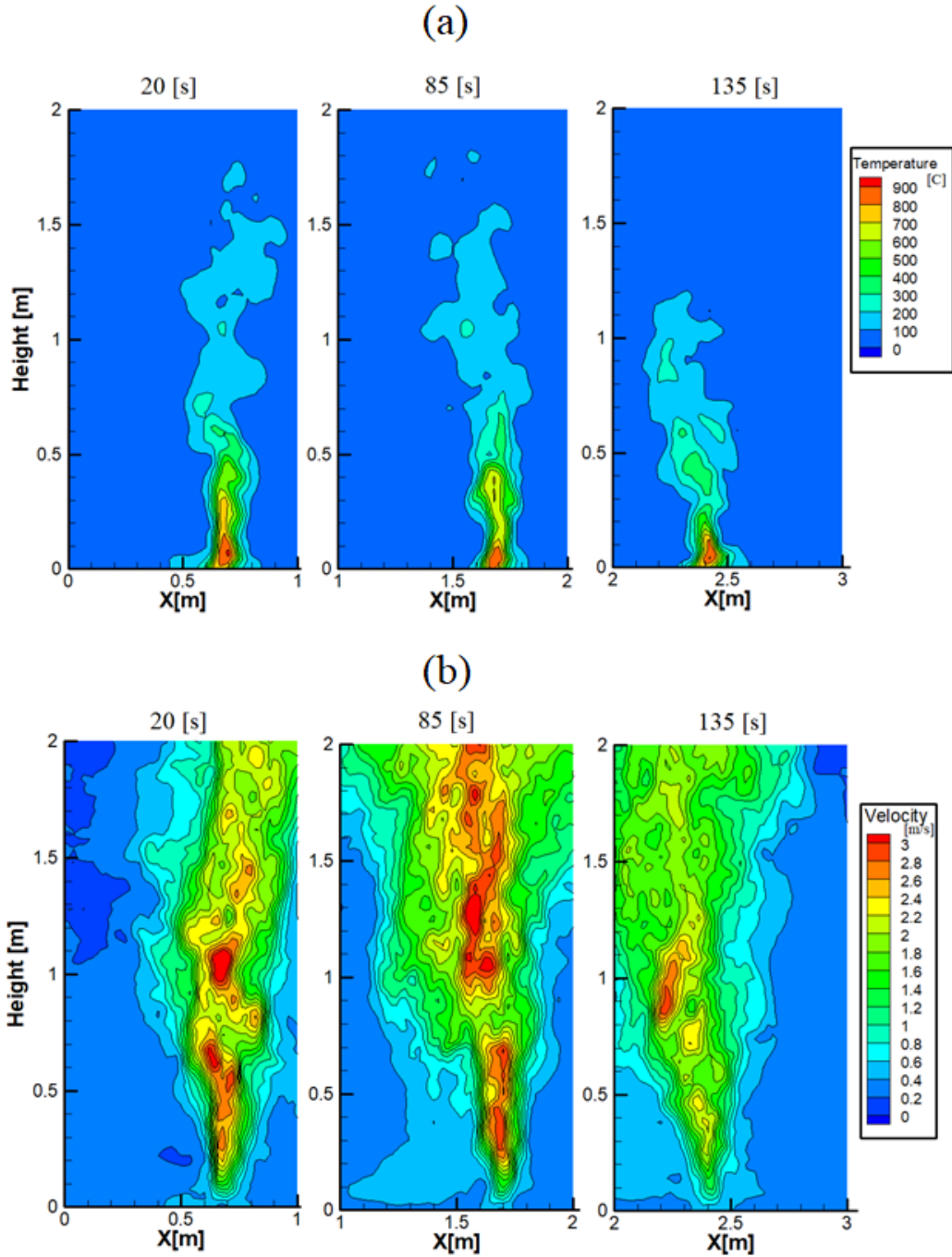


Figure 37. Contour of different flow quantities at a vertical plane at center of wind tunnel for different time steps 20, 85 and 135 s. a): Temperature b): Velocity

Figure 38 shows the variation of temperature versus normalized time for experiment, single-step reaction, and multi-step reaction modeling. The temperature was reported for a point at the fuel

bed surface at the center line. Three features can be extracted from the temperature graph: temperature rise trend, maximum temperature and peak temperature duration. The moments that the temperature rise and drop occur, denotes the flame front and backline, respectively. The temperature development trend for the single-step simulation was almost similar to the experiment for no wind condition and low wind condition, but the model overpredicted maximum temperature for high wind speed condition. The larger width of the peak for the single reaction compared to the experiment indicates that the flame width of the simulation is larger than the experiment.

In the case of single-step reaction modeling, the peak temperatures for no wind, 0.44 m/s and 1.0 m/s wind speeds are approximately 760 °C, 680 °C and 740 °C, respectively. Also, the relative temperature error between model prediction and experimental data were 17.6%, 16.6% and 45% for no wind, 0.44 m/s and 1.0 m/s wind speeds conditions, respectively. The multi-step reaction modeling improved the maximum temperature prediction compared to single-step reaction. The width of the peak curve is more similar to the experimental measurements. The peak temperature for no wind, 0.44 m/s and 1.0 m/s cases are 665 °C, 552 °C and 658 °C, respectively. The relative temperature error between model prediction and experimental data are 2.8%, 4.8% and 29%. Compared to the single-step model, the results of multi-step model indicated that the multi-step reaction model is more capable of predicting the temperature profile. However, the multi-step reaction model was incapable to predict the temperature profile for high wind speeds.

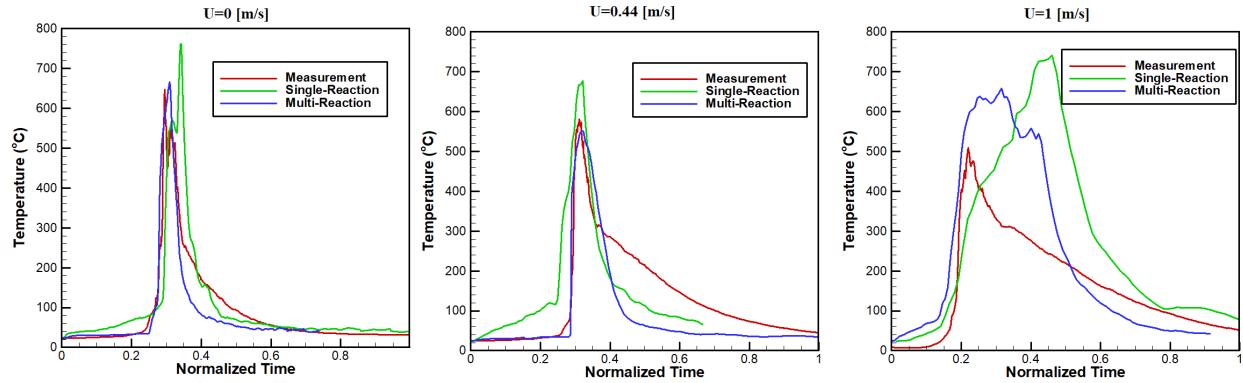


Figure 38. Temperature at the fuel bed surface for a point at the center of wind tunnel for experiment, single-step reaction and multi-step reaction modeling versus normalized time at different wind speeds

Figure 39 shows the contour of temperature at a vertical plane at middle of wind tunnel for different wind conditions and different modeling schemes. According to the contours, increase in incoming wind speed makes the flame larger and reduces the angle between flame and unburned fuel. Comparing the results of single-step reaction and multi-step reaction shows that the size of flame is bigger for single-step reaction modeling. From this result we can conclude that fire spread rate and maximum flame temperature is higher for single-step reaction modeling.

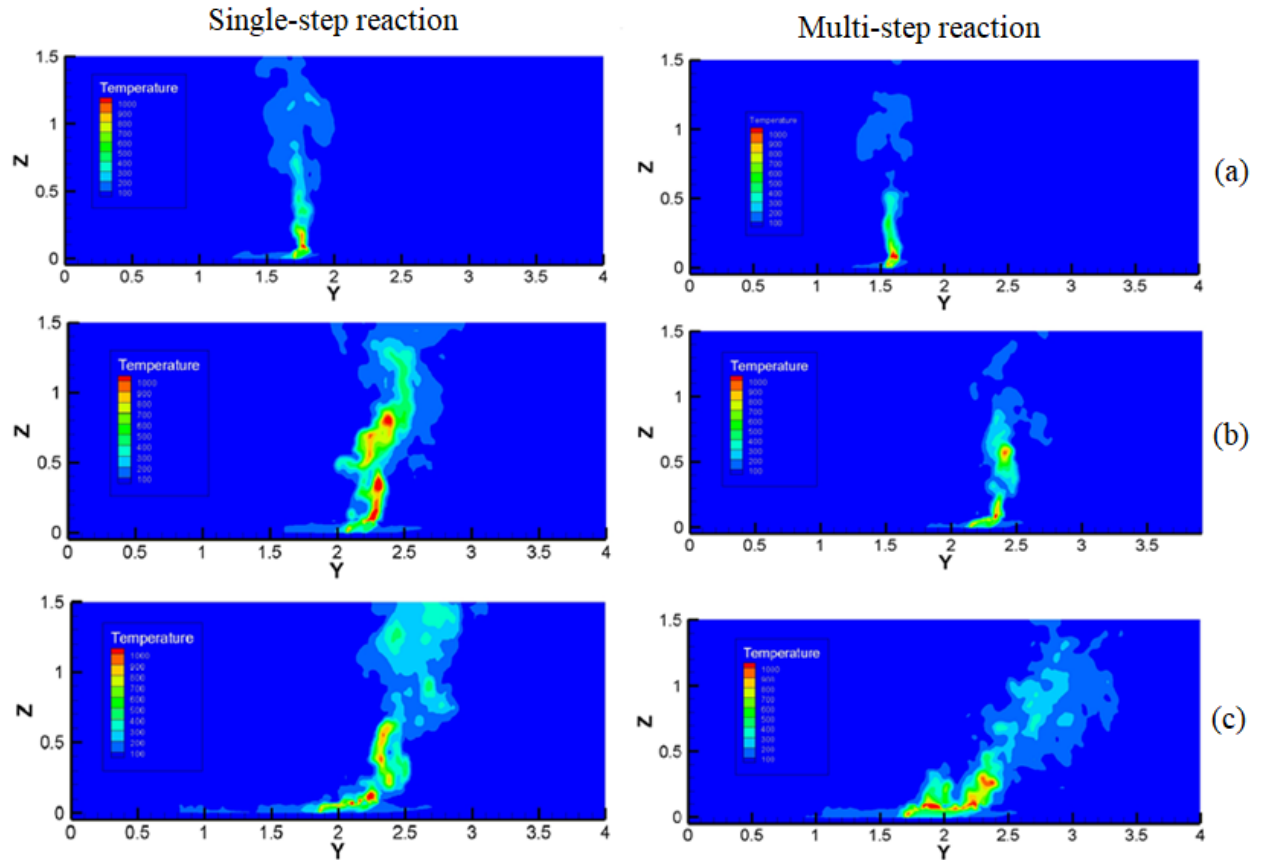


Figure 39. Contour of temperature at vertical plane at middle of wind tunnel for single-step reaction and multi-step reaction modeling. a): $U=0$ m/s. b): $U=0.44$ m/s. c): $U=1$ m/s.

The flame propagation shape is shown in figure 40 for experiment, single-step reaction and multi-step reaction at different wind speeds. According to the experiment, the flame shape and dimensions are greatly influenced by wind conditions. For no wind condition, the fire starts as a straight-line shape and changes to “U” shape. For 0.44 m/s wind condition, the fire represents a reverse “U” shape. For 1.0 m/s wind condition, the “U” shape fire still can be observed in a whole view. As figure 40 shows, both simulations were capable to replicate the fire shape for no wind and 0.44 m/s cases. But the flame curve is different between experiment and simulation at higher wind speeds.

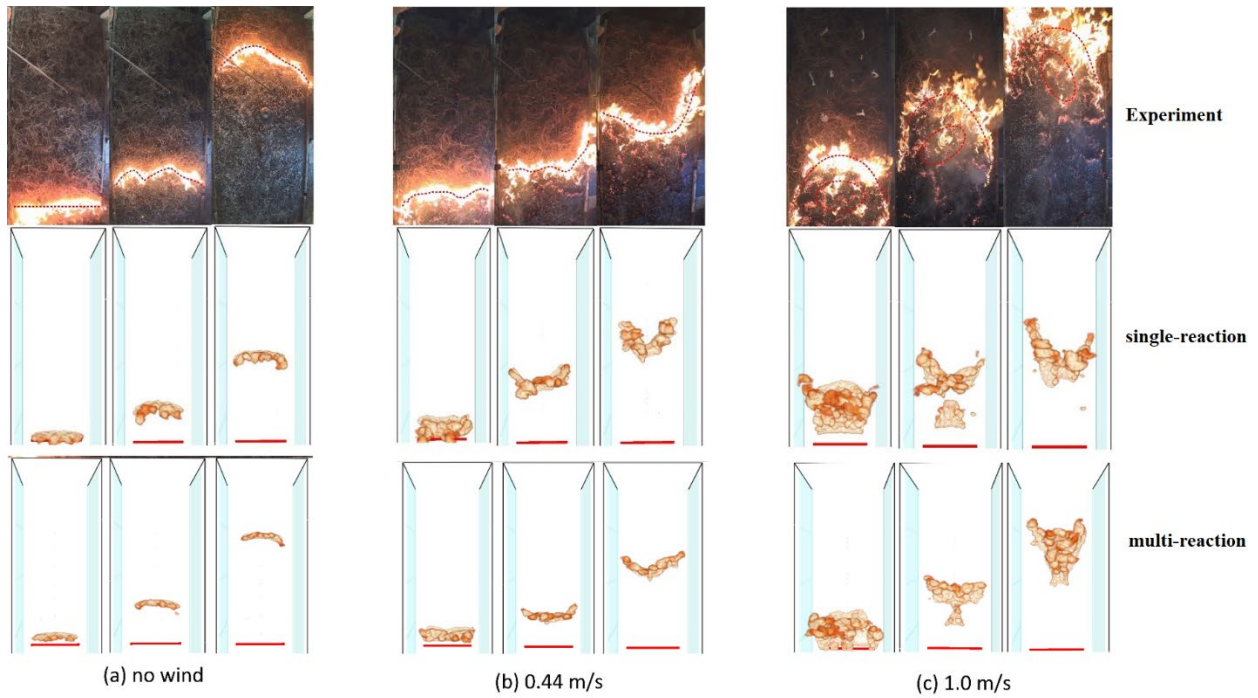


Figure 40. Flame dimensions from top view for experiment and simulation at different wind speed conditions.

Figure 41 compares the flame width between single-step reaction modeling and multi-step reaction modeling. The flame width for single-step reaction is larger compared to the multi-step reaction. For single-step reaction the flame width varies around 15 cm, while the flame width is around 10 cm for multi-step reaction.

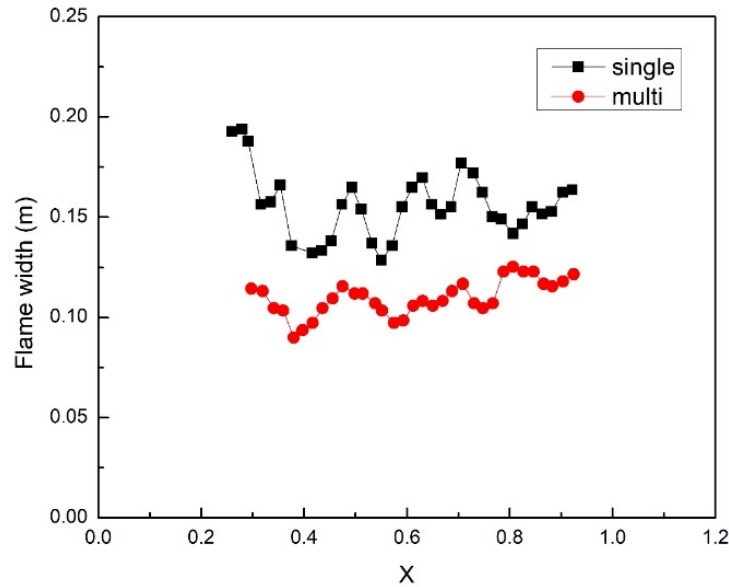


Figure 41. Flame width for single-step reaction and multi-step reaction at no wind condition.

Figure 42 shows the mass loss of pine needles at different wind speed conditions for both single-step and multi-step reactions. The pine needles had higher mass loss rate at higher wind speeds. Besides, the stable mass loss rate for the no wind condition, indicates that the combustion process was constant and even at no speed condition. But the mass loss rate has certain fluctuations that implies the flame changes dramatically at high wind speeds. In the case of multi-step reaction, the burning time is 550 s, 295 s and 130 s for 0 m/s, 0.44 m/s and 1.0 m/s, respectively. Figure 42 predicted higher residue for no wind conditions. It can be interpreted that combustion was incomplete for no wind conditions.

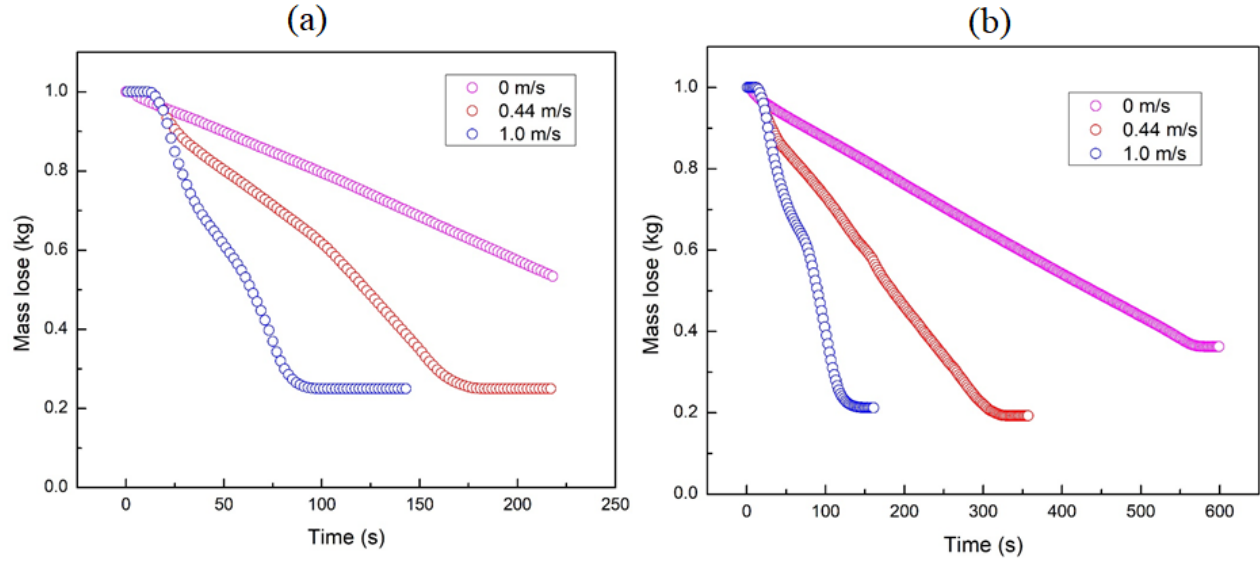


Figure 42. The mass loss with time for different wind speeds a): single-step reaction. b): multi-step reaction.

Table 4 shows the fire spread rate for experiment and different simulations. This fire spread rate was calculated based on the fuel mass loss rate and the flame front location. In the case of single-step reaction, since some endothermic reactions are neglected, the predicted fire spread rate is much faster compared to the experiment. The discrepancy between single-step reaction modeling and measurements is 48.9%, 60.7% and 68.7% for 0 m/s, 0.44 m/s and 1.0 m/s, respectively.

Table 9. Experimental and simulation data for fire spread rate.

Case no.	Wind velocity (m/s)	Experimental spread rate (cm/s)	Fire spread rate of single-step model (cm/s)	Fire spread rate of single-step model (cm/s)
1	0	0.58	0.86 (+48.9%)	0.51 (-12.1%)
2	0.44	1.037	1.67 (+60.7%)	0.95(-8.4%)
3	1.0	2.08	3.51(+68.7%)	2.13(2.4%)

In the case of multi-step reaction modeling, there were 12.1%, 8.4% and 2.4 % deviation between measurement and modeling for 0 m/s, 0.44 m/s and 1.0 m/s, respectively. This improvement in results indicates the capability of multi-step reaction model in fire spread prediction.

2.5 Conclusion

A series of Computational Fluid Dynamics simulations to study the fire spread across a pine needle fuel bed. Three different wind conditions including $U=0$, 0.44, and 1 m/s were investigated. Two modeling schemes, single-step reaction and multi-step reaction were utilized to model the pyrolysis process. In the single-step reaction, the pine needles were considered as cellulose, while for the multi-step reaction the pine needles were modeled as a combination of cellulose, hemicellulose and lignin. To validate the numerical methodology, the numerical temperature and flame spread rate data were compared with wind tunnel measurements. Different quantities such as temperature at fuel bed surface, flame shape, flame spread rate, flame width and fuel mass loss were analyzed in this study. Single-step reaction model overpredicted the flame spread rate, while the multi-step reaction model could predict flame spread rate. The flame was predicted 50% wider in the single-step reaction model compared to the multi-step reaction.

References

- [1] Fons, W.L.: Analysis of fire spread in light fuels. *J. Agric. Res.* 93–121 (1946)
- [2] Butler, B.W., Cohen, J., Latham, D.J., Schuette, R.D., Sopko, P., Shannon, K.S., Jimenez, D., Bradshaw, L.S.: Measurements of radiant emissive power and temperatures in crown fires. *Can. J. For. Res.* 34, 1577–1587 (2004). doi:10.1139/x04-060
- [3] Silvani, X., Morandini, F., Dupuy, J.-L.: Effects of slope on fire spread observed through video images and multiple-point thermal measurements. *Exp. Therm. Fluid Sci.* 41, 99–111 (2012). doi:10.1016/J.EXPTHERMFLUSCI.2012.03.021
- [4] Anderson, W.R., Catchpole, E.A., Butler, B.W.: Convective heat transfer in fire spread through fine fuel beds. *Int. J. Wildl. Fire.* 19, 284 (2010). doi:10.1071/WF09021
- [5] Albini, F.A.: Wildland Fire Spread by Radiation-a Model Including Fuel Cooling by Natural Convection. *Combust. Sci. Technol.* 45, 101–113 (1986). doi:10.1080/00102208608923844
- [6] Finney, M.A., Cohen, J.D., Forthofer, J.M., Mcallister, S.S., Gollner, M.J., Gorham, D.J., Saito, K., Akafuah, N.K., Adam, B.A., English, J.D., Dickinson, R.E.: Role of buoyant flame dynamics in wildfire spread. *Proc. Natl. Acad. Sci.* 112, 9833–9838 (2015). doi:10.1073/pnas.1504498112
- [7] Frankman, D., Webb, B.W., Butler, B.W., Jimenez, D., Forthofer, J.M., Sopko, P., Shannon, K.S., Hiers, J.K., Ottmar, R.D.: Measurements of convective and radiative heating in wildland fires. *Int. J. Wildl. Fire.* 22, 157–167 (2013). doi:10.1071/WF11097
- [8] Cohen, J.D.: Fuel Particle Heat Exchange during Wildland Fire Spread, (2015)
- [9] Frankman, D., Webb, B.W., Butler, B.W.: Time-Resolved Radiation and Convection Heat Transfer in Combusting Discontinuous Fuel Beds. *Combust. Sci. Technol.* 182, 1391–1412

- (2010). doi:10.1080/00102202.2010.486388
- [10] Morandini, F., Silvani, X.: Experimental investigation of the physical mechanisms governing the spread of wildfires. *Int. J. Wildl. Fire.* 19, 570 (2010). doi:10.1071/WF08113
 - [11] Weise, D.R., Biging, G.S.: Effects of wind velocity and slope on fire behavior. *Tak. Kashiwagi, ed. 1994. Fire Saf. Sci. Proc. Fourth Int. Symp. Intl. Assoc. Fire Saf. Sci. Boston, MA pp 1041-1051. 4, 1041–1051 (1994).* doi:10.3801/IAFSS.FSS.4-104
 - [12] Weise, D.R., Zhou, X., Sun, L., Mahalingam, S.: Fire spread in chaparral—'go or no-go?'. *Int. J. Wildl. Fire.* 14, 99 (2005). doi:10.1071/WF04049
 - [13] Morandini, F., Silvani, X., Susset, A.: Feasibility of particle image velocimetry in vegetative fire spread experiments. *Exp. Fluids.* 53, 237–244 (2012). doi:10.1007/s00348-012-1285-5
 - [14] Mungal, M.G., Lourenco, L.M., A., K.: Instantaneous Velocity Measurements in Laminar and Turbulent Premixed Flames Using On-Line PIV. *Combust. Sci. Technol.* 106, 239–265 (1995). doi:10.1080/00102209508907781
 - [15] Gustenyov, N., Akafuah, N.K., Salaimeh, A., Finney, M., McAllister, S., Saito, K.: Scaling nonreactive cross flow over a heated plate to simulate forest fires. *Combust. Flame.* 197, 340–354 (2018). doi:10.1016/J.COMBUSTFLAME.2018.08.014
 - [16] Clark, T.L., Radke, L., Coen, J., Middleton, D., Clark, T.L., Radke, L., Coen, J., Middleton, D.: Analysis of Small-Scale Convective Dynamics in a Crown Fire Using Infrared Video Camera Imagery. *J. Appl. Meteorol.* 38, 1401–1420 (1999). doi:10.1175/1520-0450(1999)038<1401:AOSSCD>2.0.CO;2
 - [17] Zhou, X., Sun, L., Mahalingam, S., Weise, D.R.: Thermal particle image velocity estimation of fire plume flow. *Combust. Sci. Technol.* 175, 1293–1316 (2003). doi:10.1080/00102200302376

- [18] Ho, C.M., Jakus, K., Parker, K.H.: Temperature fluctuations in a turbulent flame. *Combust. Flame*. 27, 113–123 (1976). doi:10.1016/0010-2180(76)90011-0
- [19] Wu, Y., Xing, H., Atkinson, G.: Interaction of fire plume with inclined surface. *Fire Saf. J.* 35, 391–403 (2000). doi:10.1016/S0379-7112(00)00032-1
- [20] Toepler, A.: Beobachtungen nach einer neuen optischen Methode, Cohen, Bonn. (1864)
- [21] Wernekinck, U., Merzkirch, W.: Speckle photography of spatially extended refractive-index fields. *Appl. Opt.* 26, 31 (1987). doi:10.1364/AO.26.000031
- [22] Dalziel, S.B., Hughes, G.O., Sutherland, B.R.: Whole-field density measurements by “synthetic schlieren.” *Exp. Fluids*. 28, 322–335 (2000). doi:10.1007/s003480050391
- [23] Meier G E A: Hintergrund Schlierenmessverfahren, (1999)
- [24] Settles, G.S., Hargather, M.: A review of recent developments in schlieren and shadowgraph techniques *This. Meas. Sci. Technol.* (2017). doi:10.1088/1361-6501/aa5748
- [25] Meier, G.: Computerized background-oriented schlieren. *Exp. Fluids*. 33, 181–187 (2002). doi:10.1007/s00348-002-0450-7
- [26] Wetzstein, G., Raskar, R., Heidrich, W.: Hand-held Schlieren Photography with Light Field probes. In: 2011 IEEE International Conference on Computational Photography (ICCP). pp. 1–8. IEEE (2011)
- [27] Leopold, F.: The Application of the Colored Background Oriented Schlieren Technique (CBOS) to Free-Flight and In-Flight Measurements. In: 2007 22nd International Congress on Instrumentation in Aerospace Simulation Facilities. pp. 1–10. IEEE (2007)
- [28] Ota, M., Hamada, K., Kato, H., Maeno, K.: Computed-tomographic density measurement of supersonic flow field by colored-grid background oriented schlieren (CGBOS) technique. *Meas. Sci. Technol.* 22, 104011 (2011). doi:10.1088/0957-0233/22/10/104011

- [29] Bauknecht, A., Merz, C.B., Raffel, M., Landolt, A., Meier, A.H.: Blade-Tip Vortex Detection in Maneuvering Flight Using the Background-Oriented Schlieren Technique. *J. Aircr.* 51, 2005–2014 (2014). doi:10.2514/1.C032672
- [30] Aminfar, A., Davoodzadeh, N., Aguilar, G., Princevac, M.: Application of optical flow algorithms to laser speckle imaging. *Microvasc. Res.* (2018). doi:10.1016/J.MVR.2018.11.001
- [31] Heineck, J.T., Banks, D., Schairer, E.T., Haering, E.A., Bean, P.: Background Oriented Schlieren (BOS) of a Supersonic Aircraft in Flight. In: *AIAA Flight Testing Conference*. American Institute of Aeronautics and Astronautics, Reston, Virginia (2016)
- [32] Schwar, M.J.R., Weinberg, F.J.: Laser techniques in combustion research. *Combust. Flame.* 13, 335–374 (1969). doi:10.1016/0010-2180(69)90106-0
- [33] Förster, F.J., Dröske, N.C., Bühler, M.N., von Wolfersdorf, J., Weigand, B.: Analysis of flame characteristics in a scramjet combustor with staged fuel injection using common path focusing schlieren and flame visualization. *Combust. Flame.* 168, 204–215 (2016). doi:10.1016/J.COMBUSTFLAME.2016.03.010
- [34] Albers, B.W., Agrawal, A.K.: Schlieren analysis of an oscillating gas-jet diffusion flame. *Combust. Flame.* 119, 84–94 (1999). doi:10.1016/S0010-2180(99)00034-6
- [35] Mattsson, R., Kupiainen, M., Gren, P., Wåhlin, A., Carlsson, T.E., Fureby, C.: Pulsed TV holography and schlieren studies, and large eddy simulations of a turbulent jet diffusion flame. *Combust. Flame.* 139, 1–15 (2004). doi:10.1016/J.COMBUSTFLAME.2004.06.005
- [36] Brequigny, P., Endouard, C., Mounaïm-Rousselle, C., Foucher, F.: An experimental study on turbulent premixed expanding flames using simultaneously Schlieren and tomography techniques. *Exp. Therm. Fluid Sci.* 95, 11–17 (2018).

doi:10.1016/J.EXPTHERMFLUSCI.2017.12.018

- [37] Choi, J.-H., Lee, W.-J., Park, S.-K., Kim, J., Choi, B.C.: Experimental study on the flame propagation behaviors of R245fa(C₃H₃F₅)/CH₄/O₂/N₂ mixtures in a constant volume combustion chamber. *Exp. Therm. Fluid Sci.* 101, 276–282 (2019). doi:10.1016/J.EXPTHERMFLUSCI.2018.10.030
- [38] Harker, M.R., Hattrell, T., Lawes, M., Sheppard, C.G.W., Tripathi, N., Woolley, R.: Measurements of the Three-Dimensional Structure of Flames at Low Turbulence. *Combust. Sci. Technol.* 184, 1818–1837 (2012). doi:10.1080/00102202.2012.691775
- [39] Grauer, S.J., Unterberger, A., Rittler, A., Daun, K.J., Kempf, A.M., Mohri, K.: Instantaneous 3D flame imaging by background-oriented schlieren tomography. *Combust. Flame.* 196, 284–299 (2018). doi:10.1016/j.combustflame.2018.06.022
- [40] Weise, D.R., et. al., T.H., Johnson, T.J., Hao, W., Dietenberger, M., Princevac, M., Butler, B., McAllister, S., O'Brien, J., Loudermilk, L., Ottmar, R., Hudak, A., Kato, A., Shotorban, B., Mahalingam, S., Mell, W.E.: A project to measure and model pyrolysis to improve prediction of prescribed fire behavior. In: *Advances in forest fire research 2018*. pp. 308–318. Imprensa da Universidade de Coimbra (2018)
- [41] Lozano, J.: *An investigation of surface and crown fire dynamics in shrub fuels*, (2011)
- [42] Cobian-Iñiguez, J., Aminfar, A., Chong, J., Burke, G., Zuniga, A., Weise, D.R., Princevac, M.: Wind Tunnel Experiments to Study Chaparral Crown Fires. *J. Vis. Exp.* e56591–e56591 (2017). doi:10.3791/56591
- [43] Maynard, T., Princevac, M., Weise, D.R.: A Study of the Flow Field Surrounding Interacting Line Fires. *J. Combust.* 2016, 1–12 (2016). doi:10.1155/2016/6927482
- [44] Maynard, T., Princevac, M.: The Application of a Simple Free Convection Model to the

- Pool Fire Pulsation Problem. *Combust. Sci. Technol.* 184, 505–516 (2012).
doi:10.1080/00102202.2011.648034
- [45] Lozano, J., Tachajapong, W., Weise, D.R., Mahalingam, S., Princevac, M.: Fluid Dynamic Structures in a Fire Environment Observed in Laboratory-Scale Experiments. *Combust. Sci. Technol.* 182, 858–878 (2010). doi:10.1080/00102200903401241
- [46] Gladstone, J.H., Dale, T.P.: Researches on the Refraction, Dispersion, and Sensitiveness of Liquids. *Philos. Trans. R. Soc. London*, Vol. 153, pp. 317–343. 153, 317–343 (1863)
- [47] Settles, G.S.: Basic Concepts. In: *Schlieren and Shadowgraph Techniques*. pp. 25–38. Springer Berlin Heidelberg, Berlin, Heidelberg (2001)
- [48] Wey, F.J.: Analysis of optical methods. In: *Physical Measurements in Gas and Dynamics and Combustion*. pp. 3–25 (1954)
- [49] de Ris, J.L.: Mechanism of Buoyant Turbulent Diffusion Flames. *Procedia Eng.* 62, 13–27 (2013). doi:10.1016/J.PROENG.2013.08.040
- [50] Taylor, Z.J., Gurka, R., Kopp, G.A., Liberzon, A.: Long-Duration Time-Resolved PIV to Study Unsteady Aerodynamics. *IEEE Trans. Instrum. Meas.* 59, 3262–3269 (2010). doi:10.1109/TIM.2010.2047149
- [51] Venkatakrishnan, L., Meier, G.E.A.: Density measurements using the Background Oriented Schlieren technique. *Exp. Fluids.* 37, (2004). doi:10.1007/s00348-004-0807-1
- [52] Atcheson, B., Heidrich, W., Ihrke, I.: An evaluation of optical flow algorithms for background oriented schlieren imaging. *Exp. Fluids.* 46, 467–476 (2009). doi:10.1007/s00348-008-0572-7
- [53] Horn, B.K.P., Schunck, B.G.: Determining Optical Flow. *Artif. Intell.* 17, 185–203 (1980)
- [54] Lucas, B.D., Kanade, T.: An Iterative Image Registration Technique with an Application to

Stereo Vision. 674–679 (1981)

- [55] Farnebäck, G.: Two-Frame Motion Estimation Based on Polynomial Expansion. In: Image analysis. pp. 363–370 (2003)
- [56] Brox, T., Bruhn, A., Papenberg, N., Weickert, J.: High Accuracy Optical Flow Estimation Based on a Theory for Warping. Springer (2004)
- [57] Zach, C., Pock, T., Bischof, H.: A Duality Based Approach for Realtime TV-L 1 Optical Flow. In: Pattern Recognition. pp. 214–223. Springer Berlin Heidelberg, Berlin, Heidelberg (2007)
- [58] Gibson, J.J.: The senses considered as perceptual systems. Houghton Mifflin, Oxford, England (1966)
- [59] Uras, S., Giroso, F., Verri, A., Torre, V.: A computational approach to motion perception. Biol. Cybern. 60, 79–87 (1988). doi:10.1007/BF00202895
- [60] Sánchez Pérez, J., Meinhardt-Llopis, E., Facciolo, G.: TV-L1 Optical Flow Estimation. Image Process. Line. 3, 137–150 (2013). doi:10.5201/ipol.2013.26
- [61] Bühlmann, P., Meier, A.H., Ehrensperger, M., Rösger, T.: Laser speckle based background oriented schlieren measurements in a fire backlayering front. In: 17th international symposium on applications of laser techniques to fluid mechanic. , Lisbon (2014)
- [62] Xue, T., Rubinstein, M., Wadhwa, N., Levin, A., Durand, F., Freeman, W.T.: Refraction Wiggles for Measuring Fluid Depth and Velocity from Video. Proc. Eur. Conf. Comput. Vis. (ECCV. (2014)
- [63] Raffel, M.: Background-oriented schlieren (BOS) techniques. Exp Fluids. 56, (2015). doi:10.1007/s00348-015-1927-5
- [64] Anandan, P.: A Computational Framework and an Algorithm for the Measurement of Visual

- Motion. (1989)
- [65] Hargather, M.J., Settles, G.S.: Background-oriented schlieren visualization of heating and ventilation flows: HVAC-BOS. HVAC R Res. 17, 771–780 (2011). doi:10.1080/10789669.2011.588985
- [66] Nelson, R.M.: Byram's Derivation of the Energy Criterion for Forest and Wildland Fires. (1993)
- [67] Weise, D.R., Fletcher, T.H., Cole, W., Mahalingam, S., Zhou, X., Sun, L., Li, J.: Fire behavior in chaparral—Evaluating flame models with laboratory data. Combust. Flame. 191, 500–512 (2018). doi:10.1016/J.COMBUSTFLAME.2018.02.012
- [68] Cheung, S.C.P., Yeoh, G.H.: A fully-coupled simulation of vortical structures in a large-scale buoyant pool fire. Int. J. Therm. Sci. 48, 2187–2202 (2009). doi:10.1016/j.ijthermalsci.2009.04.011
- [69] Clark¹, T.L., Jenkins², M.A., Coen¹, J.L., Packham³, D.R.: A Coupled Atmosphere-Fire Model: Role of the Convective Froude Number and Dynamic Fingering at the Fireline. (1996)
- [70] Porterie, B., Nicolas, S., Consalvi, J.L., Loraud, J.C., Giroud, F., Picard, C.: MODELING THERMAL IMPACT OF WILDLAND FIRES ON STRUCTURES IN THE URBAN INTERFACE. PART 1: RADIATIVE AND CONVECTIVE COMPONENTS OF FLAMES REPRESENTATIVE OF VEGETATION FIRES. Numer. Heat Transf. Part A Appl. 47, 471–489 (2005). doi:10.1080/10407780590891434
- [71] National Interagency Fire Center: https://www.nifc.gov/fireInfo/fireInfo_statistics.html
- [72] Pyne, S.J.: Introduction to Wildland Fire: Fire Management in the United States. John Wiley & Sons Inc (1984)

- [73] Sullivan, A.: Wildland surface fire spread modelling, 1990–2007. 1: Physical and quasi-physical models. *Int. J. Wildl. Fire.* 18, 349–368 (2009)
- [74] Yashwanth, B.L., Shotorban, B., Mahalingam, S., Lautenberger, C.W., Weise, D.R.: A numerical investigation of the influence of radiation and moisture content on pyrolysis and ignition of a leaf-like fuel element. *Combust. Flame.* 163, 301–316 (2016). doi:10.1016/j.combustflame.2015.10.006
- [75] McGrattan, K., Hostikka, S., McDermott, R., Floyd, J., Vanella, M.: *Fire Dynamics Simulator Technical Reference Guide Volume 1: Mathematical Model.* 1., doi:http://dx.doi.org/10.6028/NIST.SP.1018
- [76] Deardorff, J.W.: Stratocumulus-capped mixed layers derived from a three-dimensional model. *Boundary-Layer Meteorol.* 18, 495–527 (1980)
- [77] Pope, S.B.: *Turbulent Flows.* (2000)
- [78] Shotorban, B., Yashwanth, B.L., Mahalingam, S., Haring, D.J.: An investigation of pyrolysis and ignition of moist leaf-like fuel subject to convective heating. *Combust. Flame.* 190, 25–35 (2018). doi:10.1016/j.combustflame.2017.11.008
- [79] MILLER, R.S., BELLAN, J.: A Generalized Biomass Pyrolysis Model Based on Superimposed Cellulose , Hemicellulose and Lignin Kinetics. *Combust. Sci. Technol.* 126, 97–137 (1997). doi:10.1080/00102209708935670
- [80] Bryden, K.M., Hagge, M.J.: Modeling the combined impact of moisture and char shrinkage on the pyrolysis of a biomass particle. *q.* 82, 1633–1644 (2003). doi:10.1016/S0016-2361(03)00108-X
- [81] Mell, W., Maranghides, A., McDermott, R., Manzello, S.L.: Numerical simulation and experiments of burning douglas fir trees. *Combust. Flame.* 156, 2023–2041 (2009).

doi:10.1016/j.combustflame.2009.06.015